Shear Banding in Metallic Glass

A mathematical perspective inspired by soil mechanics

Jacob Corteen

A thesis presented for the degree of Doctor of

Philosophy, January 2014

Department of Materials Science and Engineering

Faculty of Engineering

University of Sheffield

Sheffield

Contents

List of Figures

5

8

List of Tables

List of Symbols

Symbol	Definition
a_m	length of a axis of monoclinic CuZr B19' unit cell
A	potential energy equation for the force chain system in terms of u_m only
b_m	length of b axis of monoclinic CuZr B19' unit cell
B	Bulk Modulus
c_m	length of c axis of monoclinic CuZr B19' unit cell
C_{ij}	terms of the compliance tensor
d_i	sliding distance of the ith particle against k_t
dS	surface element for integral around transformation zone
D	compound parameter defined in Equation 4.27, carries information about buckling mode
E	Young's Modulus
$\dot{E}$	ratio of energy rates in the 1 and 2 directions
E_m	Young's modulus of matrix
E_p	Young's modulus of transforming particle
F	the force applied axially along the force chain
G	Shear Modulus
G_{inf}	Shear Modulus at infinite frequency
G_0	chemical free energy of transformation per unit volume
F_{min}	force required to buckle a force chain in any given buckling mode
F_{crit}	force required to buckle the force chain in the buckling mode with lowest F_{min}
h_I	weight function in Mode I

h_{II}	weight function in Mode II
k_n	spring constant opposing axial compression of the force chain
k_r	spring constant opposing rotation of particles
k_s	spring constant governing lateral support on the force chain
k_t	spring constant opposing sliding of particles across one another
K	buckling segment size in particles (peak to peak), given by $(N+1)/(m_crit)+1$
K_I	crack or shear band tip stress intensity factor in Mode I
K_{II}	crack or shear band tip stress intensity factor in Mode II
m	wavenumber defining a particular buckling mode
m_{crit}	wavenumber corresponding to the buckling mode with lowest associated F_{min}
m_f	fragility, given by $\frac{dlog_{10}\tau}{d(T_g/T)}\Big|_{Tg}$
M	number of parallel force chains in an assembly. There are $(M-1)\tan(\beta)+K$ particles in a chain.
n	normal vector to transformation zone surface
N	there are N+2 particles in a force chain
p_i	temporary parameter used in Figure 4.5, special case of Δ_i
q_i	lateral displacement of the ith particle is given by $q_i R$
r	distance from crack or shear band tip. Forms a coordinate system with θ
r'	$\frac{\partial r}{\partial \theta}$
r_c	transformation zone radius
R	force chain particle radius
s_x	12-term of the transformation strain matrix
s_y	21-term of the transformation strain matrix
T	body forces in matrix to cancel out particle surface tractions $\mathbf{T_c}$
$\mathbf{T_c}$	tractions applied to transformed particle surface to fit it back into its original space
w	transformation zone height
W	potential energy equation for the force chain system broken down into Fourier terms
u_m	modal amplitude for displacement terms for the buckling mode with wavenumber m
v_x	11-term of the transformation strain matrix

v_y	22-term of the transformation strain matrix
V	potential energy equation for the force chain system
V_f	volume fraction of particles in the transformation zone
V_p	volume of the transforming particle
x	lateral displacement of particles at either end of a buckling segment
α	angle defined by the plane of easiest failure
β	shear band angle (also: angle between x-direction and line linking end buckling segments)
β_1	ratio of matrix and particle elastic moduli E_m/E_p
β_m	angle between a and c axes in CuZr B19' martensite
Δ_a	distance over which the crack or shear band tip has advanced
Δ_b	axial compression due to buckling
Δ_{crit}	axial shortening at the onset of buckling
ΔG	total free energy change of transformation
Δ_i	axial compression between the ith and $i+1$th particles
Δ_K	change in crack or shear band tip stress intensity due to transformation
ΔU	total strain energy change of transformation
ΔU_D	deviatoric component of strain energy change of transformation
ΔU_H	hydrostatic component of strain energy change of transformation
ΔU_T	strain energy change of transformation when not under applied stress
ΔU_I^T	strain energy change of transformation - term accounting for bias by applied stress
ϵ_1	strain in y direction, ie along chain axis
ϵ_1^{crit}	axial strain required to initiate buckling, given by $F_{min}/2Rk_n$
ϵ_2	strain in x direction, ie perpendicular to chain axis
ϵ^c	volume component of the transformation strain of the constrained particle
$`\epsilon_{ij}^c$	shape component of the transformation strain of the constrained particle
ϵ_{ij}^T	transformation strain of the unconstrained particle
ϵ^T	volume term of transformation strain of the unconstrained particle, see also $\epsilon^{\mathbf{T}}$
$`\epsilon_{ij}^T$	shape term of transformation strain of the unconstrained particle, see also ϵ^S

ϵ^S	shape term of transformation strain of the unconstrained particle, see also ϵ_{ij}^T
ϵ^{T*}	transformation strain of the 'equivalent particle'
$\boldsymbol{\epsilon^T}$	transformation strain of the unconstrained particle, see also ϵ_{ij}^T
ϵ_{eff}^T	$e^T V_f$ effective transformation strain after volume fraction accounted for
θ	angle away from centreline of shear band or crack. Forms a coordinate system with r
μ	parameter relating to internal friction
ν	Poisson's ratio
σ_1	stress applied in the y-direction, along the chain axes
σ_2	stress applied in the x-direction, usually by lateral support or constraint
σ_{ij}^A	strain applied to the transforming particle
σ^I	volume component of σ_{ij}^I
$'\sigma_{ij}^I$	shape change component of σ_{ij}^I
σ_{ij}^I	stresses that develop in the transformed particle under Eshelby surface tractions
σ_n	normal stress on the yield plane
τ_0	τ_y for no applied normal stress
τ_r	relaxation time
τ_y	shear stress at yield
ϕ_m	modal amplitude for rotation terms for the buckling mode with wavenumber m
ϕ_μ	true angle of friction
ϕ_f	nominal friction angle
ψ_i	angle rotated to bring the former centrelines of the ith and $i+1$th particles parallel
ω_i	clockwise rotation from the vertical of the ith particle
$\sin(\psi^*)$	dilatancy parameter

Abstract

There have been many approaches to engineering toughness in metallic glasses. Some have worked in composites, such as the transformation-toughened examples developed recently. Others have delved into the fundamental nature of deformation in these systems. Here, a number of mathematical models from other fields are applied in order to shed light on some of these advances.

A model of transformation toughening more typically used in ceramics is adapted to consider the question of whether martensitic transformation in CuZr austenitic nanocrystals can in fact toughen the surrounding glass by the same mechanism as is typically invoked for crystalline materials. The results draw that explanation into question - the volume change associated with transformation in that system is just too small to significantly modify the shear band tip stress state, and the shape strain terms are constrained by variant self-accommodation and matters of orientation.

A model developed to describe dilatant shear banding in granular media is then adapted to draw new insight on the same problem in metallic glasses. By modelling the glassy system as made up of clusters that behave like particles in sand or gravel, arranged into load-bearing force chains that fail by buckling, the behaviour of the system is shown to depend on a series of spring constants that represent the local packing and bonding in the glass. These spring constants emerge as a new order parameter, promising the possibility of a direct quantitative link between the state of structural order and the degree of dilatation associated with deformation. The new order parameters represent a first step to bridging the gap between nanoscale bonding and structure, and larger-scale properties.

Acknowledgements

When considering the long list of people who deserve acknowledgement here, perhaps the best approach is to provide the story of how I got this far. In materials science at least, the tale begins with Stephen Martin, the physics teacher who first got me interested in materials specifically. I was always going to study Natural Sciences once I got my undergraduate offer, but thanks are due to James Elliott for the interesting conversation that probably got me through the interview, and subsequent support.

When things went a bit wrong later on, it was perhaps an excellent and much appreciated reference from Bill Clyne that helped get Sheffield to take a chance on me at Masters level, a chance I took with both hands. Dave Randman has to get a lot of credit for helping me through the research project that followed. Some poking from Mark Rainforth and Brad Wynne later, and I was talking to Iain Todd about a PhD project. Iain, with his skill for managing my occasional panic attacks and encylopoediac knowledge of the academic literature, has gotten me this far by dangling interesting science in front of my nose and giving me the space I needed to work on it. Many thanks there. The whole research group were very good to me - John Plummer in particular deserves a mention for a lot of help and advice, and Andy Cunliffe for grounding me in reality ever so often. The EPSRC of course must be thanked for providing the funding to carry out the research.

I couldn't write this without mentioning my family, who have been there for me however hard things have gotten for any of us. The cliche of "I couldn't have done it without you" is entirely true here. And then we come to Victoria, whom I love unreservedly and absolutely, and whose encouragement, patience and faith have kept me going to the end. Victoria, I love you, from the bottom of my heart.

Chapter 1

Introduction

More than 50 years after their initial discovery, metallic glasses remain a material of considerable scientific interest. Unlike their crystalline counterparts, the nature of their deformation behaviour remains to be fully understood and presents a significant outstanding challenge to the materials community.

The object of this work was initially to investigate metallic glass matrix composites undergoing transformation toughening as typified by the work of Eckert et al [1] at IFW Dresden. Given the extremely attractive ductility and work hardening behaviour observed in these systems, they can be considered one of the most promising recent advances in metallic glass research.

An initial investigation into the toughening effect soon raised the issue that the effects of transforming particles on the stress state near the shear band tip were often being cited as a possible explanation for the toughening behaviour. In fact, the volume strain associated with transformation in the martensites in question is very low, calling into question this explanation as the transformation should have little effect.

It is often the case that scientists working in one field will possess techniques of significant applicability to problems in another, should the connection only be noticed. In this case the search for an approach to quantify this behaviour did not need to go far - the fracture mechanics of transformation toughening in ceramics is a well established discipline. As such, approaches more typically used in zirconia were adapted to apply to metallic glasses. The goal was to identify if such

small transformation strains could indeed result in the observed toughening and work-hardening behaviours. Considering both volume and shape strains, it became clear as the analysis was completed that such small strains would indeed have little impact on the stress state at the shear band tip.

This presented somewhat of a null result - one of the established explanations for the toughening effect had been called into question, but no strong alternatives had come to light (beyond the established approach focussing simply on hardening due to transformation to martensite impacting the rule-of-mixtures properties and shear banding behaviour of the combined system). No fresh direction of research immediately presented itself.

It was at this point that a paper came to light concerning a phenomenon known as cataclystic deformation in geology. While not directly applicable to the problem of transformation toughening, significant parallels were noticed between the geological phenomena and shear banding in metallic glasses. As such the idea was born to divert research into the fundamental nature of shear banding from a mathematical perspective, using models developed for use in geology and in particular soil mechanics. The research could be tied together by the use of cross-disciplinary mathematical models developed for other materials and other length scales, and would represent a mathematical picture of shear banding as a wider phenomenon.

The existence of shear banding on various length scales has already had attention called to it by Gourlay [2], who compared behaviour in soils and sands to the smaller length scale of semi-solid slurries during metal solidification. Given that, it did not seem a significant stretch to imagine that shear banding at smaller length scales yet might be governed by many of the same laws.

Taking a model for deformation in granular media recently developed by Tordessilas et al [3] [4], the potential applicability to metallic glasses was considered. Making simple analogues between the spring constants of the model and the elastic constants of the glass, it was shown that the force chain model can in fact explain several common metallic glass behaviours - correctly predicting a link between Poisson's ratio and toughness for example. While the model is far from perfect and work will be required to link it more fully with glassy behaviour, it would seem clear that metallic glasses can be viewed with some success as a small-length-scale special case of a granular material.

What this work therefore represents is a collection of efforts to take behaviours of metallic

glasses and apply a quantitative approach to explaining them. Whether it be transformation toughening, or shear banding itself, models developed for use in other classes of material can and do work to provide insight into glassy behaviour. Care must be taken to account for the specific nature of glassy systems, but with this caveat it is clear that the science of metallic glasses can be approached from a cross-disciplinary and quantitative viewpoint with very real success.

Chapter 2

Literature Review

2.1 Introduction to Metallic Glass

A metallic glass, or amorphous alloy, is a metal alloy with an amorphous structure showing no long-range order.

First identified in 1960 by Duwez et al [5], these systems attracted much attention. Metallic glasses were initially formed by methods involving very rapid cooling of the order of $1 \times 10^6 \, \mathrm{K \, s^{-1}}$, and this limited casting size. Academic interest truly developed in the 1970s with the development of continuous casting methods [6] [7] allowing for manufacture in a number of useful shapes - albeit still with a very limited sample size.

Work by Turnbull et al [8] initially identified a lot of the early theory of metallic glasses and developed a criterion for glass-forming ability that helped in the identification of new glass-forming systems. This progress led to the identification of the first 'bulk metallic glasses' with low critical cooling rates and sample sizes on the millimetre scale. Chen and co-workers [9] demonstrated the first such bulk metallic glass (BMG) in 1974 in the Pd-Cu-Si system. Various other bulk glass-forming compositions were identified in the following years, with much of the most important progress being made by Inoue et al [10] using the now-commonly-accepted technique of casting in water-chilled copper moulds. These advances led to compositions with critical casting rates below $100 \, \mathrm{K \, s^{-1}}$.

Metallic glasses display a range of attractive properties that give them great potential as an engineering material. High strengths are the most dramatic property, with tensile strengths of 2GPa being not unusual and values as high as 5GPa having been identified [11]. However, corrosion properties are also often excellent [12] and soft magnetic properties have attracted particular interest [13] [14] [15].

Metallic glasses have yet to be commercialised on the large scale. They have been used in sporting goods such as golf clubs and skis [16] and patents held by Liquid Metal have been licensed by Apple but are yet to see significant use, though subsidiary Crucible Intellectual Property has filed patents relating to large-scale production methods [17]. That company's alloys are also licensed to Swatch for use in watches [18].

2.2   Structure of Metallic Glass

2.2.1   Glass Formation and the Glass Transition

One of the most academically active areas in the field of metallic glasses has been in the prediction of glass formation [7]. Metallic glasses typically form when a cooling liquid is prevented from crystallizing. This leads to a supercooled liquid region that then freezes into a glassy configuration at the glass transition temperature T_g. Glass structures, while lacking long-range lattice order across the bulk sample, often have short-range order (on the scale of the nearest atomic neighbours) and medium-range order (on the 2 nm scale) and display some form of consistent structure. [19] [20]

The cooling and glass transition can be characterized by considering the properties of the melt as it approaches T_g. As the system cools, the specific volume decreases. On crystallization, this would cause a sudden drop in volume. However, should crystallization be inhibited, the specific volume will continue to decrease. It undergoes a change in regime at the glass transition and from then on shrinks more slowly.

Similarly the viscosity of glass-forming systems increases as Tg is approached. The nature of the transition has an impact on the glass-forming ability of the system. A strong glass-former will show a gradual transition between viscosity regimes, where a fragile glass-former sees a sudden
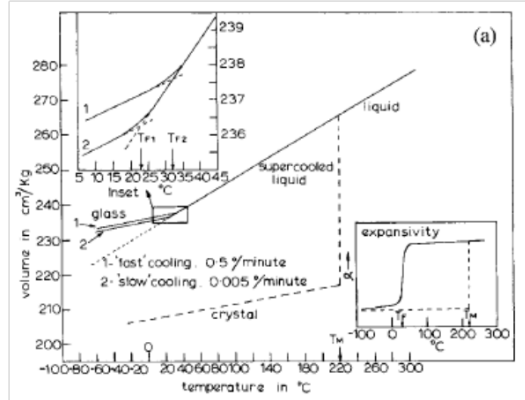
Figure 2.1: Volume of Selenium during cooling from the liquid phase, from Dyre [21]. Volume is seen to steadily decrease as temperature falls. The sudden drop in volume with crystallization can be seen to contrast with the behaviour of glasses, which undergo a continuous transition denoted by a change in gradient after a supercooled liquid region.

change. This can have important structural implications [22].

One view of glassy systems in general relates to structural relaxation (which can here be understood to concern with local structural rearrangement - a more detailed consideration will be given below). A deformation applied to a liquid must operate over a sufficiently long timescale for us to observe liquid behaviour; otherwise we will see elastic behaviour in the same manner as a solid. For a glassy system, the viscosity has grown so high that the relaxation time has passed the experimental timescale, and hence behaviour is solid-like. The glass cannot equilibrate in the time period considered and atomic motion other than by thermal vibration all but ceases [21] [24].

The relaxation time τ follows a non-Arrhenius temperature dependence around a glass transition. Relaxation time can be defined as per Maxwell by [21]:

$$\tau_r = \frac{\eta}{G_{\text{inf}}} \tag{2.1}$$

where G_{inf} is the shear modulus at infinite frequency and η is the viscosity. This then leads to the 'fragility' parameter [21]:

22
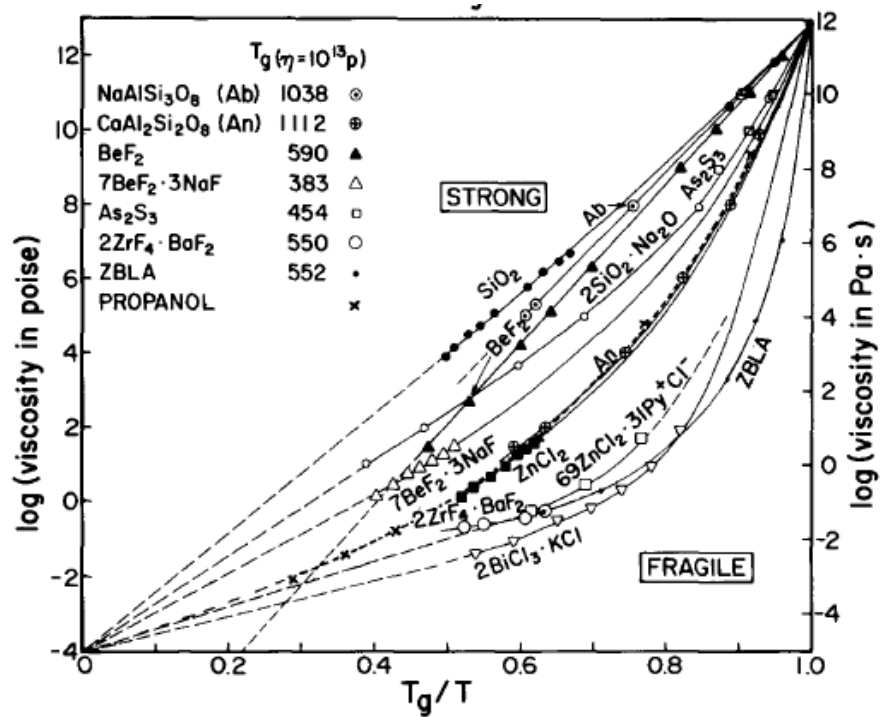
Figure 2.2: Plot showing viscosity in the vicinity of the glass transition, from Angell [23]. For strong glass-formers properties change over a wider region, for fragile glass-formers the transition is sharp.

$$m_f = \left. \frac{dlog_{10}\tau_r}{d(T_g/T)} \right|_{Tg} \tag{2.2}$$

Fragility can be viewed as a measure of the non-Arrhenius behaviour of the relaxation time. (This essentially represents a straight line on the plot in Fig 2.2). A more fragile glass-former is further from Arrhenius and displays a more sudden transition. [21] Fragility can have a significant impact on the structure and properties of a glass, as will be discussed in later sections.

There are a number of criteria that tend to make for a good glass-forming system, amongst others Inoue's empirical rules [25]. In general, multicomponent alloy systems tend to make good glass-formers, since it is harder for these systems to crystallize into a regular structure [7]. Many systems contain four or more elements. A system that tends to phase separate on crystallization will often be a good glass-former, since the requirement for diffusion slows crystal formation. Good glass-forming systems are regularly found near deep eutectic regions of phase diagrams, where supercooling is easy to achieve. Also of importance for glass formation are negative heats of mixing amongst the main constituent elements.

A large difference in atomic size between the constituents helps glass-forming ability (GFA), via what is known as the 'confusion principle'; it is difficult to form a regular structure with such an atomic size mismatch. Of note is work by Miracle [19] suggesting that atomic size mismatch is of structural importance in metallic glasses. More on Miracle's model can be found below - relevant here is that metallic glasses favour clustered structures with clear solvent and solute atoms taking different places in the clusters. Notably, no more than three topologically distinct sizes of solute are possible in such a structure, though different elements of a similar size can share a role. As such, the tendency for atoms of different sizes to favour formation of this clustered structure can aid glass formation. Kokotin et al [26] provide some corroboration of this, showing certain ratios of atomic size favouring non-crystalline structures in a computed binary network of hard spheres.

In general the science of glass forming is still inexact - many models exist which seek to predict and quantify glass formation but none are yet entirely accurate. Perhaps some of the most promising work therefore is the empirical experimental approach of Schroers et al [27], which uses sputtering with multiple evenly spaced targets of specific constituent elements and an organised network of

substrates to deposit a wide range of compositions varied predictably across the sample space. Tests can then be carried out on an entire phase diagram at once, significantly speeding the process of alloy development.

2.2.2 Structure of Glasses

Most materials that the typical materials scientist will encounter will be crystalline in nature, and their structure is usually well understood. From a metallurgist's perspective, metals are most often made up of crystalline grains - regions of organised close packing (anyone who has seen an orange seller stack fruit will be familiar with the idea). The investigation and characterization of crystalline packings and their associated symmetries is a science in itself, and will not be covered here. Instead, the rather less well understood field of the structures associated with glasses will be investigated.

A distinction should be drawn between metallic glasses and network glasses (such as the silica glass commonly known as window glass). It is metallic glasses, with their own peculiarities, that are of interest here - though both materials do share certain key attributes. Both types of glass are characterized by an amorphous structure with no long-range order or crystal symmetry. Their structures are slightly less dense than the equivalent crystals, and for metallic systems it is worth noting the absence of the dislocations that are usually associated with crystalline metals. Bonding in these amorphous alloys is metallic, with the associated lack of directionality - though the precise degree of directional bonding will vary from glass to glass. While they do not have long-range order, metallic glasses are theorised to form a distinctive structure at shorter length-scales.

The definitive work on this area is that of Miracle [19] who proposes a structure of interpenetrating icosohedral clusters, as shown in Figure 2.3. Clusters form around solute atoms, with a co-ordination number typically above ten but that varies around a mean value rather than being fixed. These clusters sometimes overlap to give interpenetration, and are in general packed in space along a hard-sphere model to give medium-range order. Miracle proposes a face-centred cubic packing of clusters as typical. At longer length-scales structural frustrations and internal strains arising from irregular clusters cause ordering to break down, and the model predicts medium-range order on the 1-2nm scale - notably, circa the scale of shear transformation zones, which will be

25
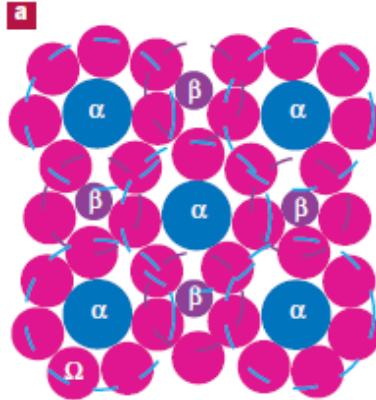
Figure 2.3: 2D demonstration of cluster packing, from Miracle [19]. Solute atoms (pink) form clusters centred on solvent atoms (α and to a lesser extent β). Some clusters can be seen to share atoms. Clusters are packed approximately regularly here, but imperfections will cause this to break down at larger scales.

covered under deformation behaviour in Section 2.3.1 below.

When experimentally investigating structure in metallic glasses a useful method to aid visualisation is the Radial Distribution Function (RDF, also known as the pair correlation function), which represents how density varies with distance from a reference particle and can be obtained from scattering data. In metallic glasses it is usual to see an initial clear peak representing nearest-neighbour atoms, a notable second peak suggesting the presence of medium range order, but no periodicity evident past a few rapidly decaying peaks. [20] Miracle's model [19] is reasonably consistent with experimental RDF, of which an example is shown in Figure 2.4.

Sheng et al [20] also consider cluster-cluster coordination via comparison of ab initio molecular dynamics simulations and experimental RDF from synchrotron radiation. They propose icosohedral packing of the clusters, with order that is short range in cluster terms but medium range when considering atoms. It is notable that solvent-solvent bonds between clusters have been theorised to control elastic properties of metallic glasses via solvent-rich intercluster regions straining preferentially [29]. This can be understood via comparison to a network of springs - the weaker springs in a network will accommodate most of the deformation.

Voronoi polyhedra [30] are of significant use when considering clustering as they can be used
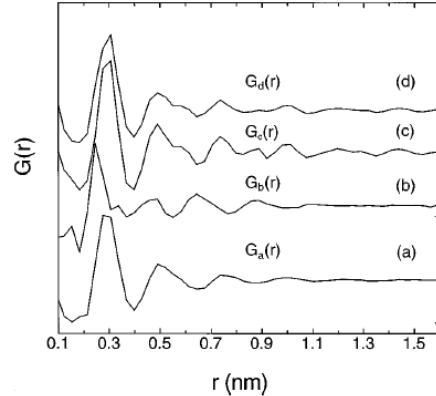
Figure 2.4: RDF for an example Zr-based glass, a) being as cast and b) through d) showing various states of annealing, from Wang et al [28]. A very clear first peak can be seen at circa 0.2 nm, further peaks are present but less distinct and peaks are very diffuse beyond circa 1 nm.

to determine a local coordination number for a given atom. Voronoi polyhedra can be explained as a mathematical method for determining 'ownership' of space around a network of points. This space is divided into polyhedra each centred on a point, with a face for each nearby neighbour - a simple 2D example is shown in Figure 2.5. The area within each polyhedron all falls closer to its central atom than to any other atom in the system.

Despite the large number of possible polyhedra, in a given system certain types of polyhedra make up a significant proportion of those present. This can be investigated via simulation, as with for example the work of Sheng [20] The polyhedra considered are solute-centred with surrounding solvent atoms. Solute-solute bonds are typically avoided. The precise nature of the preferred polyhedra vary with the ratios of atomic sizes present in the system, and some examples are shown in Figure 2.6. These polyhedra can be considered as solute-centred clusters, and they show a narrow variation in volume and coordination number about an average; this hence provides another way of looking at clustering order in metallic glasses.

Between these approaches, a clear picture emerges of the packing arrangements of metallic glasses. Solute atoms form clusters of solvent atoms around them, with co-ordination number varying tightly around an average value. These clusters pack into 3D space like atoms in a crys-

27
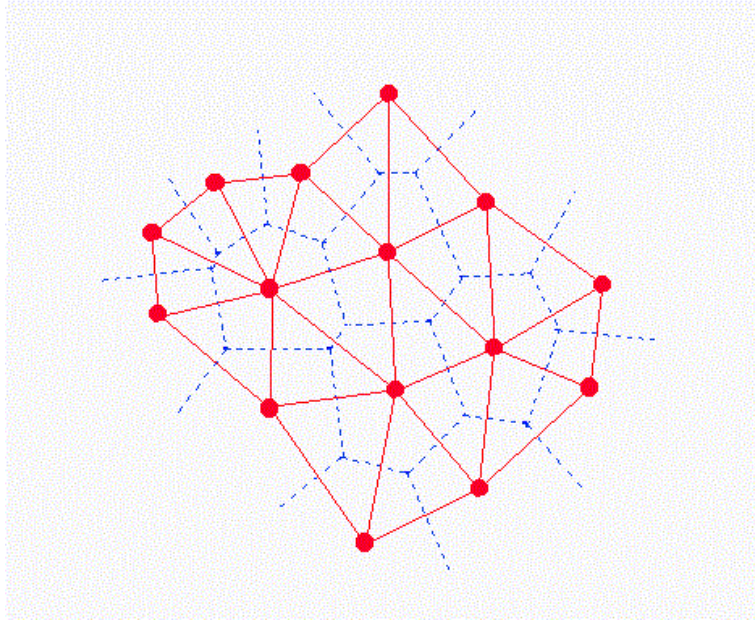
Figure 2.5: Voronoi polyhedra (shown in dotted lines) defined by the space such that each point within the polyhedron is closer to its central atom than any other atom. From University of North Carolina [31]
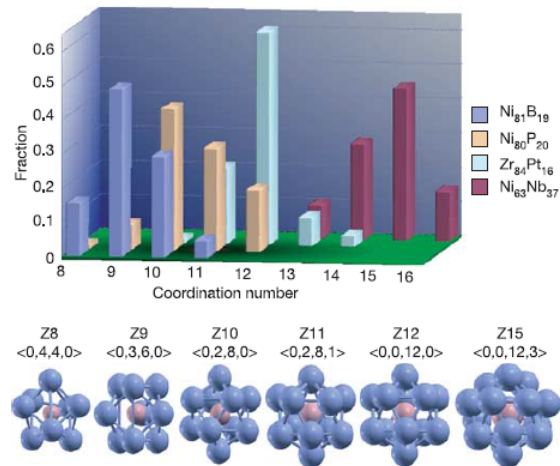
Figure 2.6: Example polyhedra and their distributions in some simulated sample glasses, from Sheng et al [20]. For each glass it can be seen that certain coordination numbers are hugely more common, and that these are clustered tightly about a central value.

talline material, taking on a regular packing order at the short scale and with the solvent-solvent bonds holding the clusters together. Since these clusters are not entirely regular, as the scale increases ordering breaks down, leaving no long-range lattice symmetry. The clusters can be seen as the primary structural unit, and the bonding between clusters has a strong impact on properties.

The imperfect packing of clusters leads to the concept of 'free volume'. This is referenced throughout the subject, and refers to the spare space in the structure that can be used to accommodate deformation (noting that a metallic glass will typically be of the order of 1% less dense than corresponding crystalline phases [32]).

Excess volume in the glassy structure has been observed experimentally by positron annihilation spectroscopy [33]. Positrons have limited lifetime before annihilation, and the sensitivity of this time to electron density can be used to map areas of open volume in a material. Flores et al also use the technique to demonstrate increased such open volume in pre-strained samples, relevantly to dilatant shear banding as explained under deformation behaviour in Sections 2.3.1 and 2.3.3 below.

A seminal work on the subject is Spaepen's paper [34] on free volume and deformation. It is suggested that deformation in a randomly packed assembly such as a metallic glass must carry associated dilatation and breakdown of ordered structure, in contrast with the similarly-dense post-deformation structure in crystals. Spaepen describes the rates of creation and annihilation of free volume. He notes that at low temperature said free volume can accumulate in regions of shear and lead to significant softening, causing shear localization and hence inhomogeneous flow - more on these flow behaviours can be found in Section 2.3. In any case, it is widely accepted that free volume influences physical properties and deformation behaviour.

Free volume can be influenced by processing - annealing a glass below Tg will usually result in 'structural relaxation' where much of the free volume in the structure is removed [35]. This has been observed by positron annihilation spectroscopy [36].

A recent article by Egami in the Journal of Materials [37] is critical of the general application of the free volume model, which does not usually consider positive density fluctuations or non-hard-sphere atoms. He instead frames the issue in terms of local variations in density, which can fluctuate in both positive and negative directions. It is also worth noting that free volume is very much a local phenomenon as well as a continuum one - while the overall proportion of free volume

29
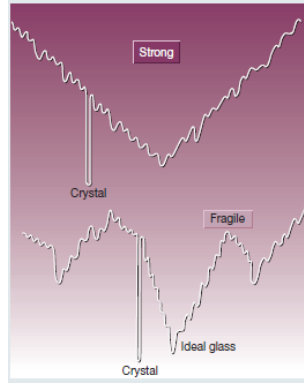
Figure 2.7: Representation of energy landscapes, with x axis representing collective configurational coordinate and y axis representing potential energy. At higher temperatures the system can mount the peaks, at the glass transition it becomes stuck in a single minimum. From Debenedetti et al [38]

in a glass is useful to consider, individual fluctuations in density must by nature be localised in space. Certainly the free volume model should be applied with caution, but it does prove useful for understanding the behaviour of glassy systems and as such retains significant value.

The structural state of a metallic glass can instead be considered by way of its energy landscape. [38] The energy landscape is essentially a representation of the potential energy of the system as molecules interact with their neighbours and sample various configurations. Figure 2.7 shows a representation of an energy landscape. Of primary interest is the nature of the minima (or 'inherent structures') and the barriers that separate them. At higher temperature the system is able to sample more minima; the glass transition corresponds to a point where the system becomes unable to surmount any of the barriers and is trapped in a single deep minimum.

The nature of the energy landscape will vary between strong and fragile glass formers. A strong glass former tends to show a single deep megabasin in its energy landscape (as well as all the usual local minima). A fragile glass-former may show several less deep basins. This is described in Figure 2.7.

Malandro and Lacks [39] have used molecular dynamics simulations to probe the effect of volume changes on inherent structures. They find that volume changes (whether positive or negative) tend to break down the barriers between inherent structures and lead to their disappearance, which
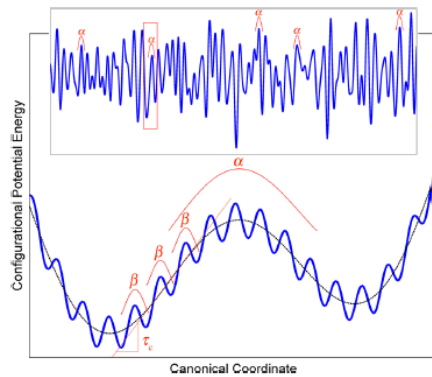
Figure 2.8: Representation of energy landscapes at various scales showing α and β relaxations. Alpha relaxations occur between larger basins, beta relaxations can be seen as smaller local jumps below. From Samwer et al [40]

can make local rearrangements easier.

Samwer et al [40] relate the energy landscape picture to theory applied to glasses in general; identifying the movements between local minima as fast reversible β relaxations and the movements between megabasins as slow α relaxations corresponding to irreversible larger-scale deformation, as shown in Figure 2.8. (These structural relaxations are general features of glasses, typically observed as loss peaks in dielectric relaxation spectra.) They relate the activation energy for α relaxations to overcoming of an Eshelby-type elastic confinement of the STZ (see Section 2.6 below) by the surrounding matrix. Bai et al then relate the β relaxations with STZ activations and show the activation energies for the two strongly correlate. [41] It can hence be suggested that STZs are to an extent reversible and that the system retains a degree of memory until larger-scale plastic α relaxations occur. They go on to suggest that these β relaxations primarily occur in regions of lower local density (drawing back to the free volume theory above).

These β relaxations can be considered as reversible oscillations of stringlike groups of atoms, as can also be seen in supercooled liquids. [42] [43].

The overall picture that can be built up of the structure of metallic glasses is of a series of clustered solute-centred polyhedra arranged into a loose packing. At longer ranges order breaks down due to the irregular nature of the polyhedra, and density fluctuations in this structure lead to

areas of excess volume ('free volume') compared to a crystalline material. This structure forms a complex energy landscape with various megabasins and local minima to sample, with relaxation processes able to rearrange the structure at the small scale between local minima.

2.3 Properties and Deformation Behaviour

2.3.1 Atomistic basis for deformation

The archetypal metallic glass is strong, hard and brittle. While other properties such as magnetic, corrosion or forming properties can attract significant interest, it is the mechanical properties and deformation behaviour of metallic glasses that have attracted the most research. Their high strengths and hardnesses are of significant potential use, but the typically poor ductility and tendency toward brittle fracture that they display significantly limit their application. It is this failure behaviour and its mitigation that is the specific focus of research; the challenge is to consistently engineer ductility into these materials - a challenge that has to some extent been met, but fundamental understanding remains lacking and much progress remains to be made.

At high temperatures or under very slow strain rates, metallic glasses can flow homogeneously with deformation spread throughout the structure. Of more interest to most researchers however is the inhomogeneous regime in which deformation is localised into shear bands, since this will control brittleness or ductility, and it is this regime that will be considered here. A sample deformation map is shown in Figure 2.9, demonstrating the homogeneous and inhomogeneous regimes.

The deformation behaviour of most bulk metallic glasses in the inhomogeneous regime is characterised by a large elastic region of circa 2% elastic strain, followed by catastrophic failure without plastic flow. Sample stress-strain curves are shown in Figure 2.10. During deformation of a metallic glass, strain tends to localise into shear bands. The typical explanation for this is that ahead of the tip of an advancing shear band, free volume tends to accumulate and the structure therefore dilates, leading to strain softening - the opposite of the behaviour normally seen in crystalline alloys. This often leads to catastrophic failure along a single shear band resulting in fracture. [44]

Shear banding involves significant adiabatic heating, as shown by Greer and co-workers [46]
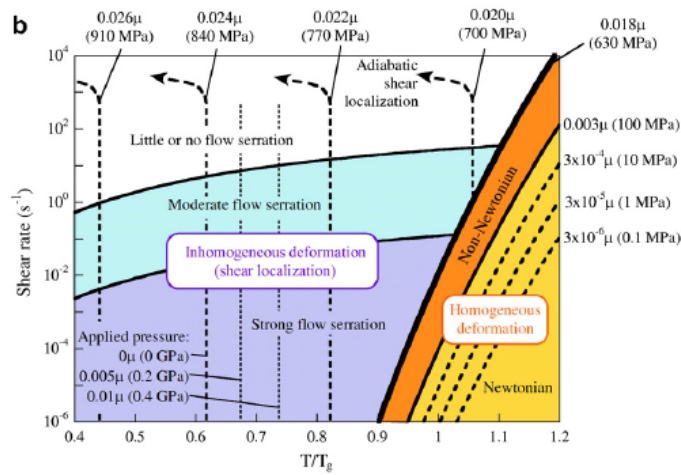
Figure 2.9: Sample deformation map. Axes are shear rate vs homologous temperature. At high strain rate and low T, flow is inhomogeneous. From Schuh et al [44]
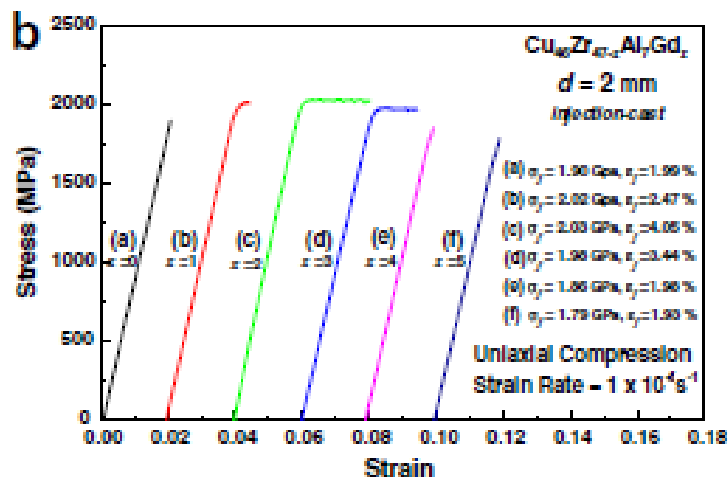
Figure 2.10: Sample stress-strain plots under compression for $Cu_{46}Zr_{47-x}Al_7Gd_x$ metallic glass. Note that some curves do display limited plastic strain, but most show significant elastic strain followed by immediate failure. From Park et al [45]

who used melting in a tin coating to show heating at the surface. It has been argued by some that this heating might be the primary source of shear softening and hence the driver for shear banding [47]. However, detailed analysis of the heat transfer involved suggests that this model would predict the wrong size scale for shear bands at low strain rates, and as such it can be discounted, leaving shear-induced density fluctuation as the primary mechanism [44] [48] [49].

Shear bands in metallic glasses have been observed by microscopy and simulation to have thicknesses typically in the vicinity of 10 nm [48] as distinct from the 10-500 μm typical in polycrystalline alloys. Taking experimental results for density changes and assuming all dilatation occurs inside shear bands suggests that this dilatation is 10% or greater - though it may instead be argued that dilatation is spread through more of the material [44] [50]. The interiors of shear bands show significant structural disordering, evidenced through scattering measurements. [51] [52]

In general deformation in metallic glasses is strongly dependent on strain rate, size and geometry effects. In small samples for example significantly more plastic strain can be observed. [44] [53] [54] The most experimental evidence exists for millimetre-scale samples at slow strain rates, and it is this regime that receives the most attention theoretically. High-temperature flow is nonetheless important for forming processes and does hence see significant interest.

While they may be the method by which large-scale deformation is often accommodated and are typically the route to failure, shear bands do not by themselves explain how deformation is accommodated at the atomic level. If it is being taken that shear bands occur due to accumulation of free volume (which can also be understood as a reduction in local density), then the mechanism by which this local density is reduced must be understood. At the atomic level, metallic glasses lack the dislocations that enable deformation in crystalline alloys. This is a contributor to their strength, since deformation processes will tend to be high-energy. Nonetheless, this means that deformation cannot be accommodated by dislocation motion as would normally be the case.

Instead, the currently theorised mechanism for deformation involves what are commonly known as 'shear transformation zones'. First identified by Argon [55] in 1979, the model concerns groups of atoms (up to perhaps a few hundred) moving collaboratively to enable deformation via inelastic shear. A shear transformation zone (STZ) is defined by its short-term existence; it is not a permanent defect like a dislocation in a crystal. A simple schematic of STZ operation is shown in Figure 2.11.
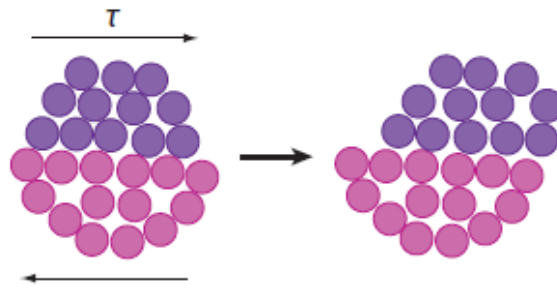
Figure 2.11: A representation of the operation of a typical STZ. From Chen [56]

The extent of the STZ is not tightly defined - though estimates at a size can be made by considering the magnitude of atomic displacement with respect to the matrix.

It is important to note that the operation of an STZ implies a local dilatation of the structure, and that the local structure may retain this higher free volume after its operation. [55] [44] Plastic deformation in metallic glasses is essentially an accumulation of the atomic movement accrued through STZ operation - conversely, the accumulation of STZ-created free volume is theorised to be the source of shear banding and hence in many cases brittle failure.

The exact mechanisms of deformation are still poorly understood. It is very difficult to model STZ operation and glassy behaviour in general. In particular the structure cannot be easily modelled, since cooling from the melt operates on a far longer timescale than sufficiently small-scale models can reach.

This makes a full understanding of STZ operation difficult, although attempts have been made - Homer and Schuh for example consider STZs via an Eshelby inclusion model (see Section 2.5.2) and attach potential STZs to points on a triangular mesh [57]. Their model outputs for low-temperature deformation in unequilibrated samples a transient period where a few difficult-to-activate STZs associated with large deformation assemble in a spatially clustered region and form a nascent shear band. After this, straining is rapid as a shear band assembles. In equilibrated samples, deformation is instead homogeneous. Example model output is shown in Figure 2.12.

Perhaps the best way to understand transformation zones is to refer back to the energy landscape (see Figure 2.8). The system in its undeformed state finds itself in small local minima. An activation energy is required to escape these minima and move to adjacent ones, resulting in deformation.
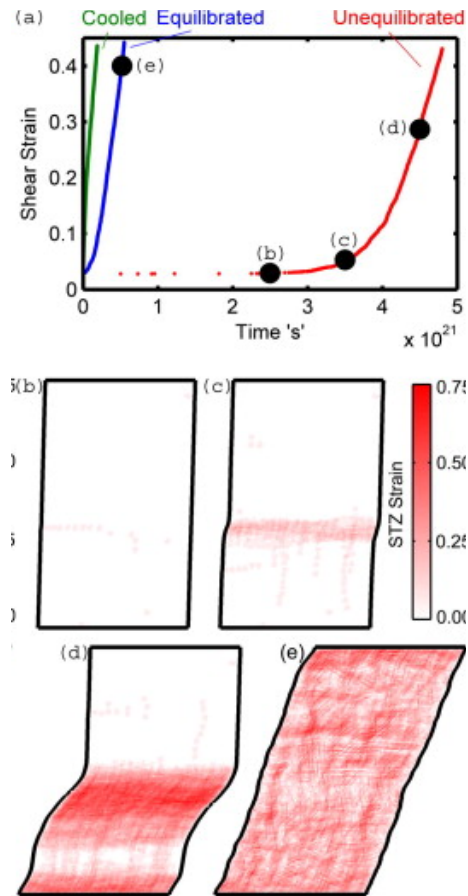
Figure 2.12: a) shows strain-time data for different structures deformed at low T. Note the time delay before rapid straining in the unequilibrated case. b)-d) are different stages of deformation in an unequilibrated sample, showing STZ assembly into a shear band and then straining along that band. e) shows homogeneous deformation in an equilibrated sample. From Homer and Schuh [57]

This energy can be thermal (as in the system above the glass transition) or it can be mechanical. Small amounts of stress allow for limited hopping between small local minima - activated where the barrier heights are lowest, ie weak spots in the structure, typically regions of low density. These correspond to the β relaxations [42] [40] [41]. To allow for large-scale deformation, the system must move between larger energy basins - this motion corresponding to the α relaxation, but also being made up of the collective activation of many smaller events, ie collective STZ action.

It must be noted that the above has still not explained in detail how it is that STZ accumulate into a shear band. The dominant theory would appear to be that STZ operate at weak spots in the structure (whether these be local density fluctuations, stress concentrators, or the like). These STZ activations have an impact on the surrounding material. The local density must decrease to accommodate the transient state of deformation, and does not necessarily return to its original state afterwards [55]. This will have an impact on the local properties - the elastic constants will fall [58] [59], and the energy barriers separating local minima in the energy landscape are reduced [39] (making structural rearrangements easier). In effect, the local region can be viewed as becoming more liquid-like in character [60], or more structurally disordered [60] [61], as can be observed in the bulk shear band (observations of individual STZ being extremely difficult, requiring as they do in situ work).

In any case, activation of an STZ makes the local structure more receptive to further activation of deformation. At some point, regions where STZs activate - now weak points themselves - reach a percolation threshold and large-scale deformation is able to occur along the band that forms [62], with collective action of a large number of STZ. The precise nature of this percolation is debated - whether STZs activate throughout the structure and shear banding occurs when they reach percolation, or whether a region of STZ action catalyses adjacent regions to activate via behaving as a stress concentrator. The activation of a shear band can also be viewed as the accumulation of sufficient mechanical strain energy to overcome the inherent states of the energy landscape and cause the band to become akin to a supercooled liquid; essentially mechanically induced reversal of the glass transition [63]. Liu et al support this by relating the shear yield strength to the glass transition temperature [64], though the analysis makes a significant approximation via considering only the work put into shearing the system, neglecting temperature and volumetric effects.

Figure 2.13: Vein patterns on the fracture surface of a $Pd_{77.5}Cu_6Si_{16.5}$ metallic glass. From Pampillo et al [69]

It is important to realise that this implies STZ activation before macroscopic plastic yield - this has been verified in simulation [65] and experimentally [66]. STZ action can be considered anelastic - it is locally plastic, but can be reversible and does not necessarily carry large-scale plasticity.

2.3.2   Mechanics of failure

It has been established that in the inhomogeneous regime STZ activation concentrates into dilatant shear bands, with attendant local strain softening. The mechanisms by which these shear bands develop into macroscopic failure should however also be investigated.

Experimentally observed fracture surfaces in bulk metallic glass samples under compression display different morphologies dependent on the nature of failure. Ductile failure leaves distinctive 'vein patterns' as shown in Figure 2.13. Brittle failure leaves a surface that initially appears smooth but in fact displays similar vein patterns and some evidence of microvoid damage on a far smaller scale. [67] In some samples regions of river patterns attributed to crack microbranching can be observed. [68]

This was explained by Argon [70]. Consider a model of meniscus instability as can be seen in liquids or grease layers - a blunted crack breaking down into fingers that advance into a fluid region

38

(in this case, fingers of air moving into liquidlike regions in the shear band, though this would seem to suggest a liquid region rather wider than the shear band itself). The waveform associated with this behaviour shows a good correlation with the vein pattern spacing in experimentally observed glasses. [70] In general vein pattern spacing carries information about the toughness of the glass - ductile glasses tend to show larger patterning. Xi et al relate the size of these features to the size of the plastic zone, relating small-scale structures to small plastic zones and hence low toughness. [67]

Donovan and Stobbs [51] mention microvoid formation within shear bands in metallic glasses. It is nowadays thought by some that the fluid meniscus model described above is modified by the formation of very small voids ahead of the crack tip. These voids interfere with rapid crack advance. According to Pan et al, the spacing of the voids is influenced by the crack tip shape and hence the stress state ahead of the tip; and the periodic appearance of voids that disrupt crack advance results in the observed regular spacing of striation patterns [71]. This is similar to Xi's suggestion of structure size relating to plastic zone size [67], as this will influence the location and nature of void formation.

The shear band angle has been observed to fall at an angle that deviates from the plane of maximum shear stress at $45°$. (It tends to fall at $43°$ from the loading axis under compression and $56°$ in tension instead.) [72] [73] [74]). In order to explain this, researchers have sometimes used yield criteria more typically associated with granular media.

Initial work focussed on comparing the Von Mises and Mohr-Coulomb yield criteria [73] [74], which attempt to define a 'yield surface' such that the point of yield can be defined for any stress state. The Mohr-Coulomb yield surface is defined via $\tau_y = \tau_0 \pm \mu\sigma_n$ where τ is shear stress at yield, τ_0 is yield shear stress for no applied normal stress, σ_n is normal stress on the shear plane, and μ is related to internal friction and is negative for tension, positive for compression. This yield criterion takes the effect of normal stress on the shear plane into account - the effect of pressure on frictional behaviour at the shear plane can have a notable impact on yield, raising or lowering the shear stress required. Mohr-Coulomb can to an extent explain shear band angles other than $45°$ in tension and compression. More explanation of Mohr-Coulomb theory is given in Section 2.6.

Since that initial work, however, the Drucker-Prager criterion has been applied successfully by Zhao and Li [76]. They criticise the application of Mohr-Coulomb criterion as it predicts symmet-

39
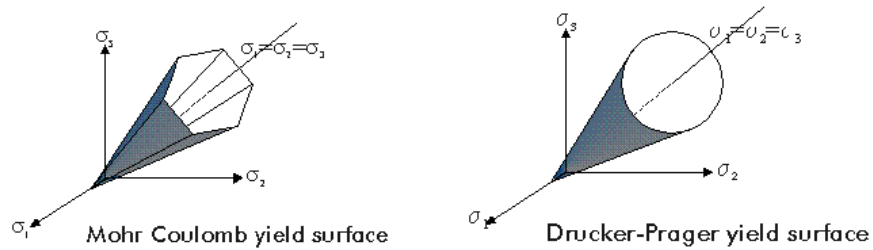
Figure 2.14: Mohr Coulomb and Drucker Prager yield surfaces. From PISA [75]

rical deviation from $45\,^\circ$ in compression and tension, which is clearly experimentally observed to not be the case. Mohr-Coulomb does not take into account dilatancy during deformation, treating the system as simply two bulk regions sliding across each other. Drucker-Prager, by contrast, models the effect of hydrostatic pressure and not just normal pressure on the shear plane. Zhao and Li's approach introduces a term relating to free volume creation to model this pressure. The ratio of volume change rate to shear rate correlates directly with change in shear band angle in their analysis, and this can be different in compression and tension, hence explaining the experimental observation.

2.3.3 Toughening Mechanisms

The lack of effective mechanisms for blunting stress concentrations at defects and crack tips, and the tendency toward catastrophic failure along single shear bands, has led to metallic glasses being seen as a generally brittle class of materials. However, a number of approaches exist that allow glasses with significant ductility to be engineered - indeed a glass recently developed exhibits a combination of strength and toughness that is unprecedented in the material world. [77] Toughening is often approached via encouraging the propagation of multiple shear bands to distribute deformation, hence the objectives of many researchers have been to encourage shear band initiation while restricting propagation.

A selection of approaches to toughening will be covered here. These can be split between intrinsic and extrinsic methods - the former adapting the properties and structure of the glass itself

to increase ductility, and the latter typically involving the formation of composites (which will be detailed in Section 2.4).

In general, more fragile glass-formers will tend to form more ductile glasses. These glasses tend toward easier activation of STZ (easier β relaxations and hence local atomic rearrangements) which can allow a degree of blunting at stress concentrators such as crack tips. Their structures contain more free volume, which further helps accommodate deformation and hence enable blunting. [78] Therefore, when considering glasses for applications requiring toughness the strongest glass-formers may in fact not be the ideal candidates.

It should also therefore be understood that annealing of metallic glasses tends to lead to a fall in toughness and is hence not an appropriate technique for improving ductility as might be expected in crystalline alloys. Annealing leads to structural relaxation and the annihilation of free volume along with a move toward a structure reminiscent of a strong glass-former. [79] [80]

Ductility has been shown to correlate with various elastic properties of glasses. The work of Lewandowski, Greer and Wang [81] relates toughness to the ratio of the shear modulus G and the bulk modulus B, demonstrating a trend whereby glasses with G/B under 0.41 show toughness (with fracture toughnesses in the many tens of $\mathrm{MPa\,m^{-1/2}}$) whereas G/B over 0.43 leads to brittle behaviour (fracture toughnesses notably less than $10\,\mathrm{MPa\,m^{-1/2}}$). It should be noted that G/B and Poisson's ratio ν are closely related and are used almost interchangeably in the literature when discussing toughness in glasses ($\nu = (3B - 2G)/(2(3B + G))$), so this behaviour is sometimes expressed in terms of a critical ν. Figure 2.15 shows Lewandowski et al's plot of fracture energy against G/B.

A qualitative explanation for this behaviour is provided by Schroers et al [82] who suggest that low shear modulus allows for easy formation of shear bands and the relatively large bulk modulus inhibits the transformation of existing shear bands into cracks, hence favouring propagation of multiple shear bands rather than cracking along one catastrophic band. G controls the resistance to shear, and K the resistance to dilatation - which is required for the formation of Mode I cracks [63]. Nonetheless a quantitative link between the elastic moduli and fracture energy has yet to be derived in amorphous metallic systems.

The elastic constants are fundamentally related to the nature of the bonding in the system [63]
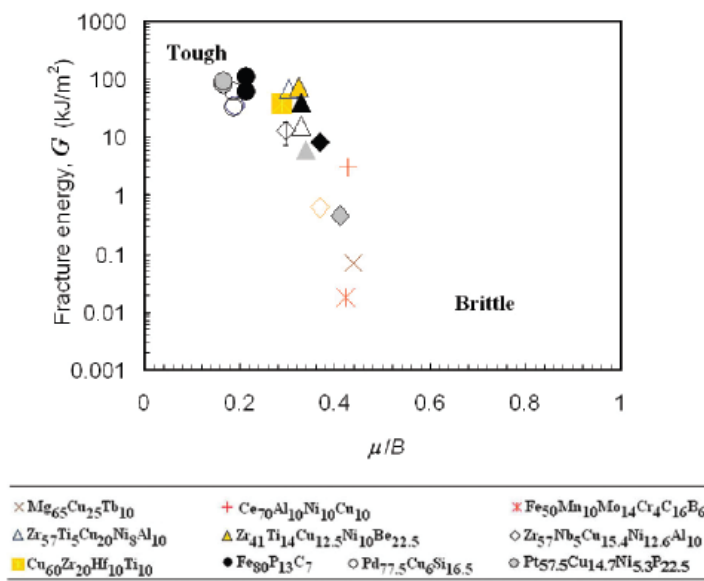
Figure 2.15: Fracture energy G against ratio of shear to bulk modulus μ/B for a series of glasses - note different notation. Observe the very rapid fall in fracture energy (and hence toughness) in the region from $\mu/B = 0.41$ to 0.43. From Lewandowski et al [81]

[83] [84] and to the atomic packing [63]. The shear modulus will relate to the distortion and rotation of bonds, while the bulk modulus depends more closely on the atomic packing and the compressibility of bonds. These bonding states will themselves be influenced by composition and processing. Wang's analysis views the elastic constants as easily measurable indicators of the fundamental state of the system, with a bearing on properties such as fragility and glass-forming ability [78], energy landscape [85] and shear transformation zone size [86].

Novikov and Sokolov [87] show a correlation between fragility m and the ratio G/B, or alternatively Poisson's ratio ν, in nonmetallic glasses - suggesting a more fragile glass former is likely to be more malleable as a glass. Wang et al [78] expand this to metallic glass and show a similar trend, albeit with a different proportionality. This therefore suggests a direct link between the intrinsic mechanisms most often related to toughness. (It must be noted, however, that the data is based on a narrow range of available fragility values, and involves somewhat inaccurate estimation of elastic properties at T_g from their room temperature equivalents, and hence requires further investigation.)

Pan et al [86] show a correlation between Poisson's ratio ν and the size of shear transformation zones. STZ volume is already correlated with toughness; Johnson and Samwer in their cooperative shear model [88] suggest that with a larger STZ size less activations are required to form a nascent shear band and hence multiple shear bands are favoured. As per Wang et al [58] [59] elastic constants change with pressure, with B varying more quickly than G. They will also vary with temperature.

Plummer and Todd [89] [90] identify statistically significant isomechanical groups in metallic glasses, initially selected along the lines of Poisson's ratio. These groups may be linked by their tendency toward directional bonding and liquid-like character, as expressed via the use of C_{ij} elastic constants. Using a Blackman diagram (a plot of C_{12}/C_{11} against C_{44}/C_{11}), they suggest that glasses with a larger positive deviation from zero Cauchy pressure ($C_{12} = C_{44}$), which corresponds to more directional bonding, are more brittle. Similarly proximity to the Born instability criterion (C_{44} and $(C_{11} - C_{22})/2$ zero) indicates liquidlike character and hence toughness. Egami [85] suggests that more directional bonding reduces Poisson's ratio, once again linking the inherent state of the material to the more easily measurable elastic properties.

It is worth noting that elastic properties, being representative of the state of packing and bonding

43

in the glass, will vary locally as well as having bulk applicability. The concept of free volume, initially coined by Argon [55] to explain shear banding in metallic glasses, can now be understood as the local variation of an order parameter [44] [62] - whether this be expressed as effective temperature (with respect to glass transition), structural disorder, local density [85] [37] or indeed elastic moduli [78] [63]. Certainly it is the case that the local structure of glasses can and does vary, and that this variation can have an important effect on properties. Local variations provide the weak spots at which shear transformation zones preferentially operate. Their prevalence and distribution can serve to control the initiation and propagation of shear bands, and hence influence malleability. Local variation of elastic moduli is shown experimentally by Wagner et al [91].

Various sources have shown an increase in plastic strain before failure on prior mechanical treatment of metallic glasses, such as cold-rolling. [92] [93] One proposed explanation is that additional free volume is induced in the structure. Another concerns induced inhomogeneity - soft regions in the structure that facilitate shear band activation and harder regions to prevent catastrophic propagation of a single shear band. This approach is demonstrated by Scudino et al [94] who engineer ductility via heterogeneity induced by imprinting with a ridged tool. Pre-deformation of metallic glasses to induce preactivated shear bands has also been seen to lead to significant ductilization, with behaviour dependent on shear band orientation [95]. Greer et al apply shot-peening to metallic glasses and show increased ductility, explained via increased shear band density and lower odds of surface cracking [96]. Loading of metallic glasses in the creep regime, well below yield, has been shown to lead to rejuvenation toward more plastic behaviour, along with decreased density indicative of more free volume in the structure [97].

Perhaps the most interesting idea to arise from the work on preloading is that of the effect of heterogeneity. If the structure of the glass consists of distinct soft and hard regions, shear bands can activate more easily in the soft regions. However, propagation will lead them to a hard region where their movement is impaired, at which point it is likely in a heterogeneous structure that there is another soft region that will now be favoured for STZ activation and hence shear band formation. As such, if the heterogeneity is of a scale such that shear bands don't propagate far enough to form cracks, macroscale deformation can occur without immediate failure. This then again draws back to the importance of local rather than bulk properties. According to finite element simulations

performed by Cheng, Jiang and Dai [98] it is not so much the amount of free volume present that is an issue, as its distribution. A large amount of homogoneously distributed free volume may lower the yield stress (also associated with a fall in Young's modulus E) but it will not have the same effect on toughness as distinct regions of high free volume concentration surrounded by denser regions. Free volume dispersion, rather than its overall concentration, hence controls ductile behaviour.

A number of approaches have been identified here that can be followed in order to engineer toughness in metallic glasses. Some benefit can be obtained in materials selection by choosing glasses with high fragility, significant structural inhomogeneity and a low ratio of elastic constants G/B. Further benefit can be obtained from processing, eg by cold rolling or ridged imprinting to obtain an inhomogeneous microstructure. Ductile bulk metallic glass would seem to be an entirely achievable goal, though a full quantitative description linking structure and properties remains to be found.

2.4   Metallic Glass Composites

While the above intrinsic methods can lead to good toughness, there also exist extrinsic methods for toughening. One of the most successful techniques for engineering plasticity in metallic glasses has been to form a composite with crystalline phases. Using these techniques, high ductilities have been achieved [99] [100] [101] - plastic strain to failure in compression usually between 5 and 10% in compression but reaching as high as 50% [100] in extreme cases.

Composities can be split into two broad classes - in situ and ex situ composites. The ex situ composites are formed with reinforcement introduced separately, rather than a crystalline phase of the glass-forming alloy. Typically these are manufactured in one of three ways. Particles can be added to the melt before cooling [102] [103]. Glass can be cast around preformed networks of reinforcement [104]. Glasses can be formed into laminates with layers of crystalline material [105] [106]. In one recent paper a composite with polymer reinforcement was demonstrated [107].

This review will focus primarily on the in situ composites, formed from the glass-forming alloy itself. Typically the material is cast in a partially glassy state through careful choice of composition or cooling rate. However, an alternative approach is to anneal the glass to a stage of partial devitri-

fication (noting that this will have an impact on the free volume distribution and hence properties of the glassy phase).

A number of morphologies of metallic glass matrix composite have been developed. In some systems, solidification produces a dendritic microstructure that can lead to considerable plasticity [99] [108]. Work by Hays and co-workers [99] identified behaviour whereby shear banding was organised into domains whose size scale corresponded to the primary dendrite axis lengths. Individual shear band separation appeared to be influenced by dendrite arm spacing. They observed some true ductility in tension, and attribute this in part to work-hardening in the soft dendrite phase.

Hofmann et al [109] extend this work by comparing the domain size with the size of the plastic zone. Essentially, they suggest that domains can be treated as individual samples, and hence dendritic microstructures can reduce the effective sample size leading to plastic behaviour. For this to be effective therefore dendrites need to be below a certain spacing. Eckert et al [110] on the other hand show a system where dendrites are too fine to adequately impede shear band propagation, and hence mechanical behaviour is similar to that of the monolithic glass. As such, it can be concluded that dendritic microstructure alone is not sufficient for plasticity and the microstructure must be carefully engineered to optimise behaviour. Shear bands in a sample dendritic glass can be seen in Figure 2.16.

This behaviour might be compared to the use of inhomogeneous microstructures to initiate shear bands but restrict their propagation in purely amorphous glasses as explained above [98] [94]. The crystalline phases can act as stress concentrators, making shear band initiation easier. In some cases stress concentration near a crystalline phase may be sufficient to activate shear banding locally but not to propagate it once away from the local stress field, hence allowing a degree of plastic deformation without failure. Crystal-glass boundaries can also deflect shear bands and prevent their continued propagation, resulting in impeded propagation, although in general crystalline particles cannot stop propagating shear bands entirely, tending to deform or fracture. Nonetheless, this may be sufficient to encourage activation of shear banding elsewhere at another stress concentrator, or to disrupt shear bands before they are fully developed, and hence obtain a degree of ductility. [44]

Other morphologies are reviewed by Schuh et al [44], who draw together data from a large number of papers to show trends in behaviour and properties of metallic glass composites - shown

46
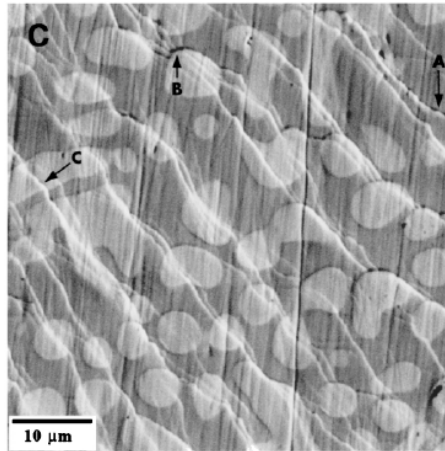
Figure 2.16: Shear bands in a dendritic bulk metallic glass composite under compression. From Hays et al [99]

in Figure 2.17. In general, they observe that below a reinforcement volume fraction of circa 0.3, strengths cluster around rule of mixtures values. Above this volume fraction, values diverge - with dendritic composites typically stronger than one would expect from rule of mixtures, and nanocrystalline systems less strong. Nanocrystals also provide less benefit in terms of plastic strain to failure in compression than larger phases.

It is worth mentioning that nanocrystallization can occur inside shear bands. [111] This occurs even during shear banding in nanoindentation (hence low amounts of heating) [112], suggesting it is not purely a thermally driven effect but that local structural rearrangement (such as free volume generation) plays a role. Crystallization tends to occur only within the shear band itself, rather than the significantly wider heated zone [111]. This further suggests a rearrangement rather than a thermal basis.

Phases formed are not always those that would be expected from annealing [113]. This is likely due to having the same composition as the glass and hence not requiring long-range diffusion to operate (which would lead to wider scale crystallization if active). There is some suggestion that crystallization may in some cases occur after rather than during shear banding. Wilde et al show nanocrystals forming after deformation, when limited degrees of heating well below the glass transition temperature are applied [114].

47
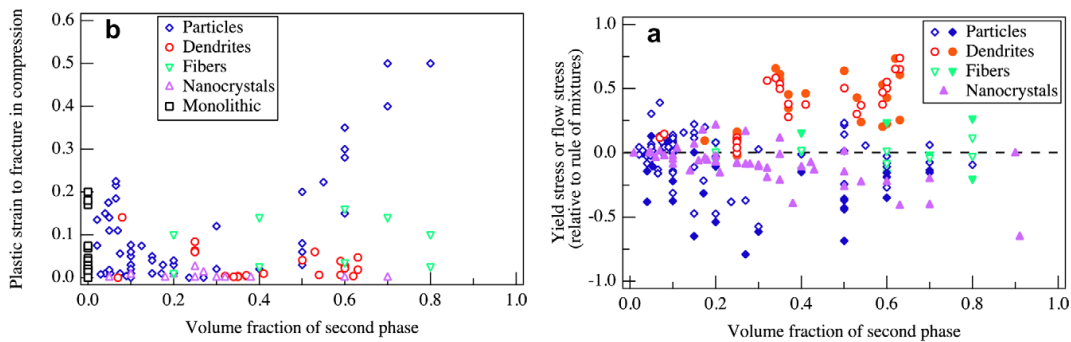
Figure 2.17: Strengths and plastic strains to failure against crystalline volume fraction for various morphologies of metallic glass composite. From Schuh et al [44]

Glasses that nanocrystallize during deformation can show significant plastic strain before failure. Chen et al [113] show shear bands widening significantly around nanocrystals. This reduces elastic shear stress and strain around the particle and hence incentivises other shear bands to activate (at higher stresses) instead. Distribution of deformation across multiple shear bands is therefore promoted, explaining the observed ductility.

Hajlaoui and co-workers [115] carry out in-situ deformation under TEM, and show that an initial dispersion of very small particles (circa 2 nm) increase in size and volume fraction under deformation. The system then exhibits behaviour like a semi-solid slurry with an increasing solid volume fraction. Essentially, as more and more of the shear band is made up of nanoparticles, viscosity increases and impedes propagation. This can to an extent be compared to crack blunting in crystalline metals or jamming transitions in granular media - a mechanism driven by advance of the crack or shear band disincentivises propagation and prevents that defect from becoming catastrophic.

2.5 Transformation toughening and its use in metallic glass composites

It has been proposed that transformation toughening in some metallic glass matrix composites may lead to work-hardening and ductility [1]. In order to understand the nature of this behaviour, it is important to first understand the nature of martensitic transformations and how they induce toughening in other classes of material.

2.5.1 Martensites and Shape Memory

Martensitic phase transformations are a form of diffusionless phase transition. Atoms collaboratively move to transform from a high-symmetry high-temperature 'austenite' phase to the low-temperature, lower-symmetry 'martensite'. [116]

It is important to note the lack of a diffusion component to martensitic transformations. Atoms retain their correspondence; ie neighbours before the transformation will remain as neighbours afterwards. This is particularly important in metallic glass composites since should diffusion be operating the glass would tend to crystallize.

In a normal, or 'non-thermoelastic' martensite, the martensite crystals form and grow rapidly to a final size then stop. If the sample is cooled further or held at temperature for a longer time they will not change in size and grow further. By comparison, 'thermoelastic' martensite crystals vary in size with sample conditions. The key to this is in the energetics of the transformation.

The driving force for the transformation is given, for a lens-shaped crystal with radius r and average thickness t, by:

$$\Delta G = \pi r^2 t \Delta g_c + 2\pi r^2 \sigma + \pi r t^2 (A + B) \tag{2.3}$$

where Δg_c is the chemical free energy change per unit volume, σ is the interface energy per unit area, At/r is the elastic strain energy per unit volume and Bt/r is the plastic strain energy per unit volume. In a thermoelastic martensite, the terms relating to interface energy and plastic strain energy are negligible, and hence:

49

$$\Delta G = \pi r^2 t \Delta g_c + \pi r t^2 A \tag{2.4}$$

This is an important distinction - it suggests that the crystal size is driven by an equilibrium between the elastic strain energy and the chemical energy change on transformation (which will vary with temperature). Hence, as temperature is varied, the size of martensite crystals will grow or shrink reversibly. Notably, however, a condition of thermoelastic martensite (which is involved in the shape memory effect) is that there should exist negligible volume change on transformation.

For any austenite phase there will be several related martensite phases, with the same symmetry but different orientations. These are known as 'correspondence variants' and are essentially twinned structures of one another. The transformation from high-symmetry to low-symmetry phase will tend to have an associated volume change and shape change. In order to accommodate this, typically multiple correspondence variants will tend to self-organise so as to minimize this change and hence lower the strain energy of the system. The transformation from austenite to thermoelastic martensite and back is crystographically reversible - you will always get the parent austenite phase back, where in other martensites you might form one of several possible austenites on reheating.

It can be possible to move the twin boundaries separating the correspondence variants and hence to transform the structure into different variants, altering the shape of the martensite region. It is in fact possible to transform the whole of the martensite into one variant, giving a significant reversible plastic deformation. Until this point is passed atoms retain their neighbours during the deformation - after that limiting strain is reached and the structure is all one variant, further straining in the same direction will be irreversible.

This reversible plastic behaviour is the basis of the shape memory effect, and the associated pseudoelastic phenomenon. On deformation below the austenite finish temperature, the martensite elements deform via a change between correspondence variants through moving the variant boundaries. On heating, all the variants transform back to the same austenite and hence the original shape is recovered. Pseudoelasticity is basically the same thing - a shape recovery driven by reverse transformation. It is just that in the pseudoelastic case the sample is above the austenite finish temperature Af and so the structure initially contains no martensite - unstressed martensite is

entirely unstable at these temperatures. On loading martensite becomes energetically favourable, forms and elongates to accommodate the stress. On removal of the stress the martensite becomes unstable and returns to austenite leading to shape recovery via the retained atomic correspondence.

2.5.2 Transformation Toughening

Transformation toughening is a mechanism that has been used in a number of materials throughout materials science to promote ductility. Perhaps the best known example would be transformation toughened zirconia, as identified originally by Garvie and co-workers in 1975 [117].

Historically, transformation toughening, or transformation-induced plasticity (TRIP) was first identified in Germany in the 1920s. The first intentional investigation appeared in the 1930s. Of particular use concerning the history and theory of TRIP is the review by Fischer et al [118] published in 1996.

Essentially, the principle is that when a crack propagates through a material, it creates a stress field ahead of it. This stress field has an influence on the thermodynamic stability of the material, and can cause a phase transformation. The volume change associated with this phase transformation exerts a compressive stress field on the advancing crack, and also energy is absorbed in driving the transformation. This tends to impede crack propagation and hence promote ductility. [119]

TRIP steel is a very notable use of the behaviour. Steel alloys have been developed in which austenite is retained, and can transform to martensite under deformation. This leads to significant work hardening and toughening, producing an exceptional balance of high strength and ductility. It is primarily the cost of the necessary alloying elements that limits their application.

Over the years, a large number of mechanical approaches have been developed to explain the behaviour of transformation-induced plasticity - mostly concentrating on steels and on ceramics such as zirconia. Consider for example the early work of Greenwood and Johnson [120] and Magee [121] in identifying two mechanisms of plasticity. Greenwood's mechanism relates to small-scale internal deformations in the weaker phase induced by volume mismatch, which can be oriented by an applied stress to cause plastic deformation. Magee instead considers the formation of martensite plates in an orientation defined by the applied stress, leading to plastic strain. Leblond et al [122]

51

show that plastic strain can be decomposed into classical and transformation components, the latter consisting of two terms related to Magee and Greenwood's mechanisms. Models of the toughening effect itself tend to follow one of two methods - either considering the work of fracture, or the stress shielding effect of transformation via fracture mechanics.

Perhaps one of the most notable stress shielding approaches is that of McMeeking and Evans [123]. Their approach is designed to be easily compared with experiment. As such, they consider the impact of transforming particles on the stress intensity factor at the tip of an advancing crack. A transformation zone is defined by a critical stress for transformation, with the calculation for the zone radius taken from earlier work by Evans and Heuer [124].

To understand their work it is useful to first consider the work of Eshelby [125] [126]. Consider an untransformed particle constrained within a matrix. Remove it from the matrix and let it transform, with an associated transformation strain. Then, apply surface tractions to the transformed particle until it fits back into the hole it left in the matrix. By linear superposition, equivalent forces will be present in the matrix to constrain the particle. The nature of these forces has been calculated for a variety of geometries and mechanical property mismatches, though McMeeking and Evans use long cylindrical particles parallel to the crack tip, essentially in 2D, with identical properties to the matrix. (The constrained strain, and strain of the equivalent particle, can be related by the Eshelby tensor S_{ijkl}, which only depends on geometry). It is these matrix forces constraining the particle that will influence the crack tip stress intensity.

The effect of these forces on the crack tip stress intensity factor can be calculated using the weight function methods of Bueckner [127] as expanded by Paris et al [128]. The idea behind these weight functions is that if the stress intensity factor induced at the crack tip for an arbitrary loading is known for a particular crack geometry, this can be used to calculate the stress intensity for any other loading with the same geometry. Essential to this is the weight function **h**, which acts as a Green function for the system and is often calculated numerically for a reference loading. Knowing this weight function, an integral of the applied stress multiplied by the weight function along a line in the plane will give the crack tip stress intensity, via:

$$\int_{ST} \mathbf{ThdS} \tag{2.5}$$

52

where T represent the tractions in question and S_T is a line in the plane. For a Mode I crack, for example, with coordinates r and θ defined as distance from the crack tip and angle with respect to the crack plane respectively, this weight function is given as:

$$\mathbf{h_I} = \begin{pmatrix} h_x \\ h_y \end{pmatrix} = \frac{\mathbf{1}}{\mathbf{2\sqrt{2\pi}\sqrt{r}(1-\nu)}} \begin{pmatrix} \cos\left(\frac{\theta}{2}\right)[2\nu - 1 + \sin\frac{\theta}{2}\sin\frac{3\theta}{2}] \\ \sin\left(\frac{\theta}{2}\right)[2 - 2\nu - \cos\frac{\theta}{2}\cos\frac{3\theta}{2}] \end{pmatrix} \tag{2.6}$$

McMeeking and Evans consider this case of a Mode I crack and consider the transformation zone as one large transforming particle (averaging the effects over the zone via a transforming volume fraction). They neglect shape change effects for simplicity (and due to the tendency for self-accommodation of martensite variants reducing its impact in any case). Adapting the method to integrate around the boundaries of this transformation zone (determined via the earlier energetic work of Evans and Heuer [124]), they calculate the change in crack tip stress intensity factor induced by transformation.

Performing this calculation for the initial transformation zone produces a result of no change in the stress intensity factor. As such, the model then considers crack advance into the material, leaving a transformed wake behind. Integrating over the crack tip region, the sides of the transformed wake and the crack edges, R-curve behaviour is identified - change in stress intensity factor rising rapidly on initial crack advance then settling down to a steady value by the time crack length reaches circa 5 times the crack width. In any case a toughening effect of transformation can clearly be seen.

The asymptotic value of the modification to crack tip stress intensity factor is given as:

$$\frac{\Delta K_I}{Ee^T V_f \sqrt{w}} = -\frac{0.22}{1 - \nu} \tag{2.7}$$

where e^T is the volume component of transformation strain, E is Young's modulus, V_f is the volume fraction of particles and ν is Poisson's ratio.

Approaches since this work have considered in more detail such factors as reversal of transformation behind the crack tip leading to a partial wake, but in general the approach has stood the test of time. Many of the features predicted by the model, such as the aforementioned (partially transformed) wakes, significant ahead of crack tip transformation and toughening varying with the

53

square root of the zone height have been observed experimentally. [119] [129] [130] Budiansky et al [131] extend the work to other geometries and consider a finite element method for determining zone size.

Budiansky et al [131] also carry out one of the first energetic approaches to quantifying transformation toughening. They consider an energy balance equation, with energy released from cracking relieving stress remote from the crack going either into the wake, or being released at the tip. An expression for the energy left in transformed material in the wake is calculated, given knowledge of the distribution of residual dilatation. Results for supercritically transforming materials (those undergoing full and irreversible transformation on reaching a critical stress) can be calculated analytically and agree with McMeeking-Evans (at least once steady state toughening is reached [132]). For subcritically transforming materials a finite element approach is used, and also proved to be in reasonable agreement with the linear elastic method.

It should be noted that these approaches tend to focus on the volume strain of transformation as driving the toughening effect. This is due to the shear strain's tendency to self-accommodate via alternately oriented variants forming - but also reflects the orientation dependence making exact calculations difficult. Nonetheless, while it may not itself drive the toughening effect, the shape strain may be very important for nucleation of martensites and hence initiation of transformation - one variant must, after all, form before the oppositely orientated variant can nucleate to cancel its shape strain effect, and the formation of this initial variant may have a significant controlling influence on the shape and extent of the transformation zone. [133] [119] Shape strain is hence still relevant to transformation toughening, despite volume strain driving the actual stress intensity factor modification. Indeed, in systems with both volume and shape strains present and of comparable magnitude, considering the shear strain can change the transformation zone width by a factor of 4 [132] and have a similar associated effect on toughening. The transformation zone shape can also change significantly - leading to a higher proportion of transformed material falling in the region that contributes to toughening, rather than the region ahead of the crack tip where transformation in fact heightens stress intensity factors.
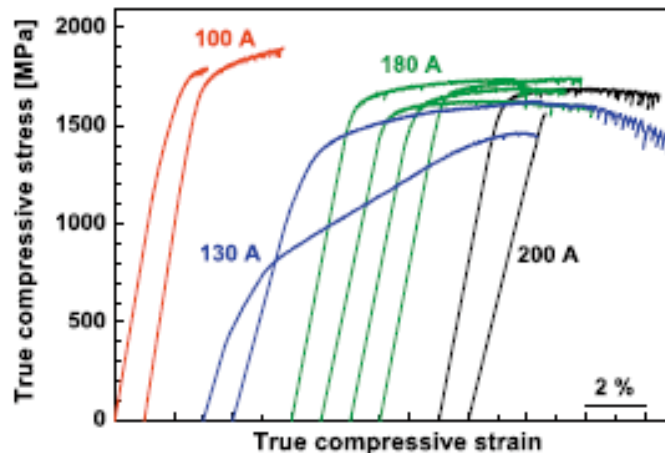
Figure 2.18: Sample stress-strain curves for CuZrAl metallic glasses cast with different melting currents. Note the pronounced plastic strain and some degree of work-hardening. From Eckert et al [136]

2.5.3 Composites

Transformation-toughened composites are commonly used - multi-phase TRIP-assisted steels being the classic example [118] albeit work by Bhadesia suggests that this may be less to do with transformation toughening than was first thought [134]. Zirconia-reinforced alumina is another example. [119]

Transformation toughening in metallic glasses was identified by the research group of Jurgen Eckert at IFW Dresden [1]. Eckert's group, working in the CuZrAl system, demonstrated significant compressive plasticity accompanied by strain hardening in in-situ glass-matrix composites. This was initially explained via the crystalline phase - CuZr B2 austenite, or at higher cooling rates austenite-like clusters - undergoing a stress-induced phase transformation to the martensite B19' and its superstructure. This would hence influence the stress state at nearby STZ, reducing accumulation of free volume and leading to ductility. Sample compressive stress-strain curves are shown in Figure 2.18. Eckert's group also observed some limited ductility and work hardening in tension, which is unusual in metallic glasses [135].

This strain hardening behaviour is unusual and notable in metallic glass systems. While it can also be observed in a very few dendritic systems where the crystalline phase work-hardens,

in general even plastically deformable metallic glasses will display constant or falling strain after yield. This evidently is of little use in practice, since once yield begins it is likely to continue, given the same applied stress. Strain hardening is, therefore, extremely exciting and desirable behaviour.

Eckert's initial work showed $Cu_{47.5}Zr_{47.5}Al_5$ alloys containing small crystals (5-10 nm) of the austenitic CuZr B2 phase. These crystals are too small for dislocation-based work-hardening mechanisms, seeming to rule out that means of toughening. Shear bands were seen to propagate wavily, thickening as they propagated. This was attributed to inhomogeneous distribution of the particles preferentially reducing STZ action and free volume accumulation in certain regions, causing changes in shear band direction. [1]

High energy x-ray diffraction data from these alloys at various stages of plastic deformation showed a much increased scattering intensity corresponding to martensite in heavily deformed samples [137]. This provides clear evidence for transformation occurring during deformation. Wu et al [138] have carried out experiments with similar crystal morphologies of non-transforming phases and shown an absence of strain-hardening effects, suggesting that the transformation is indeed responsible for this exceptional behaviour.

A further work in Nature Materials [139] expanded on the proposed mechanism. Taking a CuZrAl bulk metallic glass in tension, nanocrystals of B2 CuZr were observed to form on deformation. These nanocrystals then underwent significant twinning. Work-hardening and ductility were observed in the mechanical behaviour of the alloy. A number of co-related mechanisms were proposed to explain this complex behaviour. As explained in Sections 2.3.3 and 2.3.1, deformation in metallic glasses can be understood to be the mechanical overcoming of the energy barriers separating local minima in the energy landscape. Essentially, mechanical energy takes the place of the thermal energy that would cause rearrangements at higher temperatures. What Pauly et al proposed was that mechanical rearrangement could lead to crystallization, in the same manner as which heat treatment might - if the crystal was reasonably similar to the medium-range ordered state in the glass, and shared a similar composition.

Pauly et al explain this disordering in terms of a drop in local instantaneous shear modulus, but as discussed above this could be viewed in terms of any of the possible disorder parameters used to describe deformation in metallic glasses. The CuZr B2 phase shares a chemical composition
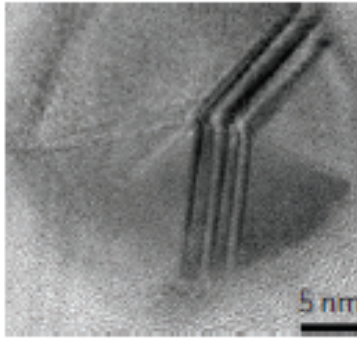
Figure 2.19: A twinned nanocrystal observed in deformed CuZr metallic glass.
From Pauly et al [139]

with the parent glass, despite only being metastable at room temperature. It also, remarkably, has very similar values of the elastic moduli G, E and K [140]. Therefore, it should form preferentially compared to the equilibrium phases $Cu_{10}Zr_7$ and $CuZr_2$. Formation of these nanocrystals is theorised to compete with shear band formation [139] or STZ activation [137]. The system would crystallize instead of STZ activation, hence reducing the number of STZ activating and impeding shear band formation. It is also suggested that crystallization can relax the local stress state, further reducing the propensity to form STZ and hence shear bands.

Once these crystals have formed, they undergo twinning - heavily twinned nanocrystals are observed in the post-deformation structure. This twinning work-hardens the crystals, enhancing ductility via counteracting the local softening effect of deformation-induced disorder. The volume change associated with twinning is furthermore suggested to impede the formation of shear bands and cracks, in a mechanism very reminiscent of traditional explanations for transformation toughening in ceramics and crystalline metals, further improving plasticity. Some of the overall toughening processes are shown in Figure 2.20.

A narrative that has developed more recently is the idea that transformation into the significantly harder martensite phase is the mechanism responsible for work-hardening in these systems [138] [140] [136], though this is typically applied to systems containing larger pre-existing crystals, on the scale of tens or even hundreds of microns. Eckert's group, working on a series of samples with varying crystal fraction, demonstrated two distinct regimes of behaviour. At low crystal volume
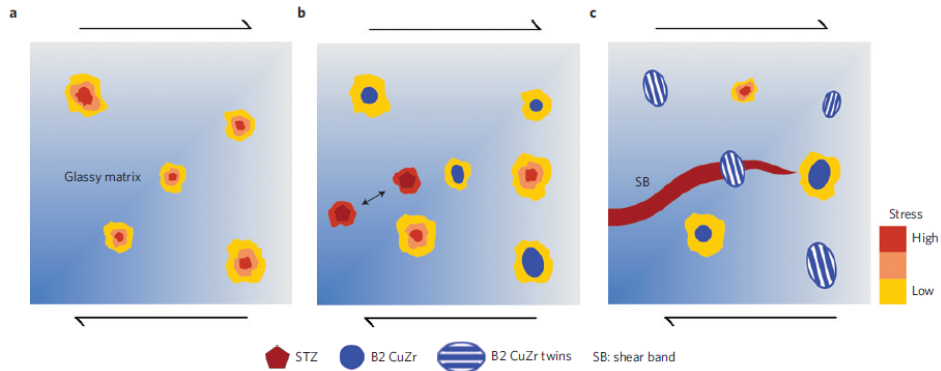
Figure 2.20: Representation of toughening mechanism in CuZrAl BMG. Under deformation, stress concentrations occur as seen in a). Some of these then form crystals, while others nucleate STZs, shown in b). c) shows these particles twinning to remove stress concentrations, while developing shear bands either avoid particles or their progress is blocked by them. From Eckert et al [139]

fractions, the yield of the system is dominated by the harder glassy matrix, and can be described by a rule of mixtures equation:

$$\sigma^c = f_\alpha \sigma^\alpha + f_\beta \sigma^\beta \tag{2.8}$$

where f_α and f_β are the volume fraction of the crystal and glassy phases respectively, and σ^c, σ^α and σ^β refer to yield strengths (combined, crystal and glass respectively). As crystal volume fraction increases, crystals eventually hit a percolation threshold and begin to connect into a network. Above this threshold, a load-bearing model is more appropriate:

$$\sigma^c = \sigma^\alpha (1 + 0.5 f_\beta) \tag{2.9}$$

Fracture strain is fitted empirically via a model that considers the system as made up of three regions - glass, crystal and interface. A clear fit for the data is possible - Pauly et al's plots of yield strength and fracture strain against crystal volume fraction are shown in Figure 2.21. Work hardening in the B2 phase is extreme, with yield circa 500 MPa and eventual failure around 2100 MPa. It is therefore suggested that this plastic deformation and work-hardening via martensitic transformation and twinning in the crystalline phase is a driving force for work-hardening and ductility in
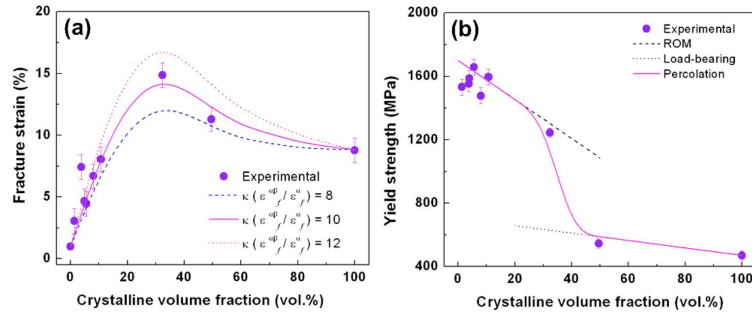
Figure 2.21: a) Yield Strength, and b) Fracture Strain, plotted against crystal volume fraction for CuZrAl bulk metallic glass composites. Both experimental data and theoretical predictions are shown to display reasonable agreement. From Pauly et al [140]

the composites as a whole.

The distinction should clearly be drawn between systems that are primarily glassy and work-harden due to nanocrystal formation in and around shear bands [139] and those with significant pre-existing crystal volume fractions [140] [136] [141] that work-harden due to the deformation and martensitic transformation of the crystal phase via strain partitioning.

The idea that transformation or twinning in nanocrystals is associated with a volume change or influence on the stress state at nearby shear bands continues to appear in discussion of these systems [139] [142] [143]. Schryvers et al [144] conducted a study of the CuZr martensite by transmission electron microscopy. The B2 austenite phase is body-centred cubic with a CsCl structure and lattice parameter a=0.3262 nm. The martensite is split between the monoclinic B19' base martensite and a superstructure. The base martensite has lattice parameters a_m=0.3278 nm, b_m=0.4161 nm, c_m=0.5245 nm, $\beta_m = 103.88\,°$. The superstructure has lattice parameters a_m=0.6316 nm, b_m=0.8562 nm, c_m=0.5331 nm, $\beta_m = 105.27\,°$. The volume change associated with the basic martensite is 0.05%, and for the superstructure 0.155%. Using experimental volume fractions an overall volume change can be estimated at 0.137%. This volume change is very small, which raises the question as to whether the volume change during transformation can in fact be influencing the deformation behaviour in CuZr metallic glasses. This question remains open to quantitative investigation.

2.6 Granular Materials

Comparisons between metallic glasses and granular materials have been drawn in numerous places throughout the metallic glass literature [62] [145] [146] [147]. Various groups have applied failure models from granular materials to metallic glasses. The Drucker-Prager [76] and Mohr-Coulomb [148] [73] [74] yield criteria have received wide acceptance in metallic glass circles.

A further connection between granular materials and metallic glasses can be demonstrated by considering the suggestion of Zhang and Greer [48] that shear band widths in metallic glasses and granular materials may operate on similar principles. Gourlay and Dahle [2] observed that shear bands are also found during solidification of crystalline metallic alloys. They extend the commonly understood relation that shear band widths fall typically between 7 and 18 particle diameters in granular materials [2] [149]. They plotted data from granular materials and solidifying metal alloys and showed that the trend extends to these materials, hence suggesting that these are dilatant shear bands.

Taking particle diameter as either the solvent-solvent bond length [150] or the cluster size (estimated here as three times that value), and taking shear band size data from the metallic glass literature [48] it is possible to extend this work to metallic glasses. Figure 2.22 clearly shows that metallic glasses fall within the same dilatant regime where clusters, as opposed to individual atoms, are used to determine particle diameter.

It is therefore clear that granular materials models may have some applicability to behaviour in metallic glasses - indeed the reverse has already been applied by Falk et al [146] who apply an STZ-based model to granular flow and confirm its applicability experimentally. The granular materials literature will hence be investigated in further detail.

Granular materials are commonly understood to cover such materials as sands, soils, powders, gravels, grain, and some varieties of rock. Typically they are aggregates of reasonably rigid particles, and have little or no cohesion to hold them together [151] (a notable difference from metallic glasses).

A key concept in deformation of granular media is that of Reynolds dilatancy [152]. Originally Reynolds observed the behaviour of beach sand drying up when compressed and explained this via
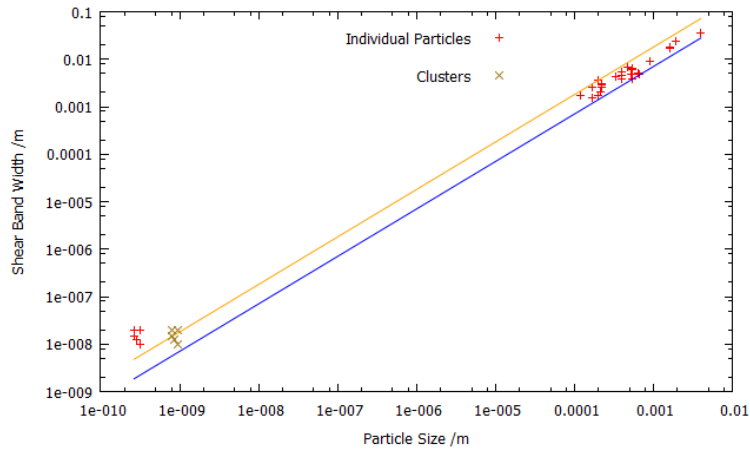
Figure 2.22: Extension of Gourlay: Shear Band Width vs Particle Size. Lines represent shear band widths of 7 and 18 particle diameters respectively. Note at the bottom left that the points for metallic glasses do not initially fit the model; however if clusters are used as the structural unit the data now fits the established trend.

lever action increasing the volume of the material by opening up voids and allowing water to drain into them [3]. This concept of dilatancy under stress has remained at the core of the science of granular media ever since.

There exists experimental evidence throughout the literature for the presence of shear bands in granular media. [153] [154] [155] Important to realise when comparing experimental treatment of granular media and metallic glasses is that the granular materials do not display cohesion - as such deformation geometries tend to be defined by their constraint and the manner in which deformation is driven. Experiments consider such situations as Couette flow (between two plates one of which is moving, often rotating) [156], triaxial deformation via compression of a column contained with rubber membranes [157], rotation of a bottom disc in a cylindrical container [158] and many similarly varied examples. By contrast, glasses tend to be experimentally deformed in standalone bulk samples - the most common geometry seen in the literature being uniaxial compression of a cylindrical sample of aspect ratio circa 2:1 [11] [159] [160] [161].

Theoretical models of shear banding in granular media have followed a number of approaches.
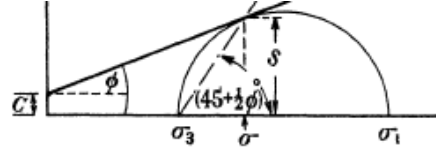
Figure 2.23: Mohr-Coulomb yield criterion. From Rowe [157]

Some of the earliest work in the field led to Mohr-Coulomb theory. Mohr-Coulomb essentially suggests that yield is pressure dependent, with normal pressure on a plane having an impact on yield. The Coulomb yield criterion can be expressed as:

$$\tau_y = \tau_0 \pm \sigma_n \tan \phi \tag{2.10}$$

where τ_0 is the component of strength independent of normal pressure, σ_n is normal stress on the shear plane, and ϕ relates to internal friction and is known as the angle of friction, or angle of shearing resistance.

Mohr-Coulomb theory combines this approach with the Mohr's Circle construction (typically used to resolve principal stresses). The idea is that Mohr's circle should just touch the yield surface as defined by Equation 2.10 at failure, and this can be used to determine the yield stress as shown in Figure 2.23.

Worth noting are the conditions typically considered when discussing dilatancy in granular media. Typical is a triaxial stress state, where $\sigma_1 > \sigma_2 = \sigma_3$ and resistance to shear is isotropic. These stresses σ_2 and σ_3 are needed to keep a cohesionless granular assembly in shape under compression; in a metallic glass the interatomic bonding plays an equivalent role. For this triaxial stress state, and from Mohr's circle as shown in Figure 2.23, Mohr-Coulomb yield occurs where:

$$\sigma_1 = \sigma_3 (\tan \frac{\pi}{4} + \frac{1}{2}\phi)^2 + 2c \tan \frac{\pi}{4} + \frac{1}{2}\phi \tag{2.11}$$

A large volume of work developed from Mohr-Coulomb theory. One of the most important approaches was provided by Rowe [157]. Rowe, citing Terghazi [162] criticized the existing models of the time for failing to take account of the fact that granular materials are made up of individual particles, instead concentrating too heavily on the assembly scale and treating sand as a homogeneous material. Mohr-Coulomb essentially treats yield as two cohesive and monolithic regions
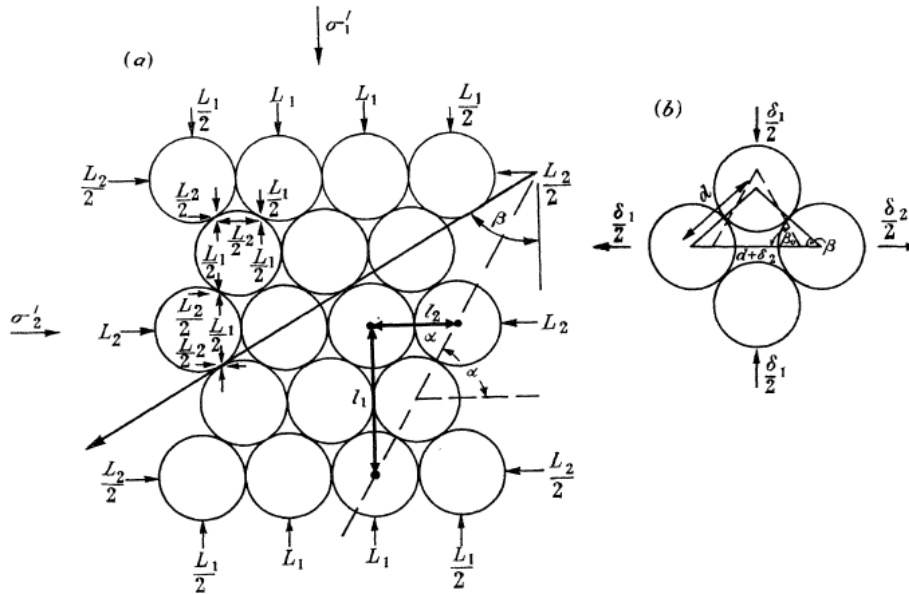
Figure 2.24: Schematic showing an example structure consisting of cylindrical rods. Note the planes defined by α and β in a) - the β-plane being that of maximum stress but not the easiest direction of failure in the structure, which is given by the α-plane. b) shows the kinematics of deformation from which we obtain a ratio of strain rates. From Rowe [157]

sliding across each other on a single friction-controlled band, and pays no direct attention to the influence of particle arrangement and behaviour in the sliding region.

Rowe's analysis considers geometric arrangements of particle packing and notes that the direction of global sliding (the 'β-plane' and the planes defined by the local packing along which local sliding will likely occur (the 'α-plane') are not necessarily coincident - as shown in Figure 2.24 for an example structure.

Rowe realised that it was possible to obtain analytically an expression for the rate of work done against the major and minor principal stresses. He theorized that values above unity for the ratio of these work rates corresponded to energy losses due to frictional heating, and that minimising this energy rate ratio $\dot{E}$ with respect to global angle of sliding β would therefore give the most efficient mode of failure. To find this ratio analytically, he first considered the static equilibrium of the system. Resolving forces on the slip plane (taking into account the friction resultant and

$$\frac{P - c_\mu x}{Q + c_\mu x \tan \beta} = \tan(\phi_\mu + \beta)$$

$$P = Q \tan(\phi_\mu + \beta) + \frac{c_\mu x \sec^2 \beta}{1 - \tan \phi_\mu \tan \beta}$$
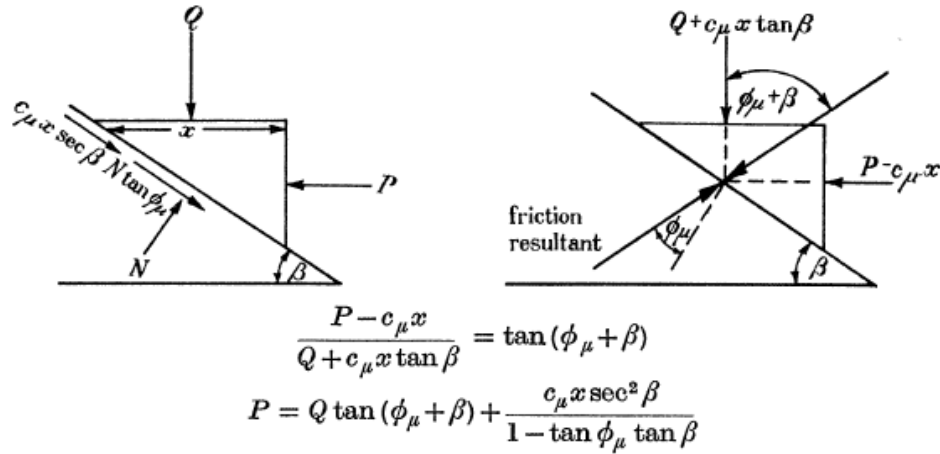
Figure 2.25: Resolution of forces on a slip plane inclined at β to applied shear force P. Q is force normal to P, then note also cohesion and frictional terms (the cohesion term is later neglected). From Rowe [157]

angle thereof - see Figure 2.25 for an example), and disregarding the cohesion term (valid for many granular systems), led to an expression for the ratio of effective principal stresses σ'_1/σ'_2. Considering the structure and hence kinematics of the system would then allow him to obtain an expression for strain rates $\dot{\epsilon}_2/\dot{\epsilon}_1$, via considering a typical mode of deformation for that structure. Figure 2.24 shows this deformation mode for an example structure.

Rowe performed these calculations for a range of sample structures, and for all cases obtained the same expression for the energy rate ratio:

$$\dot{E} = \frac{\sigma'_1 \dot{\epsilon}_1}{\sigma'_2 \dot{\epsilon}_2} = \frac{\tan \beta + \phi_\mu}{\tan \beta} \tag{2.12}$$

The angle β is defined with respect to the major principal stress and ϕ_μ is the true angle of friction. Minimisation suggests that sliding will tend to occur on the β-plane defined by $\beta = (\pi/4 - (1/2)\phi_\mu)$, seemingly independent of packing geometry. This leads to a stress-dilatancy relation:

$$-\frac{\sigma_1 \dot{\epsilon}_1}{\sigma_2 \dot{\epsilon}_2} = \left(\tan \frac{\pi}{4} + \frac{\phi_\mu}{2} \right)^2 \tag{2.13}$$

The ratio of effective principal stresses (σ'_2 being due to elastic support) at and beyond peak

strength can be expressed as:

$$\frac{\sigma_1'}{\sigma_2'} = \tan\alpha\tan\phi_\mu + \beta \qquad (2.14)$$

where α is the angle defined by the α-plane with respect to the minor principal stress, and hence carries information about packing geometry. Rowe suggests yield occurs when this effective stress ratio reaches unity and internal pressure can no longer be contained. Note that in metallic glasses, which have a significant cohesion term, this might no longer be true.

Guo and Wan [163] later criticize Rowe's approach for losing key information concerning the fabric (the local structure). Rowe's expressions for energy rate ratio and stress dilatancy lose any effect of actual particle arrangements, being reliant only on the friction angle and angle of global sliding. They then further criticize Rowe's approach for suggesting that dilatancy rate depends only upon the applied stress ratio, which is disproven by experiment.

Gou and Wan then note that Rowe's expressions for σ_1/σ_2 and $\dot{\epsilon}_2/\dot{\epsilon}_1$ contain a common factor, and that stress-dilatancy relations could instead be obtained by combining these expressions so as to not lose structural information. This leads to stress-dilatancy relations of the form $\frac{\sigma_1}{\sigma_2} = G_a\frac{\dot{\epsilon}_2}{\dot{\epsilon}_1}$ where G_a is a geometrical factor related to local structure.

They consider a random packing assembly and develop an extremely complex expression for the stress-dilatancy behaviour via a micromechanical approach. This can be simplified, where it then takes a very similar form to Rowe:

$$-\frac{\sigma_1\dot{\epsilon}_1}{\sigma_2\dot{\epsilon}_2} = \frac{\tan\bar{\beta} + \phi_f}{\tan\bar{\beta}} \qquad (2.15)$$

where $\bar{\beta}$ is the mean sliding angle. If simplified as the mean of the maximum and minimum values thereof, it can be approximated as $\pi/4 - \phi_\mu/2$. ϕ_f is the 'nominal friction angle' and depends on the fabric and its deformation state. Guo and Wan's adaptation of Rowe's stress-dilatancy relations hence now contains information about the physical nature of the particle arrangement.

A useful measure of dilatant behaviour that appears throughout is the dilatancy angle ψ, defined as:

$$\sin\psi = -\frac{\dot{\epsilon}}{\dot{\gamma}} = \frac{\dot{\epsilon}_1 + \dot{\epsilon}_2}{\dot{\epsilon}_1 - \dot{\epsilon}_2} \qquad (2.16)$$

What is key to draw out of Guo and Wan [163] and Rowe [157] is the importance of the fabric. Both approaches centre around developing a model for a structure and using the constraints that structure imposes on deformation to provide information on stress-dilatancy and the energetics of yield. The work of Guo and Wan is therefore further built upon by Tordesillas et al [3] who consider an approach based around collective buckling of force chains.

Force chains have long been identified as load bearing structures in granular media. The basic framework is that on loading, particles arrange themselves into a structure whereby dense chains of particles parallel to the major principal stress carry the majority of the load, and build up elastic strain energy. These chains are then supported laterally by loose networks of less organised particles, not all of which need be in direct contact with the chain. Beyond a certain point, the force chains are unable to support the load and begin to buckle, somewhat breaking down the force chain structure, releasing some of their stored energy into the structure and enabling yield. These buckling events concentrate into shear bands and can carry an associated dilatation via the opening up of gaps between collectively buckling force chains.

Force chains have been observed experimentally - Sanfratello and co-workers [164] carried out experiments with a two-dimensional array of photoelastic discs under compression. Figure 2.26 shows a clear force chain network supporting the load, as the discs under load glow distinctively. Sanfratello further goes on to determine distributions of force chain lengths from the experiment, as shown in Figure 2.27. Short force chains are the most common, with incidence decaying exponentially until reaching a steady-state value of incidence for chains longer than circa ten particles.

This idea of load support via a network of load-bearing regions supported by an elastic matrix has been theorised to also exist in metallic glasses. Ye et al [165], for example, describe metallic glasses as composed of liquid-like free-volume zones surrounded by a hard elastic shell of atoms. Ma and co-workers [166] further mention fractal networks of clusters in metallic glasses. Burnley et al [167] extend the concept of force chains to polycrystalline rocks, which provides significant support for their applicability in systems with structural cohesion. Cao et al [60], working with MD simulations, observe a 'backbone' of fully coordinated clusters supported by an elastic matrix that needs to be disrupted in the shear band plane to allow large shear strains to occur - a clear analogue to force chain buckling. Liss et al [168] even provide supporting experimental evidence. Their
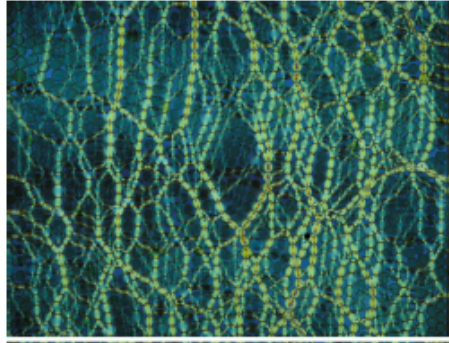
Figure 2.26: Force chains visible in a compressed network of photoelastic discs. From Sanfratello et al [164].
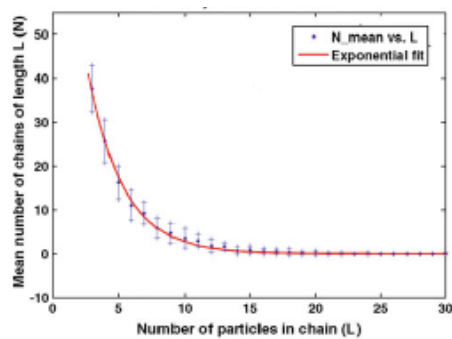
Figure 2.27: Distribution of force chain lengths in photoelastic disc experiment. There exist many more short chains, but after circa 10 particles in length force chains occur in approximately equal frequency regardless of size. From Sanfratello et al [164].
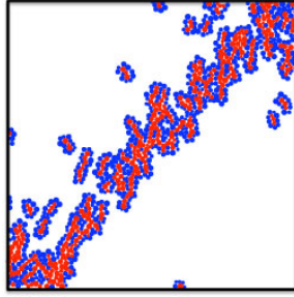
Figure 2.28: Spatial distribution of confined buckled force chains in DEM model of a granular material, showing a clear shear band pattern. From Tordesillas et al [3].

work used in-situ high-energy X-ray diffraction to examine how a Zr-based metallic glass behaved under compression. During deformation, beyond a certain point, the axial compression continues but is then accompanied by additional creation of free volume between the clusters. Notably, this free volume all appears in the transverse direction, drawing the direct parallel with force chain buckling. Notably, nearest-neighbour interactions are not significantly changed, suggesting that the cluster, rather than the atom, is the granular particle analogue and structural unit.

Tordesillas et al [3] develop their force chain model in two stages. The first is a discrete element model (DEM), and the results of this are then used to inform the development and intepretation of their micromechanical model. An algorithm is applied to the outputs of the DEM to identify particles in force chains. These are determined via identifying groups of particles with loads aligned in a narrow angular range and of above average magnitude. A second algorithm then identifies the buckled force chain segments. Combined with their confining neighbours, the collective assembly is denoted a 'confined buckled force chain' (CBFC).

The population of CBFCs is shown to correlate with overall dilatation of the system. These CBFCs also organise themselves into spacial regions that are indicative of shear banding - see Figure 2.28. Of particular interest from a metallic glass perspective are the example CBFCs shown in Figure 2.29 - these are extremely reminiscent of the schematics of shear transformation zones (STZ) shown in Figure 2.11.

Tordesillas et al then move on to develop a directly analytical model for collective force chain
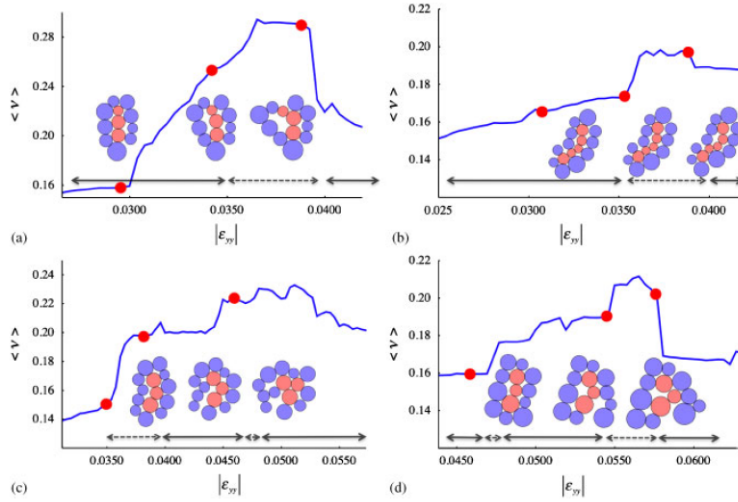
Figure 2.29: Schematics of confined buckled force chains (CBFC). Note the similarity to typical visualizations of STZ. Here $< \nu >$ is average porosity and ϵ_{yy} is applied strain. From Tordesillas et al [3].

buckling [3] [169] [4]. Their approach is motivated by much the same concern as Guo and Wan - to develop a stress-dilatancy relation rooted in the physical behaviour of the system that carries information related to local properties and behaviour.

Their detailed approach will be covered elsewhere in this document, however a brief overview will be presented here. Several assumptions are made to simplify the system - the model operates in two dimensions with arrays of perfectly aligned parallel force chains bearing load. Defects and imperfections are not considered - in real systems these irregularities would provide favoured sites for buckling. Only elastic buckling is considered - plastic failure of particles or of the support matrix are not taken into account.

Force chains are treated as a series of hard-sphere particles connected by springs. Spring constants k_n, k_r, k_t and k_s relate to axial compression, particle rotation, interparticle sliding and lateral network support respectively. A potential energy equation is formulated, simplified and eventually solved to determine the conditions required for failure of a single force chain. While buckling modes might initially be considered to be sinusoidal fluctuations of the entire force chain, it is shown that in many cases one sub-segment of the chain buckling is mathematically equivalent -
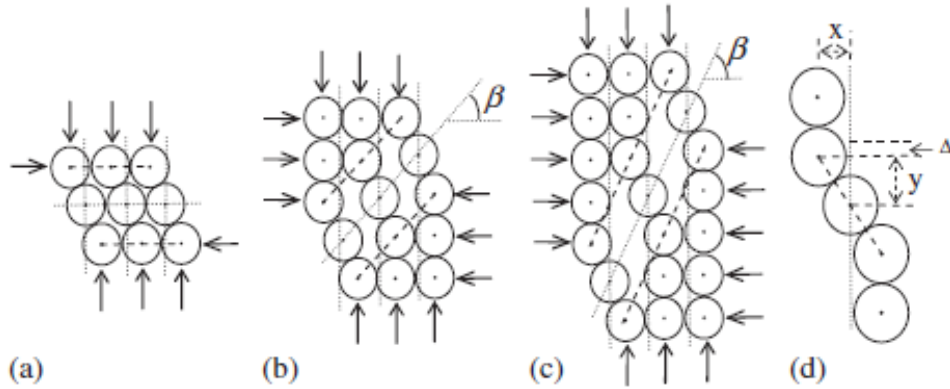
Figure 2.30: Three force chains buckling alongside one another, showing how dilatancy occurs as gaps open up between the chains. a) through b) show variation in shear band angle β, d) shows a single force chain buckling. From Tordesillas et al [3].

hence introducing the concept of buckling segment length K.

Collective failure is then discussed. A simplified system is first approached, with three parallel force chains each buckling in segments containing three particles. Figure 2.30 shows how voids can open up between force chains that buckle at different places. Several buckling segments operating together are identified as a shear band, and the angle described by a line linking the three centres, with respect to the undeformed chain axis, is described as the shear band angle β.

By considering the static equilibrium of the system in the same manner as Rowe, an expression relating ratio of stresses σ_1/σ_2 is identified. Similarly a consideration of the failure kinematics of collective buckling segments gives an expression for $\dot{\epsilon}_2/\dot{\epsilon}_1$. Combined, these could be used to create an expression for $\dot{E}$ that could then be minimised as in Rowe's approach, however this would lose information related to the fabric, and suggests failure where all buckling segments fall in a horizontal line at $\beta = 0$.

Instead a common factor in σ_1/σ_2 and $\dot{\epsilon}_2/\dot{\epsilon}_1$ is identified, and used to form a stress-dilatancy relation:

$$\dot{\epsilon}_2/\dot{\epsilon}_1 = -G(\beta)\frac{\sigma_1}{\sigma_2} \tag{2.17}$$

where $G(\beta)$ is $\frac{2(2\tan\beta+3)}{2\tan\beta+1}$. This bears significant similarity to Rowe's theories.

Having considered this simplified system, Tordesillas et al then extend the work to consider a more generalised assembly of M force chains each buckling with segments of length K. They once again consider the static equilibrium of the system to obtain expressions for a ratio of stresses, and the kinematic constraints of buckling to obtain a ratio of strain rates. These can be used via a common factor to obtain a stress-dilatancy relation of the form:

$$\dot{\epsilon}_2/\dot{\epsilon}_1 = -G_g \frac{\sigma_1}{\sigma_2} \tag{2.18}$$

G_g here contains significant information about the physical nature of the system. It encapsulates information concerning the buckling force and mode, the stress state, shear band angle and size, particle radius, and via these other quantities the elastic spring constants and hence local physical properties of the fabric.

They present a few example graphs showing behaviour of selected model outputs with varying inputs. The dilatancy parameter $\sin\psi$ for example is presented against vertical strain for varied shear band width K and shear band angle β reproduced here in Figure 2.32 - showing increased dilatancy with increased K and also as shear band angle moves away from $\beta = \pi/2$. Variations in $\sin\phi$ with number of parallel chains ('cluster size) M, K with spring constants, $\sin\phi$ with K, β and M, and so on are also shown as examples, though very few conclusions are drawn as regards the meanings and physical implications of this data.

A companion work by the same group [169] considers the effect of varying chain length, and shows that for very short force chains, critical buckling load decreases rapidly with increasing chain length. Beyond this point, critical load oscillates about a steady-state value with fluctuations of rapidly decreasing amplitude, and with a critical length scale set by a ratio of the buckling mode and force chain length. These fluctuations are of small enough amplitude that it is suggested force chains above circa eight particles in length can be said to have essentially the same buckling load as those eight particles long.

This detailed model of local deformation and nascent shear banding by collective force chain buckling, while based around a number of significant assumptions, nonetheless carries the power to provide significant information on the shear banding and yield behaviour of granular materials

(a) N+2

Figure 2.31: Minimum buckling force F_{min} vs force chain length $N+2$ for two sets of boundary conditions C1, C2. Note the rapidly decreasing amplitude of oscillations. From Tordesillas et al [169].

(a)

(b)

Figure 2.32: Example plot of volumetric vs vertical strain for varying shear band width K and shear band angle β calculated using force chain buckling model. Clear dilatancy can be observed post buckling. From Tordesillas et al [3].

by varying its inputs. Perhaps, by extension and with more attention paid to the implications of the data, its predictions could be applied to the field of metallic glasses as well.

Chapter 3

Quantifying Transformation Toughening in Metallic Glasses

3.1 Introduction

As established in Section 2.5.3, the volume change during the transformation from the austenite to martensite phases in copper-zirconium alloys is very small. This calls into question a commonly asserted explanation for the work-hardening and ductility observed in Cu-Zr-Al metallic glass matrix composites, as exemplified by the work of Pauly et al [1].

Mathematics developed to describe transformation toughening in transformation-stabilized zirconia [123] will here be adapted to consider the outstanding issue: can this transformation actually have a significant impact on the stress state at the shear band?

The methods used will follow very closely those of McMeeking and Evans [123], and Evans and Heuer [124], and as such those bodies of work can be referred to alongside this analysis to provide further insight.
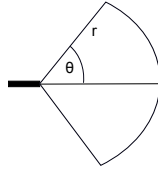
Figure 3.1: Plane perpendicular to crack front, showing the crack extending behind the front, and defining distance r and angle θ with respect to the advancing crack.

3.2 Determining the Transformation Zone

The first step in the analysis is to find the size and shape of the transforming region around the crack (or in this case shear band) tip. The method of Evans and Heuer [124] is used. A fundamental assumption will be made: that a shear band can be modelled as a Mode II crack, and that stress states around the two will be similar. This parallel does exist elsewhere in the metallic glass literature [170] [171] [44] and hence would appear reasonable (the typical approach is to consider a shear band as a Mode II phenomenon that grows into a mixed Mode I and Mode II crack, finally failing when transitioning to pure Mode I).

A reference convention must first be established. The system is modelled in two dimensions. A crack front runs perpendicular to the plane considered. As shown in Figure 3.1, cylindrical polar coordinates are defined with respect to the advancing shear band such that r denotes distance from the band tip, and θ denotes angle made with the plane defined by the crack.

Transformation or otherwise of a particle is governed by the total free energy of the particle-matrix system. The change in chemical free energy of the particle with transformation, mismatch energies at the particle-matrix interface, and the strain energy of the system must be considered.

Chemical free energy can be found fairly simply. The chemical free energy change for transformation can be expressed as $-V_p \Delta G_0$ where G_0 represents the difference in chemical free energy per unit volume between the transformed and untransformed phases and V_p is the particle volume.

The difference in chemical free energy of transformation per mole can be found from work by Zhou et al [172] to be $(-1408.52 + 2.702\ T)\ \mathrm{J\,mol^{-1}}$. Taking the mass of one mole of CuZr, and the density of CuZr B2 (found from Li et al [173] to be circa $7.5\ \mathrm{g\,cm^{-3}}$) it is possible to obtain the

free energy of transformation per unit volume to be $(-1408.52 + 2.702\,T)/(2.135 \times 10^{-5})\,\mathrm{J\,m^{-3}}$.

Next, the strain energy of the system is considered from an Eshelby inclusion viewpoint [125] [126], as mentioned in Section 2.5.2. The basic approach is to consider a particle contained within an infinite matrix. The particle undergoes a transformation with strain corresponding to a strain of ϵ_{ij}^T were it not to be constrained. In order for the particle to fit back into the matrix, surface tractions must be applied to its surface to return it to its original shape, and these stresses are mirrored in the matrix. The stresses that develop in the particle are denoted σ_{ij}^I. The hydrostatic and deviatoric components thereof can be expressed as, via Eshelby [126]:

$$\sigma^I = 3B_p(\epsilon^c - \epsilon^T) = 3B_m(\epsilon^c - \epsilon^{T*}) \tag{3.1}$$

$$'\sigma_{ij}^I = 2G_p('\epsilon_{ij}^c - '\epsilon_{ij}^T) = 2G_m('\epsilon_{ij}^c - \epsilon_{ij}^{T*}) \tag{3.2}$$

where G and B denote shear and bulk modulus, subscript p and m refer to the particle and the matrix. The term ϵ^{T*} is a transformation strain belonging to the equivalent particle, which is a construct taken from Eshelby's work intended to account for elastic modulus mismatches. From Eshelby [125]:

$$\epsilon^c = \frac{\epsilon^{T*}}{3}\left(\frac{1 + \nu_m}{1 - \nu_m}\right) \tag{3.3}$$

$$'\epsilon_{ij}^c = \frac{2'\epsilon_{ij}^{T*}}{15}\left(\frac{4 - 5\nu_m}{1 - \nu_m}\right) \tag{3.4}$$

where ϵ^c and $'\epsilon_{ij}^c$ are the hydrostatic and deviatoric components of the constrained strain. Substituting in Equations 3.1 and 3.2 to eliminate ϵ^{T*}, and using relations between the elastic constants:

$$E = 3B(1 - 2\nu) = 2G(1 + \nu) \tag{3.5}$$

an expression for the stresses within the particle can be obtained.

$$\sigma^I = \frac{\epsilon^T}{\frac{1\nu m}{2E_m} + \frac{1 - 2\nu_p}{E_p}} \tag{3.6}$$

$$'\sigma_{ij}^I = \frac{'\epsilon_{ij}^T}{\frac{1 + \nu_p}{E_p} + \frac{2(1 + \nu_m)(4 - 5\nu_m)}{E_m(7 - 5\nu_m)}} \tag{3.7}$$

76

The strain energy of the system must take into account the impact of any applied stresses. ΔU denotes the increase in strain energy of the system. The strain energy of the particle-matrix system when not under applied stress can be expressed as:

$$\Delta U_T = V_p \epsilon_{ij}^T \sigma_{ij}^I / 2 \tag{3.8}$$

Applying a stress σ_{ij}^A modifies the above expression. The modification due to elastic modulus mismatch between particle and matrix is neglected, since transformations rarely lead to significant changes in elastic moduli. However, the applied stress field will have a different influence on the particle before and after transformation, and the term describing this is given by [125]:

$$\Delta U_I^T = -V_p \sigma_{ij}^A \epsilon_{ij}^T \tag{3.9}$$

Combining these terms leads to:

$$\Delta U = -V_p \epsilon_{ij}^T \left(\sigma_{ij}^A + \frac{1}{2} \sigma_{ij}^I \right) \tag{3.10}$$

Add in the chemical free energy term and this gives:

$$\Delta G = -V_p \Delta G_0 - V_p \epsilon_{ij}^T \left(\sigma_{ij}^A + \frac{1}{2} \sigma_{ij}^I \right) \tag{3.11}$$

Note that the term related to surface energy has been neglected - this is consistent with a thermoelastic martensite, such as are found in shape memory systems. Transformation will be favourable when the free energy change is negative, and this constraint leads to the critical condition:

$$\sigma_{ij}^A \epsilon_{ij}^T \geq -\frac{1}{2} \sigma_{ij}^I \epsilon_{ij}^T - \Delta G_0 \tag{3.12}$$

The components of the term σ_{ij}^I have already been derived and are given in Equations 3.6 and 3.7 above. The next step is to determine the stress field around the shear band tip. Evans and Heuer calculate this in Mode I, here Mode II expressions will be used instead. As found in Stephenson [174]:

$$
\left.\begin{array}{c} \sigma_{11} \\ \sigma_{12} \\ \sigma_{22} \end{array}\right\} = K_{II} r^{\frac{-1}{2}} \begin{cases} \sin\frac{\theta}{2}\left[-2 - \cos\frac{\theta}{2}\cos\frac{3\theta}{2}\right] + o\left(r^{(-1/2)}\right) \\ \cos\frac{\theta}{2}\left[1 - \sin\frac{\theta}{2}\sin\frac{3\theta}{2}\right] + o\left(r^{(-1/2)}\right) \\ \cos\frac{\theta}{2}\sin\frac{\theta}{2}\cos\frac{3\theta}{2} + o\left(r^{(-1/2)}\right) \end{cases} \tag{3.13}
$$

Here K_{II} is the applied stress intensity factor. It should be noted that this applies primarily close to the shear band tip, where r is much smaller than the band length.

The expression for the critical transformation condition given in Equation 3.12 is in terms of the chemical free energy (determined to be $-2.83 \times 10^7\,\mathrm{J\,m^{-3}}$ at T=298 K), the applied stresses near the shear band tip (found to be given by Equation 3.13), the transformation strain ϵ_{ij}^T and the stresses caused by transformation (given in Equations 3.6 and 3.7). Therefore, combining these expressions allows the transformation zone radius to be calculated, given a known transformation strain.

Firstly, take Equation 3.10 and separate out the terms to give:

$$
\Delta U/V_p = -[\epsilon^T(\sigma^A + \sigma^I/2) + {}'\epsilon_{ij}^T({}'\sigma_{ij}^A + \sigma_{ij}^I/2)] \tag{3.14}
$$

The hydrostatic component ΔU_h can be found by substituting in σ_I as found in Equation 3.6. Divide through by E_p and $\epsilon^T\epsilon^T$, multiply the relevant term by E_m/E_m and the following is obtained:

$$
\frac{\Delta U_h}{E_p V_p \epsilon^T \epsilon^T} = \frac{E_m/3}{E_p(1 + \nu_m) + 2E_m(1 - 2\nu_p)} - \frac{\sigma^A}{\epsilon^T E_p} \tag{3.15}
$$

The deviatoric component ΔU_d is found by a similar method. Substitute in Equation 3.7, divide both sides through by ${}'\epsilon_{ij}^T\,{}'\epsilon_{ij}^T$ and E_p, multiply the relevant term by E_m/E_m and then $(7-5\nu_m)/(7-5\nu_m)$, and the expression below emerges:

$$
\frac{\Delta U_d}{E_p V_p\,{}'\epsilon_{ij}^T\,{}'\epsilon_{ij}^T} = \frac{(7 - 5\nu_m)E_m}{2E_p(1 + \nu_m)(4 - 5\nu_m) + E_m(1 + \nu_p)(7 - 5\nu_m)} - \frac{{}'\sigma_{ij}\,{}'\epsilon_{ij}^T}{E_p\,{}'\epsilon_{kl}^T\,{}'\epsilon_{kl}^T} \tag{3.16}
$$

To clean up the expressions, $\beta_1 = E_m/E_p$ is defined. Bringing in the free energy term as per Equation 3.12, and using the subscript c to refer to critical values for transformation:

$$\sigma_c^A V + ('\sigma_{ij}^A)_c \,'\epsilon_{ij}^T = -\Delta G_0 + E_p \beta_1$$

$$\left[\frac{(1/3)(\epsilon^T)^2}{(1+\nu_m)+2\beta_1(1-2\nu_p)} + \frac{'\epsilon_{ij}^T \,'\epsilon_{ij}^T (7-5\nu_m)}{2(1+\nu_m)(4-5\nu_m)+\beta_1(1+\nu_p)(7-5\nu_m)} \right] \quad (3.17)$$

At this stage the applied stresses are introduced. This is the point where significant divergence from Evans and Heuer's method appears - since this analysis considers the Mode II case, the Mode II expressions from Equation 3.13 will be used. The volume term σ_c^A is taken as $(1/3)(1+\nu)(\sigma_{11}+\sigma_{22})$, and $'\sigma_{ij}^{Ac}$ as σ_{12}. Rearranging, an expression for the critical radius for transformation is found, hence defining the transformation zone:

$$\sqrt{r_c} = -\frac{K_{II}\left[\cos(\theta/2)(1-\sin(\theta/2)\sin(3\theta/2))\epsilon^S - 2(1+\nu)/3\sin(\theta/2)\epsilon^T\right]}{\Delta G_0 + \beta_1 E_p \left[\frac{(1/3)(\epsilon^T \epsilon^T)}{(1+\nu)+2\beta_1(1-2\nu_p)} + \frac{(7-5\nu)\epsilon^S \epsilon^S}{2(1+\nu_m(4-5\nu_m)+\beta_1(1+\nu_p)(7-5\nu_m)}\right]} \quad (3.18)$$

3.3 Effects of transformation on the shear band tip

Having identified the transformation radius, the time has now come to consider what effect this transformation has on the shear band tip. This segment now follows the principles set out in McMeeking and Evans' work of 1982 [123], though the details of the approach will differ.

The basic principle behind their work is that as the crack (shear band) advances, particles around it transform. The Eshelby surface tractions applied by the matrix to constrain the transformed particles have an impact on the stress state at the shear band tip. These tractions are given by $\mathbf{T} = -\mathbf{T_c} = \mathbf{n}\mathbf{C}\epsilon_{ij}^{\mathbf{T}}$, where $\mathbf{T_c}$ are the tractions applied to the particle surface, $\mathbf{T}$ represents the body forces restoring equilibrium, $\mathbf{n}$ is the normal to the particle surface in the outward direction, and $\mathbf{C}$ is the particle's elasticity matrix.

The influence of these tractions T can be quantified using the methods of Bueckner [127], Rice [175] and Paris [128], following the methods in McMeeking and Evans [123]. They define a weight function $\mathbf{h}$ such that:

$$\Delta K = \int_{ST} \mathbf{T}\mathbf{h}d\mathbf{S} \quad (3.19)$$

79

where ΔK is the change in stress intensity factor at the shear band tip due to the transformation, and can hence be regarded as a measure of toughening. The Mode I weight factor is used in McMeeking and Evans' work, the Mode II equivalent will be used here, as given by Paris [128]:

$$\mathbf{h_{II}} = \begin{pmatrix} h_x \\ h_y \end{pmatrix} = \frac{1}{2\sqrt{2\pi}\sqrt{\mathbf{r}}(1 - \nu)} \begin{pmatrix} \sin\left(\frac{\theta}{2}\right)[2 - 2\nu + \cos\frac{\theta}{2}\cos\frac{3\theta}{2}] \\ \cos\left(\frac{\theta}{2}\right)[1 - 2\nu + \sin\frac{\theta}{2}\sin\frac{3\theta}{2}] \end{pmatrix} \tag{3.20}$$

It should be noted that this only applies reasonably near the shear band tip, and hence the method assumes any transforming particles fall within this region of dominance. It is further assumed that the far-field effects of the sample edges are negligible. This approach only considers direct advance of the shear band; branching or activation of secondary bands are not considered.

Further following McMeeking and Evans' method, splitting the volume and shape terms and working with the entire transformation zone treated as a single transforming particle:

$$\Delta K_I = [E/(1+\nu)] \int_{Sp} [(\boldsymbol{n}\boldsymbol{\epsilon}^T\boldsymbol{h} + (\nu\boldsymbol{\epsilon}^T\boldsymbol{nh})/(1 - 2\nu))] \tag{3.21}$$

defining ϵ^T as the trace of $\boldsymbol{\epsilon^T}$. Here McMeeking and Evans simplify this expression for a case with only volume change involved. Given that in typical martensitic transformations correspondence variants self-accommodate (see section 2.5.1) to avoid shape change, this would seem to be a reasonable assumption - nonetheless after working through the dilation-only case, the shape change influence will be considered later in this work.

3.3.1 Volume Change Only

Simplifying Equation 3.21 for zero shape change, the expression for the stress intensity change at the shear band tip ΔK_{II} can be expressed as:

$$\Delta K_{II} = \frac{\epsilon^T E}{3(1 - 2\nu)} \int_{Sp} \mathbf{nhdS} \tag{3.22}$$

For the following calculations, an effective transformation strain $\epsilon^T_{eff} = \epsilon^T V_f$ is defined, where V_f is the volume fraction of particles within the transformation zone - essentially, the zone is being treated as one large particle.

The direction of the zone normal **n** can be found via:

$$\mathbf{n_{dir}} = \begin{pmatrix} n_x \\ n_y \end{pmatrix} = \begin{pmatrix} -r\,'\sin(\theta) - r\cos(\theta) \\ r\,'\cos(\theta) - r\sin(\theta) \end{pmatrix} \tag{3.23}$$

where $r\,'$ is the gradient of r with respect to θ, and the expression for r_c in Equation 3.18 is used for r. Note that the above expression will need to be normalised to obtain the unit normal vector. For cylindrical polar co-ordinates, the surface element can be found via:

$$dS = \sqrt{dr^2 + r^2 d\theta^2} \tag{3.24}$$

Hence:

$$\Delta K_{II\ tip} = \frac{\epsilon^T E}{3(1 - 2\nu)} \int_{lim1}^{lim2} \begin{pmatrix} -r_c'\sin(\theta) - r_c\cos(\theta) \\ r_c'\cos(\theta) - r_c\sin(\theta) \end{pmatrix} \cdot$$

$$\frac{1}{2\sqrt{2\pi}\sqrt{r_c}(1-\nu)} \begin{pmatrix} \sin\left(\frac{\theta}{2}\right)[2 - 2\nu + \cos\frac{\theta}{2}\cos\frac{3\theta}{2}] \\ \cos\left(\frac{\theta}{2}\right)[1 - 2\nu + \sin\frac{\theta}{2}\sin\frac{3\theta}{2}] \end{pmatrix} \sqrt{dr_c^2 + r_c^2 d\theta^2} \tag{3.25}$$

Transformation strain here is taken to be the volume component only - from Schryvers [144], the volume change in the CuZr austenite to martensite transformation is 0.137%, and volume fraction of particles estimated at 0.1, giving the trace of the hydrostatic strain matrix as $\epsilon_V^T = 0.000137$.

The elements of Equation 3.22 are hence all in place. This will first be calculated for the initial transformation zone around the shear band prior to advance, and then the zone around an advancing shear band will be considered. Physical properties for the $Cu_{47.5}Zr_{47.5}Al_5$ system will be used as sourced from the work of Pauly [136], Zhou [172] and Schryvers [144] and reproduced in Table 3.1.

For the purposes of these calculations, a sample initial stress intensity factor of 5 MPa m$^{1/2}$ is used, corresponding to an otherwise brittle glass. Room temperature of 298 K is further assumed. The full integral is not shown in the body of this text due to its lengthy nature. Calculations are carried out using Wolfram Mathematica 8.0, and sample code is shown in Appendix A.

To calculate for the zone prior to shear band advance, Equation 3.25 should be integrated from $-\pi$ to π. As expected from the parallels with McMeeking and Evans' analysis, the stress intensity

Table 3.1: Properties of $Cu_{47.5}Zr_{47.5}Al_5$

ν	E_p (GPa)	E_m (GPa)	$\Delta G(\mathrm{J\,mol^{-1}})$	ϵ^T
0.373 [136]	82 [136]	89 [136]	$2.702T$-1408.52 [172]	0.00137 [144]

factor change calculated for this region only is zero - no impact at all is seen from the transformation around the initial zone. Therefore, the next stage is to consider the effects of an advancing shear band.

When the shear band advances, the transformation zone will be made up of two distinct regions - the transformed region ahead of the tip (which will follow Equation 3.18 for r_c), and the wake of transformed material behind the advancing tip. It is to be expected therefore that the degree of toughening will vary with shear band advance.

A schematic of the transformation zone around an advancing shear band is shown in Figure 3.3. For the purposes of calculation, both the shear band edges and the transformation zone outer edges must be considered in addition to the tip region. For this ahead of tip region, Equation 3.18 is used for values of θ diverging from 0 until the distance from the shear band plane reaches its maximum value, which is denoted the zone height w. Past that point, straight zone sides parallel to the shear band plane at height w are assumed. The end effects are assumed to be negligible, which will introduce a degree of error into calculations for small values of band advance.

The zone height can be calculated from the maximum absolute value of $w = r_c \sin \theta$, which falls at approximately $\theta = \pm\pi/6$ as shown in Figure 3.2. This hence gives the limits between which the ahead of tip integral in Equation 3.25 should be calculated. It should be noted that the transformation radius includes a significant shape strain component - in fact, the shape strain term dominates the transformation radius for this system, due to the very small volume strain. This is reasonable even in cases where variant self-accommodation limits end-product shear strain as a result of transformation - nucleation of the first correspondence variant will be influenced by shape strain before further variants form. Therefore, this radius will be used even when considering
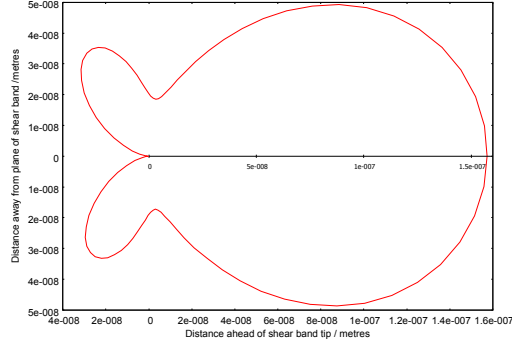
Figure 3.2: Transformation radius r around an example shear band tip.
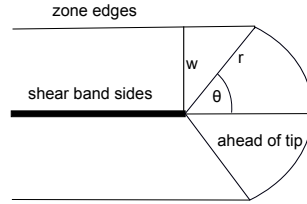
Figure 3.3: Schematic showing an advancing shear band. Zone height w is marked. Note the three regions integrated over - the shear band sides, the zone edges and the near-tip region. It should further be noted that there are two each of the shear band side and zone edge regions.

entirely volume-change-driven toughening.

For the zone sides, the critical radius is given by:

$$r_{c2} = \frac{w}{\sin \theta} \tag{3.26}$$

The zone outward normal is given by:

$$\mathbf{n_2} = \begin{pmatrix} 0 \\ 1 \end{pmatrix} \tag{3.27}$$

Given these expressions, h and dS can be calculated from Equations 3.20 and 3.24. The integral for this section should be calculated from $\theta = \pi/6$ (approximately - an exactly calculated value is used in the full calculation) to $\theta = \arctan \Delta a/w + \pi/2$. Δa is the distance of shear band advance; $\Delta a/w$ hence represents advance relative to the zone height. Shown for demonstration purposes:

$$\Delta K_{II\ zonesides} = \frac{\epsilon^T E}{3(1-2\nu)} \int_{\pi/3}^{\arctan \Delta a/w + \pi/2} \begin{pmatrix} 0 \\ 1 \end{pmatrix} \cdot$$

$$\begin{pmatrix} \sin\left(\frac{\theta}{2}\right)[2 - 2\nu + \cos\frac{\theta}{2}\cos\frac{3\theta}{2}] \\ \cos\left(\frac{\theta}{2}\right)[1 - 2\nu + \sin\frac{\theta}{2}\sin\frac{3\theta}{2}] \end{pmatrix} (\frac{\sqrt{\frac{\sin\theta}{w}}}{2\sqrt{2\pi}(1-\nu)})$$

$$\sqrt{w(\cot\theta^2\csc\theta + \csc\theta^3)d\theta^2 + \frac{w^2}{(\sin\theta)^2}d\theta^2} \quad (3.28)$$

For the shear band sides, $dS = da$, $dr = da$, and:

$$\mathbf{n_3} = \begin{pmatrix} 0 \\ -1 \end{pmatrix} \quad (3.29)$$

The integral in this case is evaluated from $a = 0$ to $a = \frac{\Delta a}{w}w$, for $\theta = \pi$.

$$\Delta K_{II\ band} = \frac{\epsilon^T E}{3(1-2\nu)} \int_{0}^{\frac{\Delta a}{w}w} \begin{pmatrix} 0 \\ -1 \end{pmatrix} \cdot \frac{1}{2\sqrt{2\pi}\sqrt{\mathbf{a}}(1-\nu)}$$

$$\begin{pmatrix} \sin(\pi)[2 - 2\nu + \cos\pi\cos 3\pi] \\ \cos(\pi)[1 - 2\nu + \sin\pi\sin 3\pi] \end{pmatrix} (1 + a^2)da^2 \quad (3.30)$$

The integrals from these regions are calculated for a range of values of crack advance Δa. They are then summed, noting that there are two each of the zone and shear band sides as well as the zone around the tip. Results are shown in Section 3.4.

3.3.2   Shape and Volume Change

The same approach used above for the volume change only case is taken to the calculations when shape change is taken into account. The same regions shown in Figure 3.3 will be integrated over. The major difference will be the use of Equation 3.21 in the place of the simplified Equation 3.22, now that the shape change component of the transformation strain is non-zero.

A number of significant assumptions and simplifications must be made in order to consider the impact of the shape change component. This calculation will hence not be exact but instead serves

Table 3.2: Lattice Parameters for CuZr Austenite and Martensite

Structure	a_m	b_m	c_m	β_m
B2	0.3262	0.3262	0.3262	90°
B19'	0.3278	0.4161	0.5245	103.88°
Superstructure	0.6316	0.8562	0.5331	105.27°

to consider a series of example scenarios - attempting to give insight into what might occur were shape strain to play a significant part, and including attempts at a best case scenario for available toughening that could provide a limiting case.

It is assumed that particles transform into one martensite correspondence variant only - ie that multiple variants do not form to accommodate some of the shape strain. In real systems it is likely that twinning and variant self-accommodation will almost entirely remove the impact of shape strain, so this analysis by its nature considers an extreme scenario.

When applying Equation 3.21, the shape strain to be considered will depend upon the orientation of the transforming particles. In order to obtain the most favourable orientations, the nature of this transformation must be considered. This requires consulting the work of Schryvers [144].

The lattice parameters of the B2 austenite phase, and of the martensite and its superstructure, are reproduced in Table 3.2. The ac plane of the martensite is formed by shearing the (110) plane of the cubic austenite, along with some stretching and rearrangement. There is also a degree of contraction normal to the (110) plane.

The model for the toughening effect of transformation as explained in Section 3.3.1 is entirely in 2 dimensions. Therefore, the 3D behaviour above needs to be condensed into 2 dimensions to calculate its effect, and this will require further simplification.

For the purposes of this analysis the plane with an impact expected to be most favourable to toughening will be considered - that containing the shear, the large expansion term and the smaller of the two contractions. This is the ac-plane of the martensite (the (110) plane of the austenite).
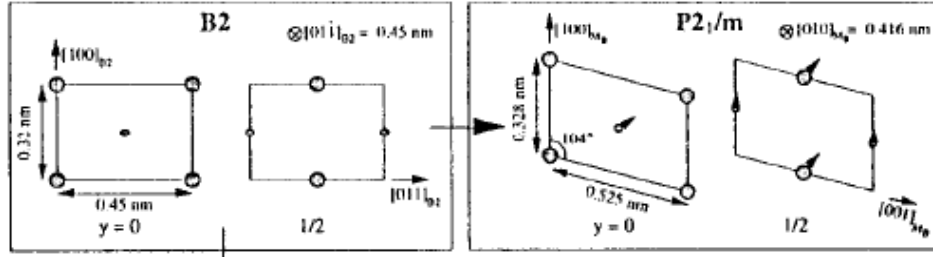
Figure 3.4: Transformation from austenite to martensite in CuZr, showing the austenite (110) plane and the ac-plane of the martensite. From Schryvers [144].

The contraction perpendicular to this plane will be neglected - the shear band being related to a pure Mode II crack means that these terms should not contribute to the stress intensity factor at the tip. The transformation hence consists of a small contraction along the a-axis, a larger expansion on the c-axis and a shear term. This can be seen by comparing the austenite (110) plane to the martensite ac-plane as shown in Figure 3.4.

The orientation of these expansion axes must then be taken into account. A number of possible orientations will be considered in order to build up a picture of the overall behaviour.

For the first case to be considered, the c-axis and direction of shear are aligned along the normal to the transformation zone - this direction will evidently vary for the zone edges, shear band sides, and continually around the ahead of tip region. For the zone sides the transformation matrix is given by:

$$\begin{pmatrix} (a_m/a_0) - 1 & 0 \\ -(a_m/c_m)\sin(\beta_m - \pi/2) & (c_m/(\sqrt{2}a_0)) - 1 \end{pmatrix} \tag{3.31}$$

The same expression is used for the shear band edges, but with the direction of the shear reversed:

$$\begin{pmatrix} (a_m/a_0) - 1 & 0 \\ (a_m/c_m)\sin(\beta_m - \pi/2) & (c_m/(\sqrt{2}a_0)) - 1 \end{pmatrix} \tag{3.32}$$

For the region ahead of the shear band tip, the direction of $\mathbf{n}$ must be considered:

$$
\begin{pmatrix} v_x & s_x \\ s_y & v_y \end{pmatrix}
\tag{3.33}
$$

Where:

$$
\begin{aligned}
v_x &= (a_m/a_0)\cos\left(\beta_m - \pi/2\right))n_y + (c_m/(\sqrt{2}a_0))n_x - 1 & (3.34) \\
v_y &= ((n_y c_m/(\sqrt{2}a_0)) - 1) - (((n_x a_m \cos\left(\beta_m - \pi/2\right))/a_0) - 1) & (3.35) \\
s_x &= -((a_m/c_m)\sin\left(\beta_m - \pi/2\right))n_x & (3.36) \\
s_y &= -((a_m/c_m)\sin\left(\beta_m - \pi/2\right))n_y & (3.37)
\end{aligned}
$$

and where n_x and n_y are the x and y components of the outward zone normal **n**. Note that for all of these three expressions, the shear is given a particular sense (eg positive in Equation 3.32 and negative in Equation 3.31) - calculations are in fact be carried out for the opposite shear as well, to compare these situations.

As an alternate approach to the above situation of rotating particle orientations to align with the zone normal, fixed particle orientations around the transformation zone are also considered. For this case, the following situations are used, with these transformation matrices used all around the transformation region:

$$
\begin{pmatrix} (a_m/a_0) - 1 & 0 \\ -(a_m/c_m)\sin\left(\beta_m - \pi/2\right) & (c_m/(\sqrt{2}a_0)) - 1 \end{pmatrix}
\tag{3.38}
$$

$$
\begin{pmatrix} (a_m/a_0) - 1 & 0 \\ (a_m/c_m)\sin\left(\beta_m - \pi/2\right) & (c_m/(\sqrt{2}a_0)) - 1 \end{pmatrix}
\tag{3.39}
$$

$$
\begin{pmatrix} (c_m/(\sqrt{2}a_0)) - 1 & (a_m/c_m)\sin\left(\beta_m - \pi/2\right) \\ 0 & (a_m/a_0) - 1 \end{pmatrix}
\tag{3.40}
$$

$$
\begin{pmatrix} (c_m/(\sqrt{2}a_0)) - 1 & -(a_m/c_m)\sin\left(\beta_m - \pi/2\right) \\ 0 & (a_m/a_0) - 1 \end{pmatrix}
\tag{3.41}
$$

Corresponding to transformation oriented with shear and axial extension aligned normal to the shear band plane (Equations 3.31 and 3.32) and parallel to the direction of shear band advance (Equations 3.40 and 3.41) respectively.

It should be noted that the above expressions for the transformation strain carry a significant volumetric term as a result of the manner in which they are expressed. As a further point for comparison, the above calculations are repeated with the diagonal terms of the transformation matrix artificially replaced with the bulk 3D volume strain 0.000137.

Having identified the transformation strain matrix ϵ^T to use, Equation 3.21 is now used to calculate the degree of toughening, taking into account the shape strain components. Of particular note is the term $n\epsilon^T h$. Using the same expressions for dS and $\mathbf{n}$ as above (Equations 3.24 and 3.23), the ahead of tip integral can be expressed as:

$$
\begin{aligned}
\Delta K_{II\ tip,shape} = \frac{E}{1+\nu} \int_{-\pi/6}^{\pi/6} (& \begin{pmatrix} -r'_c \sin(\theta) - r_c \cos(\theta) \\ r'_c \cos(\theta) - r_c \sin(\theta) \end{pmatrix} \begin{pmatrix} v_x & s_x \\ s_y & v_y \end{pmatrix} \\
& \frac{1}{2\sqrt{2\pi}\sqrt{r_c}(1-\nu)} \begin{pmatrix} \sin\left(\frac{\theta}{2}\right)[2 - 2\nu + \cos\frac{\theta}{2}\cos\frac{3\theta}{2}] \\ \cos\left(\frac{\theta}{2}\right)[1 - 2\nu + \sin\frac{\theta}{2}\sin\frac{3\theta}{2}] \end{pmatrix} \\
& + \nu e^T \begin{pmatrix} -r'_c \sin(\theta) - r_c \cos(\theta) \\ r'_c \cos(\theta) - r_c \sin(\theta) \end{pmatrix} \frac{1}{2\sqrt{2\pi}\sqrt{r_c}(1-\nu)} \\
& \begin{pmatrix} \sin\left(\frac{\theta}{2}\right)[2 - 2\nu + \cos\frac{\theta}{2}\cos\frac{3\theta}{2}] \\ \cos\left(\frac{\theta}{2}\right)[1 - 2\nu + \sin\frac{\theta}{2}\sin\frac{3\theta}{2}] \end{pmatrix} \frac{1}{1-2\nu}) \sqrt{dr_c^2 + r_c^2 d\theta^2} \quad (3.42)
\end{aligned}
$$

Similar expressions can be developed for the zone edge and band side regions, using the methodology from Section 3.3.1 and Equations 3.31 and 3.32. The full integral can hence be calculated from the five (recalling that there are two each of zone sides and shear band edges) integrals developed here. Calculations are performed, as always, with Wolfram Mathematica 8.0 - code is shown in Appendix A. While the above integral considers the rotating particle orientation case the fixed orientation cases follow the same approach.
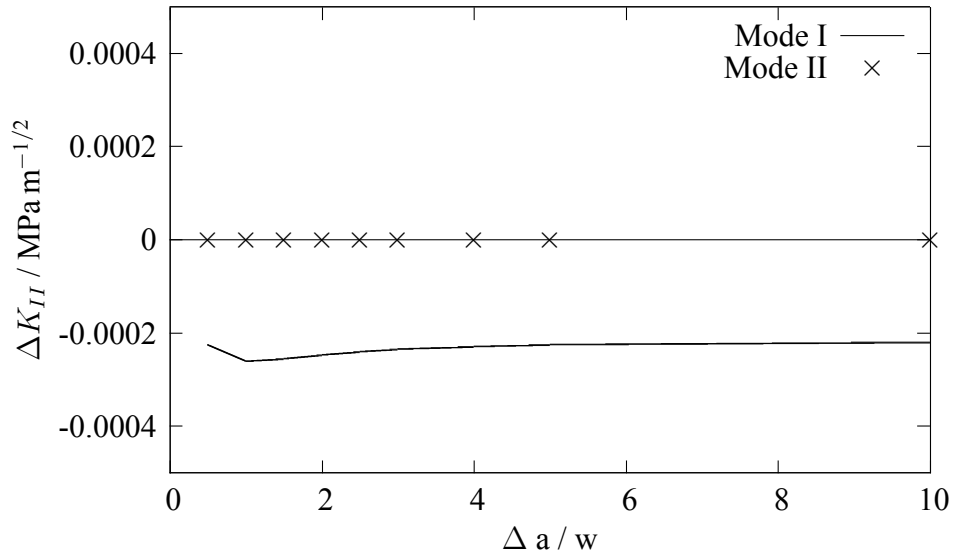
Figure 3.5: Change in shear band tip stress intensity plotted against shear advance relative to transformation zone width, for Mode I and Mode II cases. Note the small absolute values (due to the low volume strain associated with the transformation), the tendency toward steady-state values for Mode I as advance continues, and that the Mode II values are zero for all values of shear band advance.

3.4   Results and Discussion

The objective of the calculations performed has been to determine whether the effect of transforming CuZr crystalline particles in a metallic glass composite can in fact be influencing the stress state at shear bands sufficiently to provide toughening and work-hardening.

Figure 3.5 shows the situation when volume change alone is considered, with the Mode I case included for comparison. Notably, in Mode II, the (very small) positive volume change of transformation had no effect at all on the stress intensity at the shear band tip. However, in either case the effect of volume change is insignificant compared to the initial applied stress intensity of $5\,\mathrm{MPa\,m}^{1/2}$. This fits with the expected result - a negligible volume change leads to very little impact on the shear band tip - though the zero result for Mode II bears more consideration.
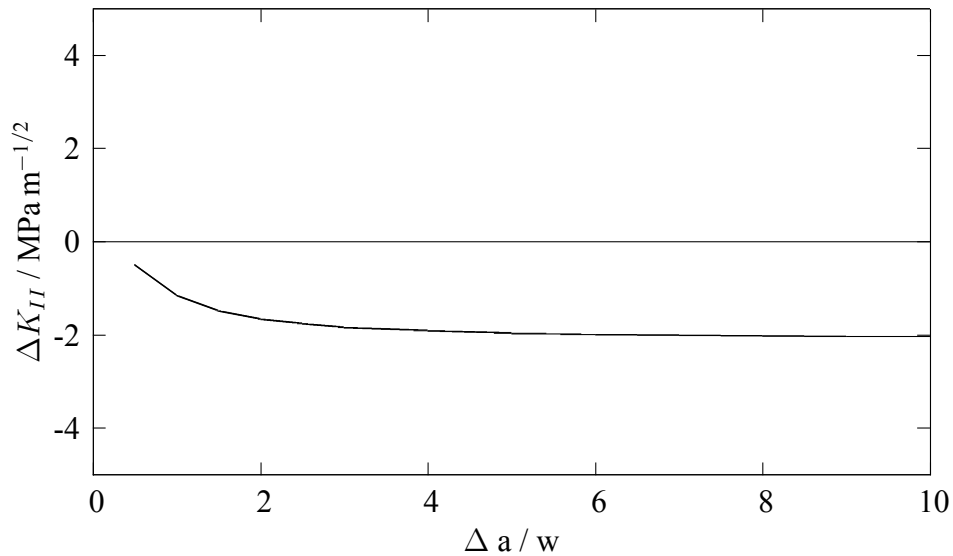
Figure 3.6: Change in shear band tip stress intensity plotted against shear advance relative to transformation zone width, for the case of particles with positive shear direction aligned upward relative to the shear band plane. Note the convergence toward a steady-state value, and appreciable contribution to shear band tip stress intensity. The plot is the same whether or not artificially reduced diagonal terms are used in the transformation strain matrix.

The various calculations considering shear as well as volume components to transformation strain produce more complex output. Figures 3.6, 3.7 and 3.8 show the situation where different variants of a single fixed particle orientation are used around the same region. Two cases with respect to volume components are considered - that with the full (simplified) 2D transformation matrix, and that with the diagonal terms artificially reduced to match the (very small) 3D volume strain - however this produces no change in the model output for cases of fixed shear direction, and so is not explicitly shown.

In the case where the shear direction is rotated to follow the tangent to the zone perimeter at any given point, the terms from above and below the shear band cancel out exactly with one another, leading to zero contribution to shear band tip stress intensity - as with the volume only case, a result bearing further consideration. (This zero result is not reproduced graphically).
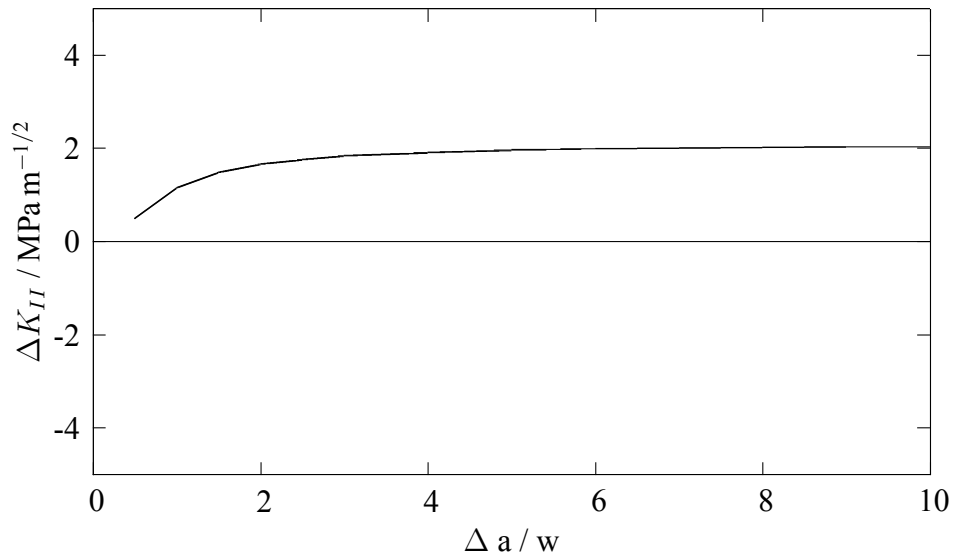
Figure 3.7: Change in shear band tip stress intensity plotted against shear advance relative to transformation zone width, for the case of particles with positive shear direction aligned downward relative to the shear band plane. Note the convergence toward a steady-state value, and appreciable contribution to shear band tip stress intensity. The plot is the same whether or not artificially reduced diagonal terms are used in the transformation strain matrix.
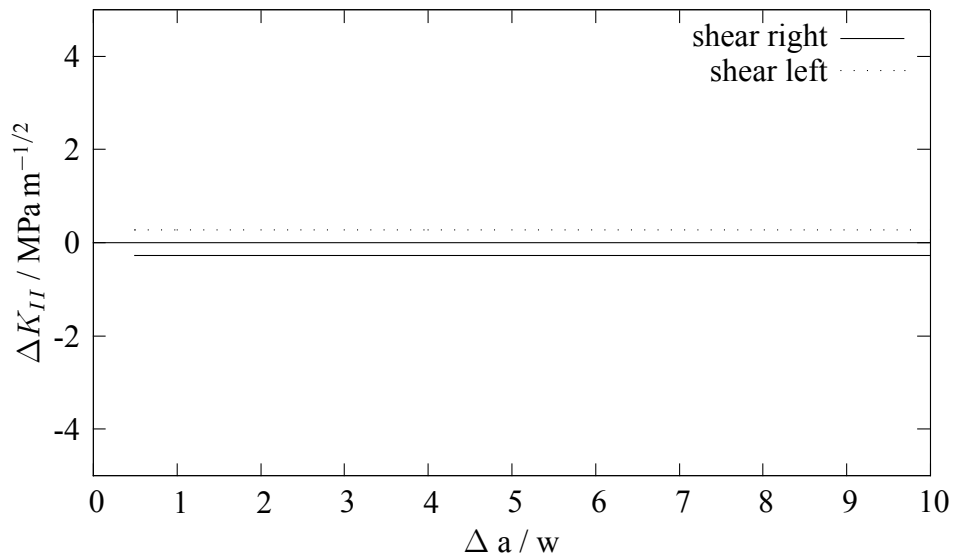
Figure 3.8: Change in shear band tip stress intensity plotted against shear advance relative to transformation zone width, for the case of particles with positive shear direction aligned sideways relative to the shear band plane. The toughening takes a constant value, positive for shear leftward and negative for shear rightward - the only contribution being from the ahead of tip region. The plot is the same whether or not artificially reduced diagonal terms are used in the transformation strain matrix.
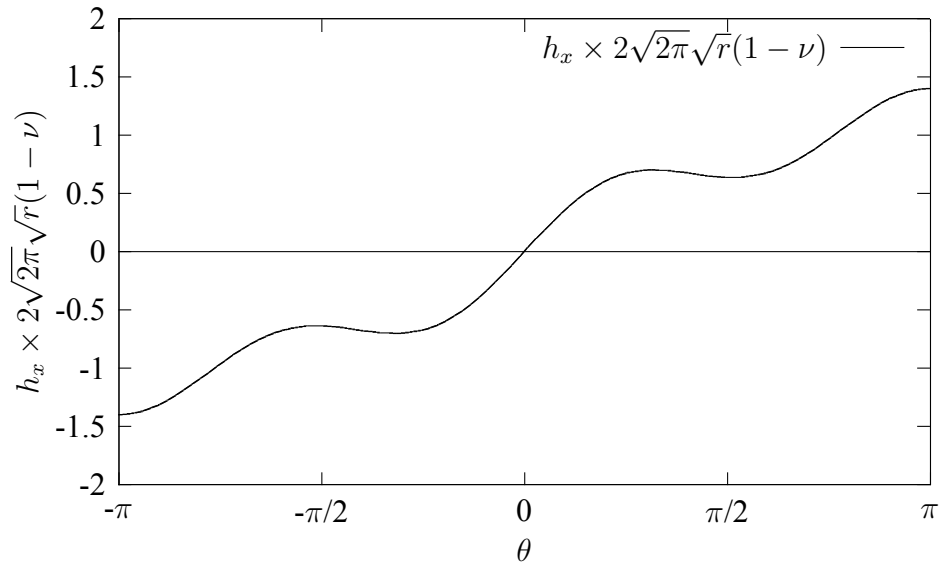
Figure 3.9: Horizontal component of weight function **h** against θ. Note that the function is antisymmetric about $\theta = 0$.
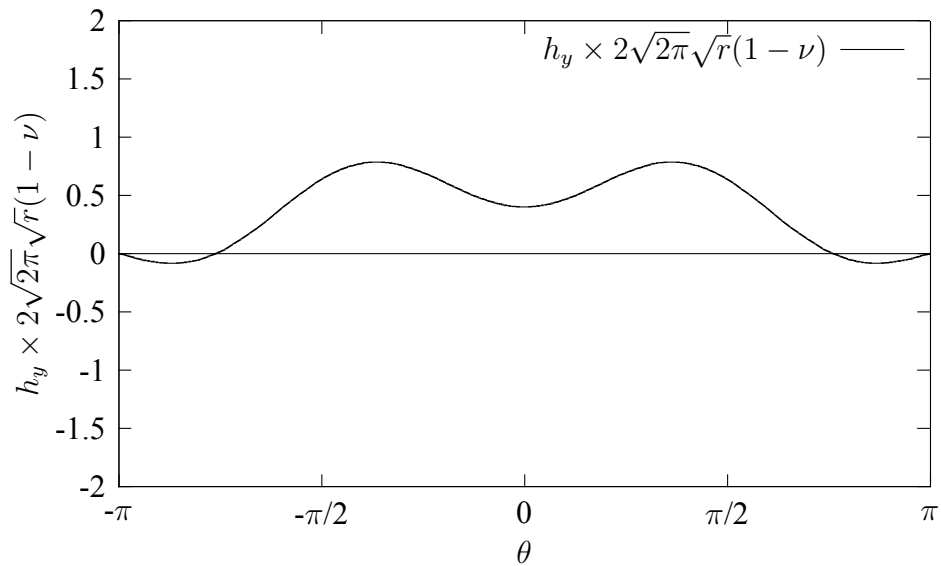
Figure 3.10: Vertical component of weight function **h** against θ. Note that the function is symmetric about $\theta = 0$.

It can immediately be observed that the magnitude of the contributions to shear band tip stress intensity from the shear terms can be significantly larger than those from the volume-change-only case. However, those contributions depend significantly on the direction of the shear.

From McMeeking and Evans' work [123], for the Mode I case and volume change only, the three distinct regions integrated over come together to give a contribution to stress intensity that rapidly moves to a steady-state value. This is due to the terms from the zone edges (positive) and band/crack sides (negative) opposing one another - the ahead of tip region will only ever contribute a constant factor, as it is not impacted by crack or shear band advance. This can be understood by considering the far-field limit: for very large values of shear band advance, the shear band side and transformation zone edge fall at approximately the same r and θ, and so their contributions will only be distinguished by the positive or negative sign of the normal $\mathbf{n}$, hence cancelling out. Only at shorter length scales will the contributions from these regions be differentiated by r and θ.

Similar behaviour is observed here for the Mode II cases with fixed transformation strain orientation normal to the shear band plane (Figures 3.6 and 3.7). Steady-state behaviour is observed after a certain degree of shear band advance, driven by opposing zone edge and shear band side terms. However, whether the contribution is positive (indicating embrittlement) or negative (indicating toughening) is dependent on the direction of the shear.

When the orientation of the transformation strain is rotated about the edge of the transformation zone to a favourable orientation, the band side and zone edge cancel out for all values of band advance - leading to zero contribution to shear band tip stress intensity. There remains, however, a constant term corresponding to the ahead of tip region. The same is observed with a transformation strain aligned sideways with respect to the shear band plane - with the magnitude of the ahead of tip term positive or negative depending on whether the shear aligns left or right.

The results obtained when using the full diagonal terms of the simplified 2D transformation matrix, and those using artificially reduced terms to represent the 3D volume strain, are exactly the same - indeed the volume terms have precisely zero contribution to shear band tip stress intensity in Mode II. To understand this result, and the lack of band advance dependence of the shear-sideways and rotating-shear cases, the nature of the expression used to calculate this contribution must be considered.

94

The expression **h** can be split into its x and y components, depicted in Figures 3.9 and 3.10 respectively. It can immediately be observed that h_x is antisymmetric about $\theta = 0$, where h_y is symmetric. Now consider the full expression $\mathbf{ne^T h}$, and break it down into its component terms:

$$\mathbf{ne^T h} = n_x v_x h_x + n_x s_x h_y + n_y s_y h_x + n_y v_y h_y \tag{3.43}$$

where the shear matrix is taken as:

$$\begin{pmatrix} v_x & s_x \\ s_y & v_y \end{pmatrix} \tag{3.44}$$

It should be observed that of the components of **n**, n_x will be symmetric about $\theta = 0$ and n_y will be antisymmetric. The volume components v_x and v_y are assumed not to change with θ, and for the cases of fixed shear direction, s_x and s_y will also remain constant throughout the calculation (this will be complicated somewhat when the shear direction is rotated to follow the zone perimeter tangent).

The only term containing v_x also contains n_x (symmetric about $\theta = 0$ and h_x (antisymmetric about $\theta = 0$). Therefore, the term is antisymmetric about $\theta = 0$, and the terms from above and below the shear band tip will exactly cancel with one another to produce zero overall contribution. The same can be seen for the only term containing v_y, which also contains n_y (antisymmetric) and h_y (symmetric). Therefore, the volume terms have zero impact on the output of the integral.

The terms in s_x and s_y are symmetric about $\theta = 0$, assuming that s_x and s_y remain unchanged over the entire system, hence contributions are seen from these shear terms. However, if these terms are reversed in direction below the shear band tip as was applied for the rotating shear direction, these terms will also cancel out and produce no contribution, as observed.

It is worth recalling that in a real system, the particles surrounding the transformation zone are unlikely to all be in completely the same alignment or to transform in exactly the same way. The above represent a few example cases to develop an understanding of the behaviour that transformations can cause.

The shear contributions for opposite orientations of shear (not including the diagonal terms) are exactly opposite. In a situation where the transformation direction of particles around the transfor-

mation zone was entirely randomly distributed, for sufficient particles, the shear terms would hence play no role. Toughening would be determined entirely by the volume component of transformation strain (which in the Cu-Zr system is very small). For cases with local anisotropy (including those with few individual particles to transform, hence too small a sample for complete cancellation of effects), some kind of bias by the shear term might be expected. It is entirely possible of course that the applied stress might itself bias the transformation direction, but even then self-accommodation must be remembered.

(It should be noted that the twinned nanocrystals observed in Eckert's work - see Figure 2.19 - clearly show the formation of multiple variants. Deformation of the particles by post-transformation deformation makes it difficult to tell if any shape change has occurred, but the presence of many opposed variants suggests otherwise.)

In summary, what has been observed here is that the volume component of transformation alone cannot explain the toughening behaviour observed in the work of Eckert's group into metallic glass composites in the Cu-Zr system, since its contribution to shear band tip stress intensity factor is both too small, and positive.

The shear term could have a theoretical impact were orientations of particles and of transformation to be favourable, and were variant self-accommodation not to significantly reduce the impact of these terms. However, in practice, orientations are unlikely to be completely favourable, and multiple martensite variants/twinned regions are observed to form both in ceramics [176] and in metallic glass matrix composites [177] [139]. These factors make it significantly unlikely that the effect of transformation on the shear band tip can in fact be responsible for the observed toughening and work-hardening behaviour, unlike the oft-quoted narrative from the literature.

3.4.1   Other Explanations and Further Work

Given that the traditional explanation for transformation toughening has been called into question by the above work in metallic glass matrix composites, some other mechanism must be driving the unusual observed work-hardening and toughening behaviour.

Perhaps the simplest alternate explanation is that which appears both in the work of Wu [138]

and also in work by Eckert's group [140] suggesting simply that the transformation of the reinforcement into the significantly harder martensite phase is responsible for the observed work-hardening. This very simple approach would appear to encapsulate much of the observed behaviour in systems with large crystals, but is not so helpful in the case of precipitated nanocrystals.

Precipitation of nanocrystals by rearrangement during deformation, and twinning or martensitic transformation of those particles, could still compete with STZ activation and provide a mechanism for toughening. Similarly, the mechanism whereby particles twin and harden, counteracting the local softening effect of STZ activation and preventing runaway shear banding, remains viable. All that this work has done is called into question the section of narrative concerning the volume change associated with transformation impacting the shear band stress state and toughening the material in a similar way to a traditional transformation-toughened alloy or ceramic.

It is worth considering further possibilities. It should be noted that metallic glasses deform in a very different manner to crystalline materials. Typical approaches to toughening them involve the promotion of multiple shear bands to distribute deformation, rather than catastrophic failure along a single band as is seen in the more brittle metallic glasses. In order to achieve this, shear band initiation is encouraged and shear band propagation made difficult.

This poses the question as to whether transformation of reinforcement particles might have an impact on shear band initiation. Perhaps the most intuitive way this might be the case is via the particle-matrix interface. There has been very little research into the precise nature of the crystal-particle interface, so it is difficult to say precisely how it might be impacted by transformation. Nonetheless, while at larger scale shear is minimised by variant self-accommodation, the formation of each variant is likely to have an impact on the interface adjacent to it - potentially disrupting the adjacent region and increasing its viability as an initiation site for shear bands. This could also make it easier for the particle-matrix interface to deflect and absorb shear bands that contact the particle, inhibiting propagation. Certainly the interfacial region is important, as raised by Wu et al [138] who identify it as the source of initiation of large numbers of non-critical shear bands (and also the eventual site of fracture).

Fluctuation microscopy is an imaging technique often used to probe the nature of medium-range order. Using a transmission electron microscope, normalised intensity variation in a dark-

field image ('speckle') can be used as a measure of the degree of medium-range order present in the small volume of sample measured. The principle is that an ordered region with randomly oriented clusters will have some aligned close to the Bragg diffraction condition (producing a bright spot) and some far from said condition (hence a dark spot). A less ordered region will show less variation in scattered intensity. Furthermore the ordered region will show more ordered structures when sample volume or scattering angle are varied than the amorphous regions. This can be used to produce a qualitative measure of medium range order.

Applying fluctuation microscopy to the interface region of a metallic glass matrix composite, taking a series of images moving toward and over the interface, should give an idea as to how ordering behaves in the vicinity of the interface. This would provide information hopefully of significant interest to non-transforming composites. To consider the transformation case, a sample should be prepared from a post-deformation sample (x-ray diffraction and differential scanning calorimetry should be used to ensure that significant transformation has taken place, alongside direct tem imaging of the particle to ensure it is now martensitic). The ordering in the interface region should be compared with that in the undeformed sample to see whether transformation has caused any change in medium-range order. The same experiments should carried out in a non-transformation-toughening composite to control for the general effects of deformation on the matrix-particle interface.

The application of this technique could bear significant light on the effects of transformation on the particle-matrix interface, and hence potentially lend weight to or help rule out the supposition that disruption around the interface is important in shear band nucleation and blocking.

Chapter 4

Metallic Glass through the Lens of Granular Media

4.1   Introduction

The review of the literature presented in Section 2.6 carries a strong message: that metallic glasses and granular materials are not all that different. Methodologies that were developed for use in granular media are frequently used to model BMGs. A model for describing stress-dilatancy in terms of the collective buckling of force chains was identified as a candidate for adaptation. That model will here be explained in full, and its predictions will be applied to the theory of metallic glasses.

The methodology of Tordesillas et al [3] [4] will be followed closely, so those works can form an accompaniment to this investigation.

4.2   Buckling of a Single Force Chain

The first step is to determine the conditions required for buckling of a single force chain in isolation - the following will explain the method of Hunt [4] as used to inform Tordesillas' later work [3]. Consider a force chain made up of N+2 particles. These particles are modelled as uniform discs

of radius R. A load F is applied to the end of the chain axis, and the particles move against a series of elastic springs. Particles are supported laterally by a spring of stiffness k_s. Tangential sliding and rotation of particles against one another are covered by stiffnesses k_t and k_r respectively. These spring constants will be expressed as fractions of the spring constant k_n which represents compression of the particles and hence controls axial compression of the force chain.

It is assumed that the force chain is perfectly straight and does not contain any imperfections. This is evidently a simplification, as in real systems failure is likely to be dictated by the flaws in the structure. The model will hence overestimate yield strengths and the difficulty of buckling - nonetheless it still carries significant information about the mechanics of force chain systems. It is further assumed that particles themselves do not deform plastically, whereas in real metallic glasses clusters can undergo deformation. The model operates in two dimensions.

A term q_i is defined for the i-th particle such that its lateral displacement is given by $q_i R$. Its rotation from vertical in the clockwise direction is denoted ω_i.

Figure 4.1 shows these angles and displacements for two arbitrary adjacent particles partway through buckling (for convenience of identification in the following derivations, various key lines have been numbered). Figure 4.2 then shows these particles as they would appear after rolling over one the other to bring the centrelines parallel as they would have been prior to buckling. The remaining distance across the particle surfaces between the centrelines, denoted d_i, is the distance of sliding against the spring constant k^t. The angle through which the top particle needs to be rotated to bring the centrelines parallel again is denoted $\psi_i = \omega_{i+1} - \omega_i$ and is moved against the spring constant k^r.

It is possible to calculate analytical expressions for d_i as well as the axial compression between the two particles Δ_i (as shown between lines 6 and 8 in Figure 4.1) in terms of each particle's lateral movement and rotation q_i and ψ_i.

By considering the right-angled triangle of sides $2R - \Delta_i$, $R(q_{i+1} - q_i)$ and hypotenuse $2R$ between lines 1, 4 and 6 as seen in Figure 4.1, applying Pythagoras, rearranging and applying solving the resulting quadratic it is possible to obtain:
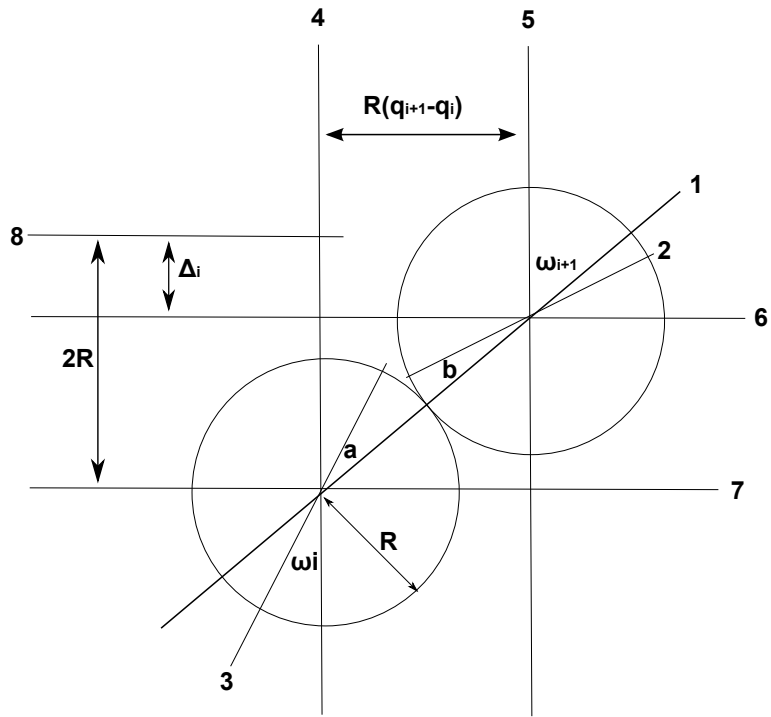
Figure 4.1: Adjacent particles i and $i + 1$ post buckling.
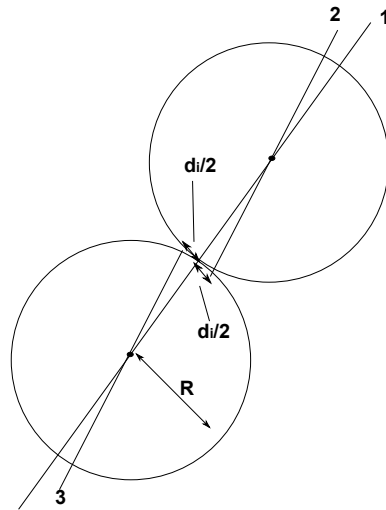
Figure 4.2: Adjacent particles i and $i + 1$ post buckling, having been rotated so as to bring the former centrelines back parallel. The remaining distance d_i is hence the distance the particles slid across one another during deformation.

$$\Delta_i = 2R \left(1 - \sqrt{1 - (\frac{q_{i+1} - q_i}{2})} \right) \tag{4.1}$$

The angles a and b here represent the angles between the former centrelines of particles i and i+1 (lines 2 and 3 in Figure 4.1), and the line joining their centres in current position (line 1). For the former centrelines to be made parallel again, they must by simple geometry move so that they fall equidistant in angle from that line. This can be used to calculate the arc length d_i remaining to slide through to unite the centrelines after they are realigned. This is given by $R(a - b)$, and is moved against the spring constant k^t.

Consideration of the right-angled triangle between lines 1, 4 and 6 allows $a = \arcsin \frac{q_{i+1} - q_i}{2} - \omega_i$ to be obtained. Similarly $b = \omega_{i+1} - \arcsin \frac{q_{i+1} - q_i}{2}$ can be found from the triangle defined by lines 1, 5 and 7. This gives:

$$d_i = R \left[2 \arcsin \frac{q_{i+1} - q_i}{2} - \omega_{i+1} - \omega_i \right] \tag{4.2}$$

The next step is to develop a potential energy equation for the system. By considering the energy accumulated in the three spring constants k_s, k_r and k_t by the motion of each particle, and also the energy put into axial compression, the following expression can be developed:

$$V = \frac{1}{2} k_s R^2 \sum_{i=0}^{N+1} q_i^2 + \frac{1}{2} k_t \sum_{i=0}^{N} d_i^2 + \frac{1}{2} k_r R^2 \sum_{i=0}^{N} \psi_i^2 - F \sum_{i=0}^{N} \Delta_i \tag{4.3}$$

This can be simplified with a few basic assumptions. In the expression for d_i, the Taylor expansion for the arcsin function can be used. For small angles, just the first-order term can be applied, resulting in:

$$d_i \approx q_{i+1} - q_i - \omega_i - \omega_{i+1} \tag{4.4}$$

Similarly the first-order Taylor expansion for the square root term in Equation 4.1 is taken. Using these expressions and $\psi_i = \omega_{i+1} - \omega_i$ the following simplified potential energy expression is obtained:

$$V = \frac{1}{2}k_s R^2 \sum_{i=0}^{N+1} q_i + \frac{1}{2}k_t R^2 \sum_{i=0}^{N} (q_{i+1} - q_i - \omega_{i+1} - \omega_i)^2$$

$$+ \frac{1}{2}k_r R^2 \sum_{i=0}^{N} (\omega_{i+1} - \omega_i)^2 + \frac{1}{4}FR \sum_{i=0}^{N} (q_{i+1} - q_i)^2 \quad (4.5)$$

In order to solve this potential energy equation to obtain useful outputs, the methods published in Hunt and Thompson's earlier book on elastic stability [178] are expanded.

According to that theory, the solutions to the above potential energy equation (and hence the buckled force chains themselves) will take a sinusoidal form. To approach this, q_i and ω_i can be broken down into Fourier terms as follows:

$$q_i = \sum_{m=0}^{n+1} u_m \sin\left(\frac{im\pi}{N+1}\right) \quad (4.6)$$

$$\omega_i = \sum_{m=0}^{n+1} \phi_m \cos\left(\frac{im\pi}{N+1}\right) \quad (4.7)$$

where m is a wavenumber corresponding to the failure mode in question, and hence u_m and ϕ_m represent amplitudes for the displacement and rotation terms of those modes. Substituting these into Equation 4.5 gives:

$$W = \frac{1}{2}k_s R^2 \sum_{i=0}^{N+1}\sum_{m=0}^{N+1} u_m \sin\left(\frac{im\pi}{N+1}\right) + \frac{1}{2}k_t R^2 \sum_{i=0}^{N} \left(\sum_{m=0}^{N+1} u_m \sin\left(\frac{(i+1)m\pi}{N+1}\right)\right.$$

$$\left. - \sum_{m=0}^{N+1} u_m \sin\left(\frac{im\pi}{N+1}\right) - \sum_{m=0}^{N+1} \phi_m \cos\left(\frac{(i+1)m\pi}{N+1}\right) - \sum_{m=0}^{N+1} \phi_m \cos\left(\frac{im\pi}{N+1}\right)\right)^2$$

$$+ \frac{1}{2}k_r R^2 \sum_{i=0}^{N} \left(\sum_{m=0}^{n+1} \phi_m \cos\left(\frac{(i+1)m\pi}{N+1}\right) - \sum_{m=0}^{n+1} \phi_m \cos\left(\frac{im\pi}{N+1}\right)\right)^2$$

$$+ \frac{1}{4}FR \sum_{i=0}^{N} \left(\sum_{m=0}^{n+1} u_m \sin\left(\frac{(i+1)m\pi}{N+1}\right) - \sum_{m=0}^{n+1} u_m \sin\left(\frac{im\pi}{N+1}\right)\right)^2 \quad (4.8)$$

It should be noted that while u_i and ω_i are broken down into terms consisting of a sum of Fourier modes, the approach taken here considers which of these individual modes will fail first. This can be achieved by investigating each Fourier mode (defined by its wavenumber m) separately, noting

that should any components of other higher-energy modes be introduced at the point of buckling equilibrium, this should always serve to increase the energy of the system and move buckling to a larger load.

The objective therefore becomes to determine which failure mode will activate at the lowest applied force F_{min}. In order to do this, constraints must be used to reduce the system to N degrees of freedom. Boundary conditions are set such that end particles have $q_i = 0$ and symmetric rotation $\omega_{i-1} = \omega_{i+1}$ (if reversing the boundary conditions to allow end particle movement, the sine and cosine terms in Equations 4.6 and 4.7 should be swapped). By inspection of Equation 4.6 it can be seen that q_i will be 0 where m is 0 or N+1, hence the terms u_0 and u_{N+1} never appearing in this analysis.

In order to obtain the critical conditions required for buckling the system is considered at the point of equilibrium between buckled and straight chain configurations. Considering the $m = 0$ case, one rapidly finds the cosine term for ω_i to be 1, and hence ω_i to be given by ϕ_0 for all i. Hence, it must be the case that $\phi_0 = 0$ in order to permit valid equilibrium. The same line of argument can also be used to give $\phi_{N+1} = 0$. This leaves $2N$ unknowns remaining.

This equilibrium condition also implies that $\frac{\delta W}{\delta \phi_0} = \frac{\delta W}{\delta \phi_{N+1}} = 0$, given energy must be the same between the buckled and unbuckled configurations at equilibrium, and these end particles are fixed by the boundary conditions so unable to move laterally. It can therefore be found that $\phi_0 = \phi_{N+1} = 0$.

This, following Hunt's method, further leads to the series of equations:

$$\frac{\partial^2 W}{\partial \phi_i \partial u_i}\bigg|^0 u_i + \frac{\partial^2 W}{\partial \phi_i^2}\bigg|^0 \phi_i = 0 \qquad (4.9)$$

With the superscript 0 denoting that the system is evaluated in its undeflected state. Noting that:

$$\frac{\partial W}{\partial \phi_m} = \frac{\partial W}{\partial \omega_i}\frac{\partial \omega_i}{\partial \phi_m} + \frac{\partial W}{\partial \omega_{i+1}}\frac{\partial \omega_{i+1}}{\partial \phi_m} \qquad (4.10)$$

Working through these equations (using Wolfram Mathematica 8.0 - the code used can be found in Appendix B) gives a series of expressions for ϕ_i in terms of u_i. Substituting these back into W gives a potential equation only in terms of u_i which we denote A. Setting the second differential

of A with respect to each u_i as zero, these equations can be solved for F, giving a buckling force F_{min} for each unique value of the wavenumber m from 1 to N. The buckling mode with the lowest buckling force, denoted as F_{crit}, is the mode that operates.

4.2.1   Buckling Segments

Consider a half-wavelength section of force chain undergoing buckling, from crest to crest. This segment is under the same boundary conditions as the chain as a whole - it does not matter to the segment in question whether the half-wavelengths to either side are buckled or not. As such, it is possible for that segment to buckle and the rest of the chain to remain straight. The shortest possible half-wavelength buckling segments contain K particles, where K is given by:

$$K = \frac{N+1}{m_{crit}} + 1 \tag{4.11}$$

This value K can, where multiple force chains buckle together, be considered as a shear band width.

4.3   Collective Buckling

The buckling of a single force chain does not in and of itself carry information on dilatancy. In order to obtain expressions for stress-dilatancy in the sense of Rowe [157], the collective action of assemblies of force chains must be considered. This analysis follows closely the work of Tordesillas [3].

Consider an assembly of M force chains, each containing $N + 2$ particles as in the above analysis. These force chains are perfectly parallel and start and end level with one another, with either side of the assembly bounded by a loose network of elastically supporting particles. A force exerted on the ends of the chains results in an equally applied axial stress σ_1.

At a critical load F_{crit} determined by the above single-chain-buckling analysis (and hence dependent on R and the spring constants k^s, k^r and k^t), the force chains will collectively buckle. If
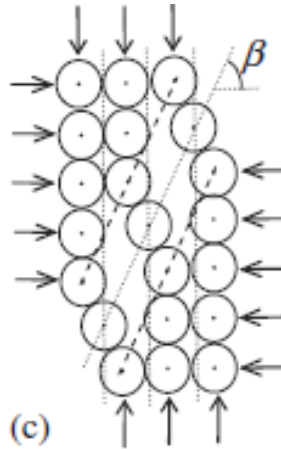
Figure 4.3: Assembly of collectively buckling force chains, showing voids opening. From Tordesillas et al [3]

the chains buckle at different positions, voids will open up in the structure, as shown in Figure 4.3. This is the source of dilatant behaviour in the system.

For the purposes of this analysis, a band of buckled segments is considered to run from one corner of the assembly to the diagonally opposite corner. Consider a line from the middle particles of these end buckling segments - that line is inclined at an angle β to the horizontal, and can be thought of as a shear band angle. By considering the right-angled triangle in Figure 4.4, it can be seen that there must be $(M - 1)\tan\beta + K$ particles in each force chain.

As the system is axially compressed and buckling occurs, the system will grow laterally. Quantifying this will lead to a description of dilatant behaviour.

Given an axial compression due to buckling Δ_b, the key step is to determine the associated lateral movement x of the particles at either end of the buckling segment from a central starting position. Tordesillas gives an expression for this, but references it to an unpublished manuscript and gives no derivation - it is hence derived in full here for purposes of verification.

In order to ascertain this relation, the particles are assumed to stay in direct contact (so as to continue to act as a force chain) and this constraint is used to link the behaviour in the x and y directions. Consider the situation of two adjacent particles i and $i + 1$ as described in Figure 4.5.

The right-angled triangle shown will allow lateral and axial movement to be connected. Simple
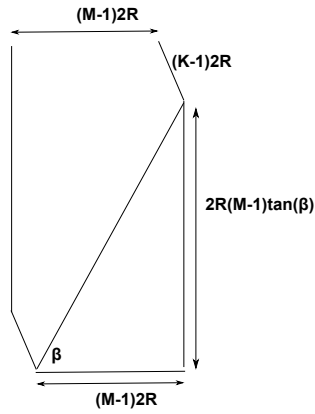
Figure 4.4: Assembly of collectively buckling force chains, showing the relations between assembly size M, shear band angle β and buckling segment length K
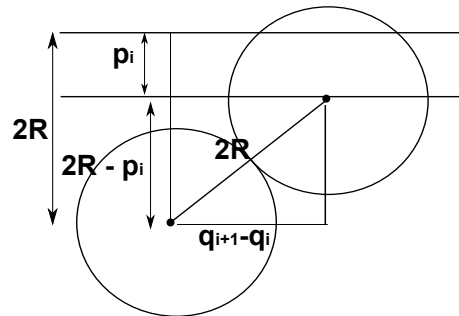
Figure 4.5: Two adjacent particles, the contact of which will be used to find the lateral displacement x of the end particles of a buckling segment.

Pythagoras gives:

$$(2R)^2 = (2R - p_i)^2 + (q_{i+1} - q_i)^2 \tag{4.12}$$

It should further be noted that the sum of the individual axial compressions between each pair of particles forms the overall buckling axial displacement:

$$\sum_{i=0}^{K-2} p_i = \Delta_b \tag{4.13}$$

Rearranging Equation 4.12 results in the following quadratic:

$$p_i^2 - 4Rp_i + (q_{i+1} - q_i)^2 = 0 \tag{4.14}$$

The next stage requires the expression for q_i:

$$q_i = u_m \cos \frac{im\pi}{N+1} \tag{4.15}$$

For a particular known failure mode, u_m can be treated as a constant, though this constant remains unknown and must be found to obtain a valid expression for x. The buckling mode wavenumber m can be expressed in terms of N and K, and substituted into the expression for q_i:

$$m = \frac{N+1}{K-1} \tag{4.16}$$

$$q_i = u_m \cos \frac{i\pi}{K-1} \tag{4.17}$$

Substituting into Equation 4.14 and solving for p_i gives:

$$p_i = 2R \pm R\sqrt{4 - u_m^2(\cos \frac{i\pi}{K-1} - \cos \frac{(i+1)\pi}{K-1})^2} \tag{4.18}$$

Summing p_i from 0 to K-2 as shown in Equation 4.13, an expression for Δ_b is found:

$$\Delta_b = \sum_{i=0}^{K-2} 2R - R\sqrt{4 - u_m^2(\cos \frac{i\pi}{K-1} - \cos \frac{(i+1)\pi}{K-1})^2} \tag{4.19}$$

This expression can now be used to find u_m, and hence x. A first-order Taylor expansion for the square root term is used:

$$\Delta_b = 2R(K-1) - \sum_{i=0}^{K-2} 2R(1 - \frac{u_m^2}{4}(\cos\frac{i\pi}{K-1} - \cos\frac{(i+1)\pi}{K-1})^2) \qquad (4.20)$$

Rearranging for u_m:

$$u_m^2 = \frac{4\Delta_b}{R\sum_{i=0}^{K-2}(1 - \frac{u_m^2}{4}(\cos\frac{i\pi}{K-1} - \cos\frac{(i+1)\pi}{K-1})^2)} \qquad (4.21)$$

It should here be noted that x can be found via the sum of the differences of particle lateral displacements:

$$x = \frac{R}{2}\sum_{i=0}^{K-2} q_{i+1} - q_i \qquad (4.22)$$

$$= \frac{R}{2}(q_{K-1} - q_0) \qquad (4.23)$$

Noting that $\cos(\pi(K-1)/K-1) = \cos\pi = -1$, and $\cos 0 = 1$:

$$x = -Ru_m \qquad (4.24)$$

$$= \sqrt{\frac{4R\Delta_b}{\sum_{i=0}^{K-2}(1 - \frac{u_m^2}{4}(\cos\frac{i\pi}{K-1} - \cos\frac{(i+1)\pi}{K-1})^2)}} \qquad (4.25)$$

$$= \sqrt{\frac{4R\Delta_b}{D}} \qquad (4.26)$$

Where D is given by:

$$D = \sum_{i=0}^{K-2}(1 - \frac{u_m^2}{4}(\cos\frac{i\pi}{K-1} - \cos\frac{(i+1)\pi}{K-1})^2) \qquad (4.27)$$

This is consistent with the expression in the source paper, and can be used to express dilatant behaviour in a number of ways. Most simply, the strain rates in the y and x directions can be expressed as:

$$\epsilon_1 = \frac{\Delta}{2R((M-1)\tan\beta + K)} \qquad (4.28)$$

109

$$\epsilon_2 = \frac{x}{MR} \tag{4.29}$$

$$= \sqrt{\frac{4\Delta_b}{DRM^2}} \tag{4.30}$$

where Δ is the overall axial shortening. These can be used fairly directly - plotting $\epsilon_1 + \epsilon_2$ against ϵ_1 for example, showing volume strain changes as deformation progresses. Similarly a dilatancy parameter relating volume and shear strains can be expressed as:

$$\sin \psi^* = -\frac{\epsilon_1 + \epsilon_2}{\epsilon_1 - \epsilon_2} \tag{4.31}$$

These relations carry significant information about the state of the system and the material properties involved. They represent a potent method for investigating influences on the dilatant behaviour of granular materials and potentially of metallic glasses.

4.4 Calculations

While the work of Tordesillas and of Hunt [3] [4] identify a powerful mathematical model, they present little in the way of context or potential usage. A few example outputs are shown for arbitrary inputs, showing variation of outputs with some of the input parameters, but no detailed attempt to link the model to a real physical system is made.

Here the relevance of the model to bulk metallic glasses will be considered, since those systems display many similarities to granular systems. For the purposes of this analysis, the structural unit (corresponding to particles in the model) will be the cluster, as per Miracle's model [19], and supported by the extension of Gourlay's work in 2.6 as shown in Figure 2.22. A value of $R=$ 5×10^{-10} m is taken for the particle (cluster) size.

In Tordesillas' analysis, values of the spring constants k^r, k^t and k^s are expressed as fractions of the axial compression spring constant k^n. This convention will be followed here. A value for k^n is estimated by considering a typical Zr-based metallic glass. ($Zr_{55}Cu_{30}Al_{10}Ni_5$, E=84.4 GPa). [179]. Considering axial compression of a single force chain under applied force F, $E = \sigma_1/\epsilon_1$, where $\sigma = F/(\pi R^2)$ and $\epsilon_1 = x/(2R(N+1))$. Each interparticle spring compresses by $x = F/k^n$, and there are $N + 1$ of these springs. Combining these expressions, k^n is calculated to be 64.078.
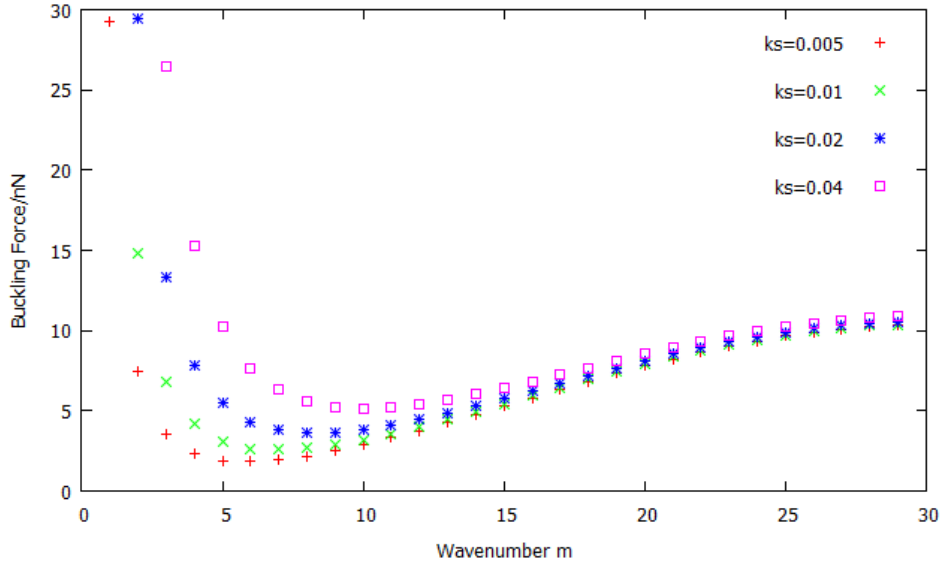
Figure 4.6: Lowest force required to buckle force chain for varying wavenumber m, calculated for four values of k_s at fixed k_r, k_t

Given Tordesillas' paper showing limited variation of buckling behaviour beyond force chain lengths of circa 10 particles [169], a force chain length given by $N = 29$ has been selected, intended to be large enough to minimise the impact of periodic behaviour and yet remain realistic for metallic glass systems.

4.4.1 Buckling Force and Shear Band Width

The first calculation to perform is that required to obtain the minimum force required for buckling. Calculations are performed with the help of Wolfram Mathematica 8.0. Inputs are k^r, k^t, k^s (all expressed as functions of k^n), R, N. For any given set of inputs, the buckling force for each integer value of wavenumber m from 1 to N must be calculated. The lowest force that corresponds to an allowed wavenumber - ie leading to an integer value of segment length or shear band width $K = ((N + 1)/m_{min}) + 1$ - will then be the buckling force, and this wavenumber will define the buckling mode (which can hence also be considered a model output). Some example lowest-force curves are shown in Figure 4.6, for varying k^s with fixed $k^r = 0.16k_n$ and $k^t = 0.16k_n$. Note the clear trough in which the critical mode will fall.
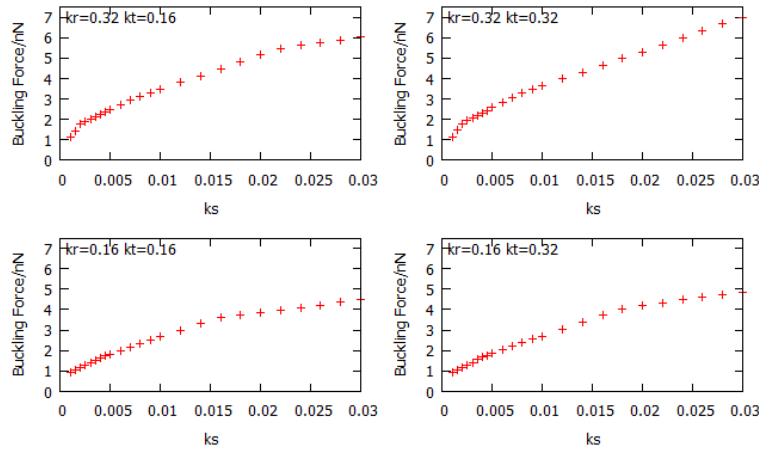
Figure 4.7: Lowest force required to buckle force chain for varying k_s, calculated for four combinations of k_t and k_r

The objective here is to determine the effects of the input spring constants on the force required for buckling (and hence yield). Figure 4.7 shows variation of F_{min} with k^s across two different values each of k^r and k^t. For each of these cases, a clear trend is shown where smaller k^s corresponds to a lower buckling force. The gradient grows steeper for smaller k^s, increasing in increments at locations that correspond to changes in the value of the buckling segment size K. F_min also falls with decreasing k^r and k^t, though the variation in k^t is less significant.

In order to observe the behaviour of shear band width K with the various inputs, a matrix of data is calculated. k^r and k^t are varied through values between 0.l to 0.5 in increments of 0.05. k^s varies in increments of 0.005 from 0.005 to 0.05. By setting values of F_{min} for adjacent valid K equal to one another, regions can be defined within which K takes a certain value. A contour plot of this data is shown in Figure 4.8.

It should be observed that in general, K increases as k^s falls. The contours also fall closer together with increasing K and decreasing k^s. Increases in k^r and k^t also lead to higher K - hence for a long buckling segment, k^s should be low and k^r, k^t high.

It should be noted that, by its nature, K is quantised by the available failure modes and the requirement for buckling segments to contain a whole number of clusters. In the above analysis, this is then further constrained by the allowed buckling modes within a force chain of the length we have
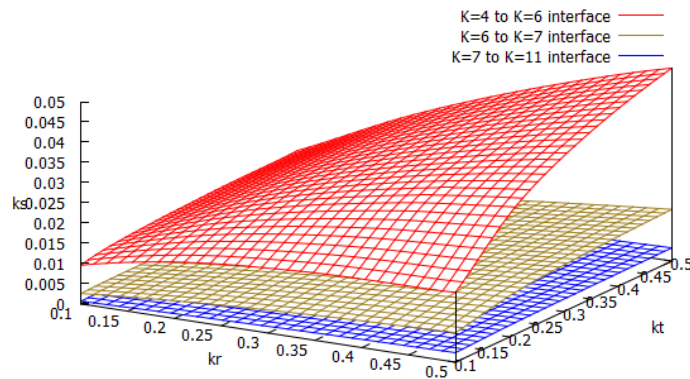
Figure 4.8: Contours outlining regions defined by buckling segment length, plotted in spring constant space.

selected. In a real system, force chains are unlikely to all neatly have the same length, so precise buckling modes and yield strengths will vary. As such, the distinction between buckling segment length regions will not follow the distinct contours shown above, and will not be constrained to a specific subset of allowed integers defined by a fixed chain length. Instead, the segment length will form a spectrum about an average value. Nonetheless, the above analysis can still carry useful information as to where this spectrum might lie and what trends it displays with variation in the inputs.

4.4.2 Dilatancy

Having determined the buckling behaviour of a single force chain, the dilatant behaviour of an array can now be considered. For these purposes, an array of $M = 30$ parallel force chains is considered, so as to give a shear band angle β in the vicinity of $\pi/4$ (although as buckling segment size K increases this angle will grow slightly more shallow).

Before buckling, the only influence on the volume of the assembly will be the effect of axial compression. The analysis above can be used to determine the critical force $F_{m}in$ required for buckling. This leads to a critical strain at which buckling begins:

113

$$\epsilon_1^{crit} = \frac{F_{min}}{2Rk_n} \tag{4.32}$$

Post buckling, it is assumed that further strain in the 1-direction is entirely accommodated by buckling - the effects of axial particle compression against k^n being negligible compared to the buckling effects. This allows Δ_b to be expressed as $\Delta - \Delta_{crit}$, where Δ_{crit} is the axial shortening at the onset of buckling. From the definition of strain:

$$\Delta = \epsilon_1(2RN) \tag{4.33}$$

via the $F = kx$ definition of a Hookean spring constant, applied over N+1 springs to make up the compressed portion of the force chain, Δ_{crit} can be found:

$$\Delta_{crit} = \frac{(N + 1)F_{min}}{k_n} \tag{4.34}$$

From the above Δ_b can therefore be expressed in terms of ϵ_1. Substituting into Equation 4.30, an expression for ϵ_2 in terms of ϵ_1 can be found.

$$\epsilon_2 = \sqrt{\frac{4\Delta_b}{DRM^2}} = \sqrt{\frac{4(\Delta - \Delta_{crit})}{DRM^2}} = \sqrt{\frac{4(\epsilon_1(2RN) - \frac{F(N+1)}{k_n})}{DRM^2}} \tag{4.35}$$

This is then calculated, using the Mathematica code found in Appendix B. Spring constants k_r and k_t are kept constant, with k_s being varied across a range chosen such that several values of buckling segment length K are sampled several times each.

Figure 4.9 shows a number of approaches to plotting the calculated data. Figure 4.9a simply plots $\epsilon_1 + \epsilon_2$ against ϵ_1. Figure 4.9b shows ϵ_2 against ϵ_1 - since the influence of ϵ_1 is simply linear with itself. Figure 4.9 c also cuts off the region prior to buckling, hence more effectively comparing post-buckling behaviour.

It is worth observing that the point of initial failure is entirely determined by F_{min} - as might be expected from the expression for ϵ_{crit} found in Equation 4.32. Hence in the cases shown in Figure 4.9 a and b, as k^s rises, F_{min} rises and hence yield occurs at higher axial strain.

The failure post-buckling appears to be entirely determined by the buckling segment length K. This is consistent with the analytical expression (Equation 4.35) - the purpose of the Δ_{crit} term
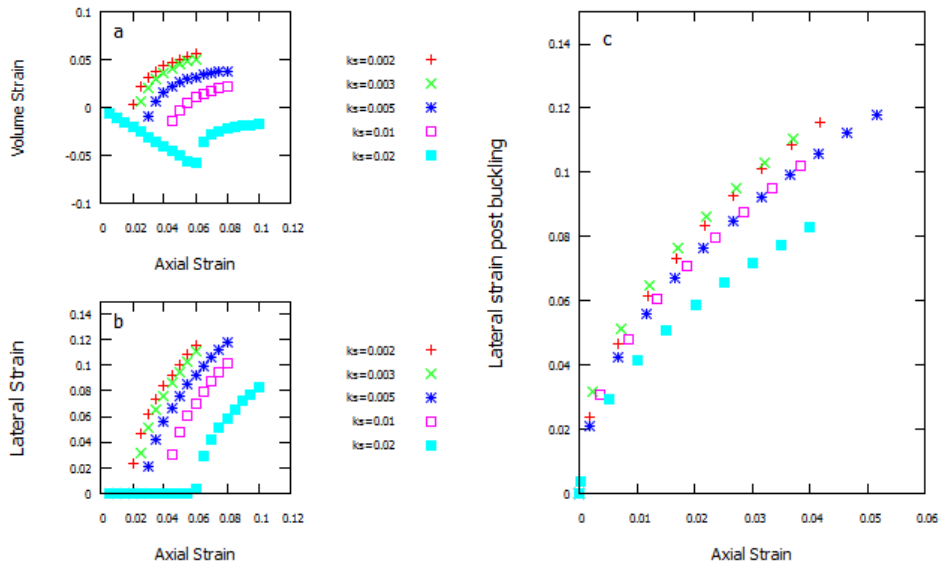
Figure 4.9: Dilatancy data against axial strain applied for varied input k_s. Shown a) volume strain raw data, b) lateral strain only, and c) lateral strain compared from the point of buckling onwards.

(which is dependent on F_{min}) is to ensure that ϵ_2 is 0 at $\epsilon_1 = \epsilon_{crit}$. Behaviour after that point is determined entirely by the Δ_b term, which is dependent on K through D.

The above plot can be considered more analytically by examining in detail Equation 4.30. The term controlling change in ϵ_2 with K is essentially driven by ϵ_1/D, which falls inside a square root term. D is plotted in Figure 4.10, along with $1/D$, and $\sqrt{1/D}$.

The ϵ_1 term (falling inside a square root) makes it clear that the post-buckling lateral deformation will always take the same square root shape with respect to further axial motion. Its magnitude will be controlled by D, and this will increase with K - so a higher K, ie a longer buckling segment, will always cause the system to dilate more. Variation of K with the spring constant inputs is considered above in Section 4.4.1.
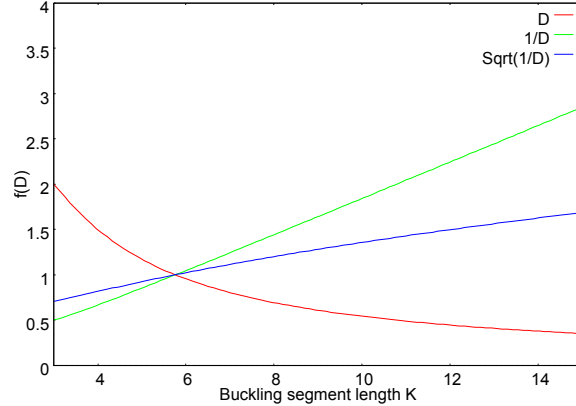
Figure 4.10: D, 1/D and Sqrt(1/D) plotted against buckling segment length K.
Note the linear nature of 1/D.

4.5 Discussion

So far, some key behaviours of the model have been identified but these have yet to be related to the properties of real systems. The following discussion will hence consider what can be learned about real behaviours, and whether the model can bring any light to observed properties of metallic glassy systems.

The model centres around yield and dilatant behaviour, and so it fits most naturally when applied to the onset and propagation of shear banding. The question is - can it draw any useful conclusions about how metallic glasses deform?

The typical narrative used to explain shear banding in metallic glasses is that shear transformation zones activate and dilate the local structure, making it easier for further STZs to activate and leading to self-catalysing shear banding.

The main inputs for the model that have been varied are the spring constants - both for axial compression (k_n), and then for lateral support (k_s) and rolling and sliding resistances (k_r and k_t). What might these be able to be related to in a real system? Quantitatively expressing these spring constants as functions of bulk mechanical properties is extremely difficult. However, relating them more qualitatively to such properties and tracking their variation may still carry significant information on behaviour.

Consider relating the lateral support spring constant k_n to the bulk modulus B, and the sliding

and rotation constants k_t and k_r to the shear modulus G. These make intuitive sense - a large bulk modulus makes expanding against the support network difficult, and a large shear modulus makes rotation and sliding of clusters against one another difficult.

This assertion can be supported by considering the electronic basis of the elastic moduli. In the force chain model, it is the inter-cluster bonding that will determine the properties of the system and hence the spring constants. The clusters themselves are treated essentially as hard spheres. This is backed up by the literature - see the work of Ma [29] and Wang et al [180] on the elastic properties of bulk metallic glasses being primarily determined by the solvent-solvent bonds. (Wang in fact even outright mentions treating the system as a series of springs [181]) The bulk modulus, which is rotationally invariant, is based on the compression response of the valence electrons involved in bonding. It essentially relates to the force required to change interatomic distances. The parallel to k_s is hence obvious - the lateral support network will indeed be controlled by the resistance of interatomic bonds to compression or stretching.

The shear modulus is instead based upon the resistance of these interatomic bonds to bending or distortion [83] [84], and is not rotationally invariant. It is immediately clear that resistance to bending and distortion of intercluster bonds should control the sliding and rotation of clusters against one another and hence k_t and k_r. Can this set of loose relations be used to draw light upon the deformation behaviour?

Take the initial point of buckling - a force chain or small assembly of force chains buckling under applied load. It is clear from the above model that this carries an associated dilatant effect - the magnitude thereof controlled by K and hence the spring constants (related to G and B).

This dilatant behaviour will have an impact on the local properties of the material. It is well established that elastic moduli change with local pressure or indeed density change - see the work of Wang et al [58] [59]. As the system dilates, the elastic constants G and B will fall. Therefore, the spring constants k_s, k_r and k_t will also be reduced in the local region.

Observing Figure 4.7, it can be seen that a fall in all 3 spring constants will lead to a fall in the force F_{min} required for buckling - i.e., it will be easier to buckle force chains in this region in future. This then provides a route to link the output of the model to shear banding behaviour. As buckling events occur, they influence the local elastic constants and make it easier for further buckling events

to occur in the same region. If the magnitude of this effect is significant or several buckling events are closely co-located, it will be significantly more favourable to activate further buckling events in the local region than to buckle at other weak spots elsewhere in the structure. This leads to the region dilating further, and self-catalysing behaviour leads to dilatant shear banding. As such, the model output is consistent with the traditional explanation for shear banding in metallic glasses.

Of significant note here is the tendency in the buckling force data for the fall in buckling force to accelerate as spring constants fall (see Figure 4.7). Decreasing elastic moduli will lead to more and more rapid decrease in the force required for buckling.

The effect of the initial spring constants (and hence elastic moduli) of the glass can also be considered. Consulting Figure 4.8, the observation can be made that the buckling segment length K increases with a fall in k_s and decreases with a fall in k_r or k_t. As such, it can be suggested that buckling segment length is related to the ratio of spring constants, and hence to the ratio of elastic moduli G and B. A high G/B is associated with relatively low k_s, high k_r and k_t, and hence long buckling segment length K. Conversely, a low G/B will be associated with short K.

Via Figures 4.9 and 4.10 and the associated analysis, it can be seen that K is the primary factor controlling the degree of dilatant behaviour observed on buckling. A high K - corresponding to high G/B - will lead to significant volume creation from each buckling event. A low K (low G/B) by comparison will result in a system that undergoes far less dilation when undergoing buckling.

From the analysis above, it is this volume creation during buckling that drives a reduction in local spring constants and hence the force required for further buckling. Dilatant behaviour drives shear banding, so less dilatant behaviour will result in a lower propensity for shear bands to propagate. In a system with low G/B, it will take longer for dilatant effects to build up and change the local properties enough to catalyse failure. This narrative hence gives a qualitative explanation, based in the output of the force chain buckling model, for the experimentally observed behaviour of metallic glasses in which glasses with low G/B display ductile behaviour and those with higher G/B are typically brittle.

Further correlations with established metallic glass theory can be observed when considering the energetics of the system. It can trivially be observed that the energy required to initiate buckling is directly proportional to F_{min} - hence falling with a fall in any of the spring constants k_s, k_t or k_r.

The critical buckling energy can be considered to relate to an STZ activation energy, or alternatively to the energy barrier for β relaxation (the two being closely related [41]). As such, regions within the metallic glass that have lower density (and hence lower elastic moduli and spring constants) will have a lower activation energy for small structural rearrangements via localised buckling.

This is relevant to the concept of 'free volume', which as per Egami [37] can also be viewed as local density fluctuation. A structure containing significant free volume will have regions of lower density surrounded by higher-density regions (the 'core-shell' model, see for example Ye et al [165]). In these lower-density regions, local rearrangements are made easier. However, the surrounding denser regions may prove more resistant to dilatation and hence shear band propagation is impaired, resulting in the potential for deformation being accommodated by lots of small local buckling events spread through the structure.

Volume strain associated with a buckling event is larger in high G/B systems according to the force chain model. The ductile-brittle transition can hence be seen as a competition between the inherent variation in elastic constants in the structure (the 'free volume', density variation carrying associated local fluctuations in spring constants) and the changes induced by buckling events. A larger G/B leads to deformation-induced volume strain rapidly dwarfing the prior structural effects and strain is localised into a single shear band. A smaller G/B sees the effect of buckling insufficient to localise yield completely, and when a more dense region is reached failure is re-initiated elsewhere at another low-density region. This gives distributed deformation and hence a degree of ductility.

The above can also be considered rather qualitatively in terms of energy landscapes. For a system with low G/B - ie tending toward short buckling segments, but also correlated with fragility [87], lots of potential small-scale rearrangements are available, with chains able to buckle at many different positions each carrying a small amount of associated deformation. This leads to lots of small basins with easy hopping from one to the other - very much the energy landscape associated with a fragile glass-former. On the other hand, a higher G/B case with longer K will have far fewer available rearrangements, each carrying a larger associated deformation - this can be related to the energy landscape of a strong glass-former with fewer deeper basins.

The force chain buckling model fits very closely with the work of Liss et al [168], which can be viewed as providing a degree of experimental verification. In-situ high-energy X-ray diffraction was used to gain insight into the behaviour of a Zr-based metallic glass under compression. Examining their results, the observation of continuing axial compression during the deformation process combined with significant transverse creation of free volume between clusters is exactly what one would expect in a buckling granular material. On yield, axial strain saturates while transverse strain runs away nonlinearly. They further observe that nearest-neighbour interactions remain similar - free volume is created on the cluster scale, which supports the model of the cluster as the deformation unit.

As well as providing experimental support for the force chain buckling model, a lot of the language used is very reminiscent of the arguments used here - albeit with no explicit mention of the granular comparison. Yield at weak points leads to transverse strain and creation of free volume that influences the local elastic moduli, moving the system toward a more liquidlike character that will eventually fail where Poisson's ratio reaches 0.5 and the ability to support shear entirely disappears. (The idea of shear as mechanical melting also appears in the review of Greaves et al [182]).

It should be noted that in the granular model an increasing Poisson's ratio would reduce K and hence volume strain - but by this point the damage is done, the local region is already significantly dilated and still the favoured location for buckling.

For a different example of the model matching established behaviour, consider the directionality of bonding in metallic glasses. It is established that metallic glasses with more non-directional bonds (as evidenced by positive deviation from zero Cauchy pressure) are more ductile [90]. Directionality of bonding would appear to correlate well with k_r - rotation of clusters being more difficult when bonds are at their most directional. A high k_r - corresponding to strongly directional bonding - also by the model implies a likelihood of long buckling segments K and hence significant dilatation associated with each buckling event. This fits well with the established evidence, and provides a degree of explanation as to why the more directionally bonded glasses are more brittle.

4.5.1 Examples

To set the above in context, consider some example glasses from the metallic glass literature. A glass with high B and lower G is the $Pt_{58}Cu_{15}Ni_5P_{22}$ glass developed by Schroers and Johnson [82]. An example with very low G, B and high G/B can be found in $Ce_{70}Al_{10}Ni_{10}Cu_{10}$ [63] [81] [7]. The $Fe_{50}Mn_{10}Mo_{14}Cr_4C_{16}B_6$ glass has similar B to the Pt-based glass but with notably higher G. Properties for these glasses can be found in Table 4.1.

Consider first the Pt-based glass. Examining its elastic constants, G is a fairly unexceptional 33.3 GPa, while B is a massive 198.7 GPa. Considering these in terms of model inputs, this should correspond to middle-of-the-road values for k_r and k_t, and a very high k_s - ie very significant lateral forces acting against buckling, while rotation and sliding of particles against one another are no more difficult than usual. The low G/B and hence k_r and k_t as compared to k_s will lead to a very short buckling segment K, with the associated volume strain hence also being small. As such, dilatation would accumulate slowly during shear, significantly impeding propagation of shear bands. This would result in a tough glass. Sure enough, this is borne out in the experimental data - with a large fracture energy indicating excellent toughness.

Taking a look at the Ce-based glass, G and B are both significantly lower than for the Pt-based glass, corresponding to significantly lower spring constants all round. Buckling should occur more readily and require lower energy to activate. The ratio of G to B, and hence of k_r and k_t to k_s, is significantly higher. This by the force chain buckling model implies a longer buckling segment K and a higher volume strain associated with buckling events. Therefore, shear band propagation should be easy. While buckling is initiated easily, regions in which buckling does occur rapidly hit runaway behaviour, reducing the opportunity for formation of multiple shear bands to distribute deformation. A check of the fracture behaviour confirms the prediction - the glass is brittle, with a low fracture energy.

The $Fe_{50}Mn_{10}Mo_{14}Cr_4C_{16}B_6$ glass has a similar B, and hence presumably k_s, to the Pt-based glass above. However, it has a notably higher G - at 76.1 GPa more than twice as high in fact, implying a significantly larger k_r and k_t - significant resistance to sliding and rolling motions of clusters. Given these inputs, a long K and a brittle glass would be expected - this is is confirmed

Composition	G/GPa	B/GPa	E/GPa		G/B
$Pt_{58}Cu_{15}Ni_5P_{22}$	33.3	198.7	94.8		0.167
$Ce_{70}Al_{10}Ni_{10}Cu_{10}$	11.5	27	30.3		0.427
$Fe_{50}Mn_{10}Mo_{14}Cr_4C_{16}B_6$	76.1	180	200		0.423
Composition	ν	G_c / $\mathrm{J\,m^{-2}}$	K_c / $\mathrm{MPa\,m^{-1/2}}$		Ref
$Pt_{58}Cu_{15}Ni_5P_{22}$	0.42	90	84		[82]
$Ce_{70}Al_{10}Ni_{10}Cu_{10}$	0.313	3	10		[63]
$Fe_{50}Mn_{10}Mo_{14}Cr_4C_{16}B_6$	0.314	0.02	2		[81]

Table 4.1: Mechanical properties for some example glass compositions.

by the data, with a low fracture energy being observed, comparable to the cerium-based glass that has far lower elastic constants all round.

A note of caution - so far the model has not directly referenced that omnipresent theoretical construct in metallic glass science: the shear transformation zone, or STZ. The correspondence between STZ theory and this model is not direct. While a buckling segment may to a first impression resemble depictions of STZ, in practice the support network that provides k_s must also be taken into account, as must the remainder of the force chain. Buckling events do not only influence the particles involved in the segment that buckles, but also the surrounding material. Furthermore, force chains should not be seen as a static and immutable construct, present in the structure from the outset until buckled, then not considered further. In fact, force chains are dynamic constructs - they represent the load balance and local structure in the material at a very short timescale. Force chains can appear and disappear, can lengthen and shorten, can buckle once or several times - whether in the same or different locations - and will alter to reflect the state of local loading. The simplistic picture of a shear band as a series of parallel force chains each buckling once and only once is not a sufficient description, while it does prove very useful for giving a measure of dilatancy. In fact, a shear band may be made up of a collection of buckling events in the same way as STZ theory, and buckling segment length, while controlling dilatant behaviour, may not necessarily correspond

directly to shear band width or STZ size.

4.6   Conclusions

The first part of this work has been to take a model of collective force chain buckling developed for granular materials and consider where it might apply to shear banding in metallic glasses. It has been shown that the local elastic constants (represented by spring constants in the model, and corresponding loosely to G and B in the physical glass) control the mode of deformation. Low elastic constants in a local region lead to easy onset of buckling and hence yield. The ratio of these constants (approximating to G/B) controls the degree of volume strain associated with that yielding - a low G/B means a short buckling segment K, which carries less associated dilatant behaviour. Via the fall in local elastic constants associated with this volume change, the region around the buckled force chain now forms a potential nucleation site for further buckling events, and this provides for a mechanism to explain and describe shear banding in metallic glasses.

A metallic glass system will contain a degree of initial density fluctuation, with variation in local elastic constants being associated with these fluctuations. On the onset of buckling, which will likely occur at a low-density weak spot, the local area becomes more dilated and it is easier for further buckling to occur. What would appear therefore to control the ductile or brittle nature of the material is simply a competition between the magnitude of the local density fluctuations already in place, and the magnitude of the density change created upon buckling. In a system with significant initial fluctuation and little volume strain on buckling, the nascent shear band will not become a more attractive place to nucleate buckling events than other weak spots in the structure. In a system with few of these initial deformation-favourable sites and more volume strain associated with buckling, there is nowhere else for deformation to be accommodated and the shear band rapidly becomes by far the easiest location to deform, leading to catastrophic failure by runaway propagation. It should be noted that the above can provide a plausible explanation for the unusually sharp ductile to brittle transition with G/B or ν in metallic glasses [81] - it represents the point at which deformation-induced dilatation outcompetes the local density fluctuations to act as the site for further yield, or vice versa.

The above is to an extent an extrapolation and reframing of concepts already found in the literature - what the force chain model provides is a lens through which to examine the competition between pre-existing regions of low elastic moduli and the changes that occur around deforming regions. It forms the basis for an approach that might in future be used to more quantitatively predict whether deformation-created 'free volume' or its inherent-to-structure equivalent will win the competition to be the site for deformation, and hence whether yield will be distributed or localised, ductile or brittle.

What the model also provides is an opportunity to set metallic glasses in a broader context. Metallic glasses can be seen as a special case of a granular material, in much the same way as Gourlay's work [2] linking semi-solidified metals with such systems. The systems are distinguished by their length scales and the nature of the forces controlling their behaviour. In a traditional granular material such as sand, the 'particles' are in fact individual grains. Lateral support will depend on the nature of the packing, and the resistance to rotation and sliding (and hence shear) will be frictional terms driven by the irregular shape of grains. In a semi-solid slurry, viscous forces will be more important than frictional. Going down to the length scale of the metallic glass, it is the electronic nature of interatomic and intercluster bonding that determines behaviour. Nonetheless, taking these differences into account the systems display very similar behaviour and respond to deformation in very much the same way - hence the same mathematics being useable to describe their behaviour.

It should be noted that metallic glasses do have a significant structural cohesion that sands do not - the forces connecting adjacent particles can be attractive as well as repulsive. This means that perhaps a better comparison than a sand might in fact be a clay - but in any case, under compression much the same behaviour is observed, and this work sets the stage for potential further investigations into the similarities - and differences - between metallic glasses and larger-scale granular media.

Looking back to the literature, perhaps what this work has achieved is to present a new set of order parameters that can be used to describe the state of a metallic glass. There evidently already exist a number of previously understood order parameters, each with their own distinct advantages and associated way of looking at a glass. The fictive temperature, for example, looks at the glass

from the perspective of a liquid, and is useful in linking deformation behaviour of glasses to their processing history and glass forming behaviour. Elastic moduli, by comparison, have the advantage of being easily measurable and hence linking the system back to observable behaviours. This also makes them useful for material selection. However, they have only loosely been linked to the bonding and packing state of the actual glass at the microscale, and the relation between them and shear banding behaviour is still only expressed somewhat qualitatively. They tend to lean toward our seeing the glasses from a crystalline perspective. Looking at the energy landscape is useful for the modeller and keeps the system close to the actual physical goings on, but is hard to relate to measurable properties - it tends to suit the solid-state physicist's eye.

The new order parameter - expressed as a series of spring constants - is closely linked to the state of the local bonding and packing in the material, but not as closely as the energy landscape picture. What it provides that other order parameters do not is the beginnings of a way to link the state of structural order quantitatively rather than qualitatively to the dilatant behaviour of STZs and shear bands. A lot of work remains to do yet, but the new parameter offers the hope of a more detailed link between the state of the glass and the development of shear bands. It forms, perhaps, one step of the link between the energy landscape at the most theoretical and the elastic moduli at the most practical end of the order parameter scale. It also draws on a new perspective - that of granular materials. It opens up the possibility of looking at metallic glass as just a special case of a granular material, which carries the significant advantage that the packing and behaviour of granular media can be much more easily described mathematically and hence new quantitative insight into deformation behaviour may be possible.

4.6.1 Further Work

While the force chain buckling model fits closely with the observed behaviour of metallic glassy systems even in its current form, it is far from without problems. The model makes some very significant assumptions that are simply not true in real systems.

The first of these is that of perfectly aligned 2D force chains without predetermined weak points. In practice, force chains (in 3D) will be far from perfectly straight and failure is likely to initiate at

weak spots in the structure.

Failure at weak points does not change the overall argument - that force chain buckling is dependent on the relative values of the spring constants resisting motion, and that this can carry information relating bulk to local properties. The presence of weak spots will make initial buckling events easier, but even so, glasses with higher G and lower B will still find these buckling events on average producing more dilatation. This will still lead to a reduction in spring constants locally and hence a reduction in the force required for buckling, self-catalysing to form shear bands and hence leading to brittle failure.

The presence of weak spots is also taken into account in the 'free volume' (density fluctuation) argument - regions with low density preferentially undergoing buckling but not necessarily developing into shear bands. It would nonetheless be interesting to develop the model itself to take into account non-idealised behaviour. This could bring the model closer to a fully quantitative description of STZ activation and yield.

The second issue is the lack of a direct quantitative link between the spring constants k and experimentally measurable properties. The lack of this link renders the output of the model, while very informative on a qualitative basis, short on detailed predictive power. It is clear that they represent the nature of intercluster bonding, and by extension connect to the elastic moduli of the system, but a quantitative relationship has yet to be established and hence remains an outstanding challenge. What the work so far provides is to an extent a 'proof of concept' and a general overview of expected behaviour; it is likely that a detailed investigation into the interatomic bonding will be necessary to determine the spring constants more exactly.

Chapter 5

Concluding Statements

At the start of this work, the objective was to investigate and shed some new light on the behaviour of transformation toughening metallic glass matrix composites, such as those developed by Eckert's group in Dresden [1]. A realisation that rapidly came to light when investigating those materials was that the literature regularly compared them to traditional transformation toughening materlials, including suggesting the volume change associated with martensitic transformation as a toughening mechanism. However, the volume change associated with the martensitic transformation in equiatomic Cu-Zr (the system most often studied) is very very small. This then led to the suspicion that this mechanism might not in fact be valid - though several other potentially viable mechanisms remain.

In order to confirm this, a comparison was drawn with transformation toughening in ceramics. A body of work carried out by McMeeking and Evans [123] was selected to provide the basis for the toughening calculation. Their work identifies a transformation radius and then, using the weight function theory of Bueckner, Rice and Paris, determines the effect of transformation on the stress intensity factor at the crack (or, here, shear band) tip. The calculations needed adapting - McMeeking and Evans had considered Mode I cracking, where Mode II is more appropriate for a shear band. Calculations were carried out initially for the volume term only. However, the transformation still carries a significant shear term, and so a method was developed to give some degree of estimate as to the effects of the shear component of transformation, using a few sample

transformation orientations to give a qualitative picture of the possible effects.

It was found that the volume change alone cannot possibly be impacting the stress state at the shear band tip, the effect being far too small in magnitude. When considering the shear term, it must be noted that typically variant self-accommodation massively reduces this in practice (multiple variants or sets of twins are indeed observed experimentally). Discounting that to give a limiting case, for a given transformation orientation a noteworthy effect is observed - but the orientation is important, and should the direction of transformation be randomly oriented the effects would cancel out.

This negative result left the investigation rather lacking in obvious direction, and so casting around for insight into other possible toughening mechanisms began. At this point, while looking deeper into the general shear banding behaviour of metallic glasses, it was observed that granular materials undergo very similar behaviour to metallic glasses. The question therefore arose as to whether models used to describe shear banding in granular media might be adapted to metallic glasses, in the same way as fracture mechanics models from ceramics had been adapted to transformation toughening in the same glasses.

A model rapidly drew attention to itself as showing strong potential - the force chain buckling model of Tordesillas et al [3] [4]. The model viewed the granular (or here metallic glass) system under stress as a network of contacts ('force chains') under stress, supported loosely by a surrounding network of less stressed particles. Their computational model had shown behaviour on buckling of these chains that was very reminiscent of STZ action, and their mathematical model promised the potential of a stress-dilatancy relation; a link between local properties and the dilatant effect of deformation.

Working through the model, a range of sample data was calculated with which to observe the effect of the local properties - modelled as a series of spring constants - on yield and dilatant behaviour. It was observed that a fall in the spring constants would, predictably, lead to more rapid onset of yield. Of greater interest, though, was the output concerning the associated volume strain. The three spring constants that had been varied as inputs concerned resistance to sliding and rotation of particles (modelled as clusters) against one another, and the lateral support from nearby particles on the force chain. A high lateral support, or a low resistance to sliding and rolling, tended to lead

to a buckling segment consisting of very few particles - and vice versa. What was particularly key was that the length of the buckling segment controlled the volume strain associated with a given amount of axial deformation. Linking these spring constants to elastic moduli - the rotation and sliding resistances to the shear modulus G, and the lateral support to the bulk modulus B - the result emerged that a glass with a high G and a low B would exhibit a long buckling segment and lots of dilatation when it deformed. A link was drawn between this dilatant behaviour and an associated fall in the local spring constants, making the system yield more easily in that local region in future.

Deformation carries an associated dilatant effect, with its magnitude related to the local G/B. Shear banding and failure exist to an extent as a competition between the reduction in local spring constants (bonding and packing, or elastic moduli - choose your order parameter to taste) caused by buckling events and the inherent degree of variation in these constants present in the structure. If, when the shear band hits a more ordered region, there are other parts of the structure with low spring constants and easy yield then buckling will occur there instead. If instead the system is fairly homogeneous but buckling creates a lot of volume strain, then a single catastrophic shear band will lead to brittle failure.

What had been achieved was to develop a new order parameter for glasses, based on these spring constants. The new order parameter is not as grounded in the physics of the local bonding as the energy landscape arguments, nor as easily related to measurable properties as the local elastic moduli. What it does, however, provide is the potential for a more quantitative link between deformation and dilatation. Much more investigation is required, but this new parameter and approach might begin to bridge the gap between the scales of bonding and atomic packing, and measurable mechanical responses.

Looking back to the beginning, the new approach might even be applicable to transformation toughening. On transformation and twinning, particles in and around the shear band might constrain the support network resisting lateral motion of force chains, and hence make buckling more difficult. This would reduce the accumulation of disorder in the shear band and impede its propagation. Similarly, a region around a particle-matrix interface that had been disrupted by the transformation strain might serve as a preferential site for buckling, initiating secondary shear bands and hence ensuring strain was distributed throughout the structure.

Perhaps a final lesson to draw would be this - there are a lot of types of material out there, and a lot of them bear similarities to one another. With a bit of searching around and some lateral thinking, ideas that help understand one of them may be adapted to improve the understanding of others. Here, metallic glasses have been compared to ceramics, and to granular media - perhaps more insight can be found in those fields to help us in our own specialty. Perhaps even in the future, and in fact as some have already begun to contemplate [146], metallic glasses may one day have something to teach the more established materials sciences as well.

Bibliography

[1] J Das, K B Kim, W Xu, B C Wei, Z F Zhang, W H Wang, S Yi, and J Eckert. Ductile metallic glasses in supercooled martensitic alloys. *Materials Transactions*, 47(10):2606--2609, 2006.

[2] C Gourlay and A Dahle. Dilatant shear bands in solidifying materials. *Nature*, 445:70--73, 2007.

[3] A Tordesillas, J Shi, and T Tshaikiwsky. Stress dilatancy and force chain evolution. *International Journal for Numerical and Analytical Methods in Geomechanics*, 35:264--292, 2011.

[4] G Hunt, A Tordesillas, S Green, and J Shi. Force-chain buckling in granular media: a structural mechanics perspective. *Philosophical Transactions of the Royal Society A*, 368:249--262, 2010.

[5] W Klement, RH Willens, and P Duwez. Non-crystalline structure in solidified gold–silicon alloys. *Nature*, 187:869--870, 1960.

[6] S Kavesh, J J Gillman, and H L Leamy. *Metallic Glasses*. ASM International, Metals Park, OH, 1978.

[7] W H Wang, C Dong, and C H Shek. Bulk metallic glasses. *Materials Science and Engineering R*, 44:45--89, 2004.

[8] D Turnbull. Under what conditions can a glass be formed. *Contemporary Physics*, 10(5):473--488, 1969.

[9] H S Chen. Thermodynamic considerations on the formation and stability of metallic glasses. *Acta Metallurgica*, 22:1505--1511, 1974.

[10] A Inoue, T Zhang, and T Masumoto. Al-La-Ni amorphous alloys with a wide supercooled liquid region. *JIM*, 30(12):965--972, 1989.

[11] A Inoue, K Ikegami, T Koshiba, and T Nagata. Cobalt-based bulk glassy alloy with ultrahigh strength and soft magnetic properties. *Nature Materials*, 2(10):661--663, 2003.

[12] J Scully, A Gebert, and J Payer. Corrosion and related mechanical properties of bulk metallic glasses. *Journal of Materials Research*, 22(2):302--313, 2007.

[13] R O'Handley, R Hasegawa, R Ray, and C Chou. Ferromagnetic properties of some new metallic glasses. *Applied Physics Letters*, 29:330--332, 1976.

[14] W Wang, M Pan, D Zhao, Y Hu, and H Bai. Enhancement of the soft magnetic properties of FeCoZrMoWB bulk metallic glass by microalloying. *Journal of Physics: Condensed Matter*, 16:3719--3723, 2004.

[15] C Lin, H Tien, and T Chin. Soft magnetic ternary iron-boron-based bulk metallic glasses. *Applied Physics Letters*, 86:162501 1--3, 2005.

[16] M Telford. The case for bulk metallic glass. *Materials Today*, 7(3):36--43, 2004.

[17] C Prest, J Poole, J Stevick, T Waniuk, and Q Pham. Bulk amorphous alloy sheet forming processes. Patent 8485245, July 2013.

[18] B Howald. `http://www.swatchgroup.com/en/services/archive/2011/swatch_group_signs_exclusive_license_agreement_with_liquidmetal_technologies`, 2011. Online, accessed 2013.

[19] Daniel B Miracle. A structural model for metallic glasses. *Nature Materials*, 3(October 2004):697--702, 2004.

[20] H W Sheng, W K Luo, F M Alamgir, J M Bai, and E Ma. Atomic packing and short-to-medium-range order in metallic glasses. *Nature*, 439:419--425, 2006.

[21] Jeppe C Dyre. Colloquium: The glass transition and elastic models of glass-forming liquids. *Reviews of Modern Physics*, 78(July-September):953--971, 2006.

[22] C A Angell. Formation of glasses from liquids and biopolymers. *Science,* 267, 1995.

[23] C A Angell. Spectroscopy simulation and scattering, and the medium range order problem in glass. *Journal of Non-Crystalline Solids*, 73:1--17, 1985.

[24] J C Maxwell. On the dynamical theory of gases. *Philosophical Transactions of the Royal Society of London*, 157:49--88, 1867.

[25] A Inoue. Stabilization of metallic supercooled liquid and bulk amorphous alloys. *Acta Materialia*, 48(1):279--306, 2000.

[26] V. Kokotin and H. Hermann. Geometrical aspects of the glass -forming ability of dense binary hard-sphere mixtures. *Scripta Materialia*, 61:261--264, 2009.

[27] S Ding, J Gregoire, J Vlassak, and J Schroers. Solidification of Au-Cu-Si alloys investigated by a combinatorial approach. *Journal of Applied Physics*, 111(11), 2012.

[28] W Wang, Q Wei, and S Friedrich. Microstructure, decomposition and crystallization in $Zr_{41}Ti_{14}Cu_{13}Ni_{10}Be_{22}$ bulk metallic glass. *Physical Review B*, 57(14):8211--8217, 1998.

[29] D Ma, A Stoica, X Wang, Z Lu, B Clausen, and D Brown. Elastic moduli inheritance and the weakest link in bulk metallic glasses. *Physical Review Letters*, 108:085501, 2012.

[30] W Brostow and J Dussault. Construction of Voronoi polyhedra. *Journal of Computational Physics*, 29(1):81--82, 1978.

[31] University of North Carolina. `http://www.unc.edu/~ivaisman/delaunay/tessell.htm`. Online, accessed January 2014.

[32] W Wang, R Wang, D Zhao, M Pan, and Y Yao. Microstructural transformation in a $Zr_{41}Ti_{14}Cu_{13}Ni_{10}Be_{22}$ bulk metallic glass under high pressure. *Physical Review B*, 62(17):292--295, 2000.

[33] K Flores, D Suh, R Dauskardt, P Asoka-Kumar, P Sterne, and R Howell. Characterization of free volume in a bulk metallic glass using positron annihilation spectroscopy. *Journal of Materials Research*, 17(5):1153--1161, 2002.

[34] Frans Spaepen. A microscopic mechanism for steady state inhomogeneous flow in metallic glasses. *Acta Metallurgica*, 25(4):407--415, 1977.

[35] A van den Beukel and J Sietsma. The glass transition as a free volume related kinetic phenomenon. *Acta Metallurgica et Materialia*, 38(3):383--389, 1990.

[36] C Nagel, K Rätzke, E Schmidtke, J Wolff, U Geyer, and F Faupel. Free-volume changes in the bulk metallic glass $Zr_{46.7}Ti_{8.3}Cu_{7.5}Ni_{10}Be_{27.5}$ and the undercooled liquid. *Physical Review B*, 57(17):10224--10227, 1998.

[37] T Egami. Understanding the properties and structure of metallic glasses at the atomic level. *Journal of Materials*, 62(2):70--75, 2010.

[38] P Debenedetti and F Stillinger. Supercooled liquids and the glass transition. *Nature*, 410:259--267, 2001.

[39] D Malandro and D Lacks. Volume dependence of potential energy landscapes in glasses. *Journal of Chemical Physics*, 107(15), 1997.

[40] J Harmon, M Demetriou, W Johnson, and K Samwer. Anelastic to plastic transition in metallic glass-forming liquids. *Physical Review Letters*, 99:135502, 2007.

[41] H Yu, W Wang, H Bai, Y Wu, and M Chen. Relating activation of shear transformation zones to β relaxations in metallic glasses. *Physical Review B*, 81:220201, 2010.

[42] D Bedorf and K Samwer. Length scale effects on relaxations in metallic glasses. *Journal of Non-Crystalline Solids*, 356(6-8):340--343, 2010.

[43] H Teichler. Heterogeneous dynamics on the microsecond scale in simulated $Ni_{0.5}Zr_{0.5}$ metallic melts far below the glass temperature. *Physical Review E*, 71:031505, 2005.

[44] C A Schuh, T C Hufnagel, and U Ramamurty. Mechanical behaviour of amorphous alloys. *Acta Materialia*, 55:4067--4109, 2007.

[45] E S Park, J S Kyeong, and D H Kim. Phase separation and improved plasticity by modulated heterogeneity in Cu - (Zr,Hf) - (Y,Gd) - Al metallic glasses. *Scripta Materialia*, 57:49--52, 2007.

[46] J J Lewandowski and A L Greer. Temperature rise at shear bands in metallic glasses. *Nature Materials*, 15(1), 2006.

[47] H J Leamy, T T Wang, and H S Chen. Plastic flow and fracture of metallic glass. *Metallurgical Transactions*, 3(3):699--708, 1972.

[48] Y Zhang and A L Greer. Thickness of shear bands in metallic glasses. *Applied Physics Letters*, 89(7), 2006.

[49] Alexei Vinogradov. On shear band velocity and the detectability of acoustic emission in metallic glasses. *Scripta Materialia*, 63:89--92, 2010.

[50] R Cahn, N Pratten, M Scott, H Sinning, and L Leonardsson. Studies of relaxation of metallic glasses by dilatometry and density measurements. *MRS Proceedings*, 28, 1 1983.

[51] P Donovan and W Stobbs. The structure of shear bands in metallic glasses. *Acta Metallurgica*, 29(8):1419--1434, 1981.

[52] Y Waseda and T Egami. Effect of low-temperature annealing and deformation on the structure of metallic glasses by X-ray diffraction. *Journal of Materials Science*, 14:1249--1253, 1979.

[53] Y Wu, H X Li, Z Y Liu, G L Chen, and Z P Lu. Interpreting size effects of bulk metallic glasses based on a size-independent critical energy density. *Intermetallics*, 18:157--160, 2010.

[54] C Q Chen, Y T Pei, and J T M De Hosson. Effects of size on the mechanical response of metallic glasses investigated through in situ tem bending and compression experiments. *Acta Materialia*, 2009.

[55] A S Argon and H Y Huo. Plastic flow in a disordered bubble raft (an analog of a metallic glass). *Materials Science and Engineering*, 39(1):101--109, 1979.

[56] M Chen. Mechanical behaviour of metallic glasses: microscopic understanding of strength and ductility. *Annual Review of Materials Research*, 38:445--469, 2008.

[57] E R Homer and C A Schuh. Mesoscale modelling of amorphous metals by shear transformation zone dynamics. *Acta Materialia*, 57:2823--2833, 2009.

[58] W Wang, R Wang, F Li, D Zhao, and M Pan. Elastic constants and their pressure dependence of $Zr_{41}Ti_{14}Cu_{13}Ni_0Be_{22}$ bulk metallic glass. *Applied Physics Letters*, 74(13):1803--1805, 1999.

[59] L Wang, L Sun, W Wang, R Wang, Z Zhan, D Dai, and W Wang. Elastic constants of $Pd_{39}Ni_{10}Cu_{30}P_{21}$ bulk metallic glass under high pressure. *Applied Physics Letters*, 77(23):3734--3736, 2000.

[60] A Cao, Y Cheng, and E Ma. Structural proceses that initiate shear localization in metallic glass. *Acta Materialia*, 57:5146--5155, 2009.

[61] E Koba, Y Milman, and A Rachek. Effect of plastic deformation and high pressure working on the structure and microhardness of metallic glasses. *Acta Metallurgica et Materialia*, 42(4):1383--1388, 1994.

[62] A Greer, Q Cheng, and E Ma. Shear bands in metallic glasses. *Materials Science and Engineering R*, 74:71--132, 2013.

[63] W Wang. The elastic properties, elastic models and elastic perspectives of metallic glasses. *Progress in Materials Science*, 2011.

[64] Y Liu, C Liu, W Wang, A Inoue, T Sakurai, and M Chen. Thermodynamic origins of shear band formation and the universal scaling law of metallic glass strength. *Physical Review Letters*, 103:066504, 2009.

[65] E Homer. *Modeling the mechanical behaviour of amorphous metals by shear transformation zone dynamics*. PhD thesis, Massachusetts Institute of Technology, 2010.

[66] T Fujita, Z Wang, Y Liu, H Sheng, W Wang, and M Chen. Low temperature uniform plastic deformation of metallic glasses during elastic iteration. *Acta Materialia*, 60:3741--3747, 2012.

[67] X Xi, D Zhao, M Pan, W Wang, Y Wu, and J Lewandowski. Fracture of brittle metallic glasses: Brittleness or plasticity. *Physical Review Letters*, 94:125510, 2005.

[68] J Meng, Z Ling, M Jiang, H Zhang, and L Dai. Dynamic fracture instability of tough bulk metallic glass. *Applied Physics Letters*, 92:171909 1--3, 2008.

[69] C Pampillo and A Reimschuessel. The fracture topography of metallic glasses. *Journal of Materials Science*, 9:718--724, 1974.

[70] A Argon and M Salama. The mechanism of fracture in glassy materials capable of some inelastic deformation. *Materials Science and Engineering*, 23:219--230, 1976.

[71] D Pan, H Zhang, A Wang, Z Wang, and Z Hu. Fracture instability in brittle Mg-based bulk metallic glasses. *Journal of Alloys and Compounds*, 438(1-2):145--149, 2007.

[72] C Liu, J Heatherly, A Horton, D Easton, C Carmichael, J Wright, M Schneibel, H Yoo, C Chen, and A Inoue. Test environments and mechanical properties of Zr-base bulk amorphous alloys. *Metallurgical and Materials Transactions A*, 29(7):1811--1820, 1998.

[73] A Lund and C Schuh. The mohr-coulomb criterion from unit shear processes in metallic glass. *Intermetallics*, 12(10-11):1159--1165, 2004.

[74] T Mukai, T Nieh, Y Kawamura, and A Inoue. Effect of strain rate on compressive behaviour of a $Pd_{40}Ni_{40}P_{20}$ bulk metallic glass. *Intermetallics*, 10(11-12):1071--1077, 2002.

[75] http://www.pisa.ab.ca/program/model/plastic/plastic.htm. Accessed December 2013.

[76] M Zhao and M Li. Interpreting the change in shear band inclination angle in metallic glasses. *Applied Physics Letters*, 93:241906, 2008.

[77] M D Demetriou, William L Johnson, and K Samwer. Coarse-grained description of localized inelastic deformation in amorphous metals. *Applied Physics Letters*, 94:191905, 2009.

[78] W H Wang. Correlations between elastic moduli and properties in bulk metallic glasses. *Journal of Applied Physics*, 99(9), 2006.

[79] Frans Spaepen and Wu Tsai-Wei. The relation between enbrittlement and structural relaxation of an amorphous metal. *Philosophical Magazine B*, 61(4):739--750, 1990.

[80] U Ramamurty, M Lee, J Basu, and Y Li. Embrittlement of a bulk metallic glass due to low-temperature annealing. *Scripta Materialia*, 47(2):107--111, 2002.

[81] J J Lewandowski, A L Greer, and W H Wang. Intrinsic plasticity or brittleness of metallic glasses. *Philosophical Magazine Letters*, 85(2):77--87, 2005.

[82] Jan Schroers and William L Johnson. Ductile bulk metallic glass. *Physical Review Letters*, 93:255506, 2004.

[83] T Courney. *Mechanical behaviour of materials*. McGraw-Hill Companies Inc., second edition, 2000.

[84] D Head, F MacKintosh, and A Levine. Nonuniversality of elastic exponents in random bond-bending networks. *Physical Review E*, 68, 2003.

[85] T Egami. Formation and deformation of metallic glasses: Atomistic theory. *Intermetallics*, 14(8-9):882--887, 2006.

[86] D Pan, A Inoue, T Sakurai, and M Chen. Experimental characterization of shear transformation zones for plastic flow of bulk metallic glasses. *PNAS*, 105(39):14769--14772, 2008.

[87] V Novikov and A Sokolov. Poisson's ratio and the fragility of glass-forming liquids. *Nature*, 431:961--963, 2004.

[88] W Johnson and K Samwer. A universal criterion for plastic yielding of metallic glasses with a $(T/T_g)^{2/3}$ temperature dependence. *Physical Review Letters*, 97:195501, 2005.

[89] J Plummer and I Todd. Implications of elastic constants, fragility, and bonding on permanent deformation in metallic glass. *Applied Physics Letters*, 98:021907, 2011.

[90] J Plummer and I Todd. Isomechanical groups in bulk metallic glasses. *Philosophical Magazine Letters*, 92(23), 2012.

[91] H Wagner, D Bedorf, S Kuchemann, M Schwabe, B Zhang, W Arnold, and K Samwer. Local elastic properties of a metallic glass. *Nature Materials*, 6:439--442, 2011.

[92] M Pham, K Park, B Yoo, J Jang, and J Lee. Plasticity improvement of amorphous alloy by skim cold rolling. *Metals and Materials International*, 15(2):209--214, 2009.

[93] M Lee, K Lee, J Das, J Thomas, U Kühn, and J Eckert. Improved plasticity of bulk metallic glasses upon cold rolling. *Scripta Materialia*, 62(9):678--681, 2010.

[94] S Scudino, B Jerliu, S Pauly, K Surreddi, U Kuhn, and J Eckert. Ductile bulk metallic glasses produced through designed heterogeneities. *Scripta Materialia*, 65:815--818, 2011.

[95] L He, M Zhong, Z Han, Q Zhao, F Jiang, and J Sun. Orientation effect of pre-introduced shear bands in a bulk-metallic glass on its 'work-ductilising'. *Materials Science and Engineering A*, 496:285--290, 2008.

[96] Y Zhang, W Wang, and A Greer. Making metallic glasses plastic by control of residual stress. *Nature Materials*, 5:857--860, 2006.

[97] S Lee, C Lee, J Yang, and J Lee. Microstructural evolution of an elastostatically compressed amorphous alloy and its influence on the mechanical properties. *Scripta Materialia*, 58(7):591--594, 2008.

[98] Y Chen, M Jiang, and L Dai. How does the initial free volume distribution affect shear band formation in metallic glass? *Science China: Physics ,Mechanics and Astronomy*, 54(8):1488--1494, 2011.

[99] C C Hays, C P Kim, and William L Johnson. Microstructure controlled shear band pattern formation and enhanced plasticity of bulk metallic glasses containing in situ formed ductile phase dendrite dispersions. *Physical Review Letters*, 84(13):2901--2904, 2000.

[100] A Inoue, W Zhang, T Tsurui, A R Yavari, and A L Greer. Unusual room-temperature compressive plasticitiy in nanocrystal-toughened bulk copper-zirconium glass. *Philosophical Magazine Letters*, 85(5):221--229, 2005.

[101] G He, W Loser, J Eckert, and L Schultz. Enhanced plasticity in a Ti-based bulk metallic glass-forming alloy by in situ formation of a composite microstructure. *Journal of Materials Research*, 17(12):3015--3018, 2002.

[102] S V Madge, P Sharma, D V Louzguine-Luzgin, A L Greer, and A Inoue. New la-based glass-crystal ex situ composites with enhanced toughness. *Scripta Materialia*, 62:210--213, 2010.

[103] H Choi-Yim and William L Johnson. Bulk metallic glass matrix composites. *Applied Physics Letters*, 71(26):3808--3810, 1997.

[104] R D Conner, R B Dandliker, and William L Johnson. Mechanical properties of tungsten and steel fiber reinforced $Zr_{41}Ti_{14}Cu_{13}Ni_{10}Be_{22}$ metallic glass matrix composites. *Acta Materialia*, 46(17):6089--6102, 1998.

[105] Y H Go, J Cho, C Y Jeong, C S Kang, and J S Park. Stress distribution of bulk metallic glass/metal laminate composites during uni-axial fracture. *Materials Science and Engineering A*, 460-461:377--382, 2007.

[106] Y Leng and T H Courtney. Some tensile properties of metal-metallic glass laminates, 1989.

[107] S Li, D V Louzguine-Luzgin, G Q Xie, M Sato, and A Inoue. Development of novel metallic glass/polymer composite materials by microwave heating in a separated H-field. *Materials Letters*, 64:235--238, 2010.

[108] U Kuhn, J Eckert, N Mattern, and L Schultz. ZrNbCuNiAl bulk metallic glass matrix composites containing dendritic bcc phase precipitates. *Applied Physics Letters*, 80(14):2478--2480, 2002.

[109] D Hofmann, J Suh, A Wiest, G Duan, M Lind, M Demetriou, and W Johnson. Designing metallic glass matrix composites with high toughness and tensile ductility. *Nature*, 451:1085--1089, 2008.

[110] J Eckert, U Kühn, N Mattern, G He, and A Gebert. Structural bulk metallic glasses with different length-scale of constituent phases. *Intermetallics*, 10(11-12):1183--1190, 2002.

[111] H Chen, Y He, G Shiflet, and S Poon. Deformation-induced nanocrystal formation in shear bands of amorphous alloys. *Nature*, 367:541--543, 1994.

[112] J Kim, Y Choi, S Suresh, and A Argon. Nanocrystallization during nanoindentation of a bulk amorphous metal alloy at room temperature. *Science*, 295(5555):654--657, 2002.

[113] M Chen, A Inoue, W Zhang, and T Sakurai. Extraordinary plasticity of ductile bulk metallic glasses. *Physical Review Letters*, 96:245502, 2006.

[114] G Wilde and H Rösner. Nanocrystallization in a shear band: An *in situ* investigation. *Applied Physics Letters*, 98:251904, 2011.

[115] K Hajlaoui, A Yavari, B Doisneau, A LeMoulec, W Botta, G Vaughan, A Greer, A Inoue, W Zhang, and A Kvick. Shear delocalization and crack blunting of a metallic glass containing nanoparticles: In situ deformation in TEM analysis. *Scripta Materialia*, 54(11):1829--1834, 2006.

[116] Hiroyasu Funakubo. *Shape Memory Alloys*. Precision Machinery and Robotics. Gordon and Breach Science Publishers, 1987.

[117] R C Garvie, R H J Hannink, and R T Pascoe. Ceramic steel? *Nature*, 258:703--704, 1975.

[118] F D Fischer, Q P Sun, and K Tanaka. Transformation-induced plasticity (TRIP). *Applied Mechanical Review*, 49(6):317--364, 1996.

[119] R H J Hannink, P M Kelly, and B C Muddle. Transformation toughening in zirconia-containing ceramics. *Journal of the American Ceramic Society*, 83(3):461--487, 2000.

[120] G W Greenwood and R H Johnson. The deformation of metals under small stresses during phase transformation. *Proceedings of the Royal Society A*, 283:403--422, 1965.

[121] C Magee and H Paxton. *Transformation Kinetics, Microplasticity and Aging of Martensite in Fe - 31 Ni*. PhD thesis, Carnegie Institute of Technology Pittsburgh, 1966.

[122] J B Leblond and J C Devaux. A theoretical and numerical approach to the plastic behaviour of steels during phase transformation. *Journal of Mechanics and Physics of Solids*, 34:395--410, 1986.

[123] R M McMeeking and A G Evans. Mechanics of transformation-toughening in brittle materials. *Journal of the American Ceramic Society*, 65(5):242--246, 1982.

[124] A G Evans and A H Heuer. Review - transformation toughening in ceramics: Martensitic transformations in crack-tip stress fields. *Journal of the American Ceramic Society*, 63(5-6), 1980.

[125] J Eshelby. The determination of the elastic field of an ellipsoidal inclusion, and related problems. *Proceedings of the Royal Society of London A*, 241(1226):376--396, 1957.

[126] J Eshelby. The elastic field outside an ellipsoidal inclusion. *Proceedings of the Royal Society of London A*, 252(1271):561--569, 1959.

[127] H Bueckner. A novel principle for the computation of stress intensity factors. *Z. Angrew. Math. Mech*, 50:529--533, 1970.

[128] P Paris, R M McMeeking, and H Tada. The weight function method for determining stress intensity factors. In *Cracks and Fractures*, Cracks and Fractures, ASTM STP 601, Philadelphia, 1976.

[129] S Antolovich and D Fahr. An experimental investication of the fracture characteristics of TRIP alloys. *Engineering Fracture Mechanics*, 4:133--144, 1972.

[130] W Gerberich, P Hemmings, and V Zackay. Fracture and fractography of metastable austenites. *Metallurgical and Materials Transactions B*, 2:2243--2253, 1971.

[131] B Budiansky, J Jutchinson, and J Lambropoulos. Continuum theory of dilatant transformation toughening in ceramics. *International Journal of Solids and Structures*, 19:337--355, 1983.

[132] L Rose. The mechanics of transformation toughening. *Proceedings of the Royal Society of London A*, 412:169--197, 1987.

[133] P Clapp, C Becquart, Y Shao, Y Zhao, and J Rifkin. Transformation toughening explored via molecular dynamics and monte carlo simulations. *Modelling and simulation in materials science and engineering*, 2:551--558, 1994.

[134] H K D H Bhadesia. TRIP-assisted steels? *ISIJ International*, 42(9):1059--1060, 2002.

[135] S Pauly, G Liu, S Gorantla, G Wang, U Kuhn, D H Kim, and J Eckert. Criteria for tensile plasticity in Cu-Zr-Al bulk metallic glasses. *Acta Materialia*, 58:4883--4890, 2010.

[136] S Pauly, G Liu, G Wang, U Kuhn, N Mattern, and J Eckert. Microstructual heterogeneities governing the deformation of $Cu_{47.5}Zr_{47.5}Al_5$ bulk metallic glass composites. *Acta Materialia*, 57:5445--5453, 2009.

[137] S Pauly, J Das, J Bednarcik, N Mattern, K B Kim, D H Kim, and J Eckert. Deformation-induced martensitic transformation in Cu-Zr-(Al,Ti) bulk metallic glass composites. *Scripta Materialia*, 60:431--434, 2009.

[138] Y Wu, Y Xiao, G Chen, C Liu, and Z Lu. Bulk metallic glass composites with transformation-mediated work-hardening and ductility. *Advanced Materials*, 22(25):2770--2773, 2010.

[139] S Pauly, S Gorantla, G Wang, U Kuhn, and J Eckert. Transformation-mediated ductility in CuZr-based bulk metallic glasses. *Nature Materials*, 2010.

[140] S Pauly, G Liu, G Wang, J Das, K B Kim, U Kuhn, D H Kim, and J Eckert. Modeling deformation behaviour of Cu-Zr-Al bulk metallic glass matrix composites. *Applied Physics Letters*, 95:101906, 2009.

[141] K Song, S Pauly, B Sun, J Tan, M Stoica, U Kuhn, and J Eckert. Correlation between the microstructures and the deformation mechanisms of CuZr-based bulk metallic glass composites. *AIP Advances*, 3:012116, 2013.

[142] X F Wei, Y F Sun, S K Guan, D Terada, and C H Shek. Compressive and tensile properties of CuZrAl alloy plates containing martensitic phases. *Materials Science and Engineering A*, 517:375--380, 2009.

[143] Y Wu, H Wang, H Wu, Z Zhang, Z Hui, G Chen, D Ma, X Wang, and Z Lu. Formation of Cu-Zr-Al bulk metallic glass composites with improved tensile properties. *Acta Materialia*, 59:2928--2936, 2011.

[144] D Schryvers, G S Firstov, J W Seo, J Van Humbeeck, and Y N Koval. Unit cell determination in CuZr martensite by electron microscopy and x-ray diffraction. *Scripta Materialia*, 36(10):1119--1125, 1997.

[145] T Voigtmann. Yield stresses and flow curves in metallic glass formers and granular systems. *European Physical Journal E*, 34(106), 2011.

[146] M Falk, M Toiya, and W Losert. Shear transformation zone analysis of shear reversal during granular flow. *pre-print*. ArXiv e-prints 0802.1752v2.

[147] D Klaumunzer, A Lazarev, R Maas, F Dalla Torre, A Vinogradov, and J Loffler. Probing shear-band initiation in metallic glasses. *Physical Review Letters*, 107:185502, 2011.

[148] A Lund and C Schuh. Strength asymmetry in nanocrystalline metals under multiaxial loading. *acta materialia*, 53(11):3193--3205, 2005.

[149] H Muhlhaus and I Vardoulakis. The thickness of shear bands in granular materials. *Geotechnique*, 37(3):271--283.

[150] Y F Sun, C H Shek, F S Li, and S K Guan. Stress-induced martensitic transformations in CuZrAl bulk metallic glass forming alloys. *Materials Science and Engineering A*, 479:31--36, 2008.

[151] J Knight, H Jaeger, and S Nagel. Vibration-induced size separation in granular media: The convection connection. *Physical Review Letters*, 70(24):3728--3731, 1993.

[152] O Reynolds. On the dilatancy of media composed of rigid particles in contact. *Philosophical Magazine*, 20:469--481, 1885.

[153] M Mooney, R Finno, and M Viggiani. A unique critical state for sand? *Journal of Geotechnical and Geoenvironmental Engineering*, 124(11):1100--1108, 1998.

[154] M Oda and H Kazama. Microstructure of shear bands and its relation to the mechanisms of dilatancy and failure of dense granular soils. *Geotechnique*, 48(4):465--481, 1998.

[155] H Wolf, D König, and T Triantafyllidis. Experimental investigation of shear band patterns in granular material. *Journal of Structural Geology*, 25(8):1229--1240, 2003.

[156] T Unger. Shear band formation in granular media as a variational problem. *Physical Review Letters*, 92(21):214301 1--4, 2004.

[157] P Rowe. The stress-dilatancy relation for static equilibrium of an assembly of particles in contact. *Proceedings of the Royal Society A*, 269(1339):500--527, 1962.

[158] J Sakaie, D Fenistein, T Carroll, M van Hecke, and P Umbanhowar. MR imaging of Reynolds dilatancy in the bulk of smooth granular flows. *Europhyics Letters*, 85:38001 1--5, 2008.

[159] J T Zhang, P Aimedieu, F Hild, S Roux, and T Zhang. Complexity of shear localisation in a Zr-based bulk metallic glass. *2009*, 61:1145--1148, 2009.

[160] J Liu, H Zhang, H Fu, Z Hu, and X Yuan. In situ spherical B2 CuZr phase reinforced ZrCu-NiAlNb bulk metallic glass matrix composite. *Journal of Materials Research*, 25(6):1159--1163, 2010.

[161] J Das, S Pauly, M Bostrom, K Durst, M Goken, and J Eckert. Designing bulk metallic glass and glass matrix composites in martensitic alloys. *Journal of Alloys and Compounds*, 483:97--101, 2009.

[162] K Terghazi. Old earth-pressure theories and new test results. *Engineering News-Record*, 85(14), 1920.

[163] P Guo and R Wan. A rational approach to stress-dilatancy modelling using an explicit micromechanical formulation. In G Exadaktylos and I Vardoulakis, editors, *Bifurcations, Instabilities, Degradation in Geomechanics*. Springer, Berlin, 2007.

[164] L Sanfratello, J Zhang, S Cartee, and E Fukushima. Exponential distribution of force chain length: a useful statistic that characterizes granular assemblies. *Granular Matter*, 13:511--516, 2011.

[165] J Ye, J Lu, C Liu, Q Wang, and Y Yang. Atomistic free-volume zones and inelastic deformation of metallic glasses. *Nature Materials*, 9:619--623, 2010.

[166] D Ma, A D Stoica, and X L Wang. Power-law scaling and fractal nature of medium-range order in metallic glasses. *Nature Materials*, 7 December, 2008.

[167] P Burnley. The importance of stress percolation patterns in rocks and other polycrystalline materials. *Nature Communications*, 4:2117, 2013.

[168] K-D Liss, D Qu, and M Reid. Variability of poisson's ratio and enhanced ductility in amorphous metal. *Advanced Engineering Materials*, 15(5):347--351, 2013.

[169] A Tordesillas, G Hunt, and J Shi. A characteristic length scale in confined elastic buckling of a force chain. *Granular Matter*, 13:215--218, 2011.

[170] F Shimizu, S Ogata, and J Li. Yield point of metallic glass. *Acta Materialia*, 54:4293--4298, 2006.

[171] R D Conner, William L Johnson, N E Paton, and W D Nix. Shear bands and cracking of metallic glass plates in bending. *Journal of Applied Physics*, 94(2), 2003.

[172] S H Zhou and R E Napolitano. Phase stability for the Cu-Zr system: First-principles, experiments and solution-based modeling. *Acta Materialia*, 58:2186--2196, 2010.

[173] Y Li, Q Guo, J Kalb, and C Thompson. Matching glass-forming ability with the density of the amorphous phase. *Science*, 322:1816--1819, 2008.

[174] R A Stephenson. The equilibrium field near the tip of a crack for finite plane strain of incompressible elastic materials. *Journal of Elasticity*, 12(1):65--99, 1982.

[175] J Rice. Some remarks on elastic crack-tip stress fields. *International Journal of Solids and Structures*, 8(2):751--753, 1972.

[176] S Deville, H Attaoui, and J Chevalier. Atomic force microscopy of transformation toughening in ceria-stabilized zirconia. *Journal of the European Ceramic Society*, 25:3089--3096, 2005.

[177] J Das, S Pauly, C Duhamel, B C Wei, and J Eckert. Microstructure and mechanical properties of slowly cooled $Cu_{47.5}Zr_{47.5}Al_5$. *Journal of Materials Research*, 22(2):326--332, 2007.

[178] J Thompson and G Hunt. *A general theory of elastic stability*. Wiley, 1973.

[179] V Keryvin, R Crosnier, R Laniel, V Hoang, and J Sangleboef. Indentation and scratching mechanisms of a ZrCuAlNi bulk metallic glass. *Journal of Physics D: Applied Physics*, 41(074029), 2008.

[180] W Wang. Metallic glasses: Family traits. *Nature Materials*, 11:275--276, 2012.

[181] W Wang. Properties inheritance in metallic glasses. *Journal of Applied Physics*, 111(123519):1--8, 2012.

[182] G Greaves, A Greer, R Lakes, and T Rouxel. Poisson's ratio and modern materials. *Nature Materials*, 10:823--837, 2011.

Appendix A

Mathematica code for Transformation Toughening

Here the code used to perform transformation toughening calculations will be presented. Example inputs will be chosen, along with simple advice for how to edit the code to cover other situations - rather than presenting repeats of very similar code. The code output is not included; some of the calculation outputs for intermediate steps are extremely lengthy and not significantly informative so have been excluded.

A.1 Definition of Parameters

The parameter adv defines the degree of shear band advance relative to the zone height, and is left at the top so it can easily be found for modification.

$$adv = 1 \tag{A.1}$$

The lattice parameters of the austenite and martensite are entered.

$$a0 = 0.3262$$
$$a1 = 0.3278$$
$$c0 = 0.5245 \tag{A.2}$$
$$\beta 1 = 103.88 * \tfrac{\pi}{180}$$

A precalculation is then performed to get the chemical energy of transformation.

$$T = 298 \tag{A.3}$$

$$\Delta G = \frac{-1408.52 + 2.702 * T}{2.135 * 10^{-5}} \tag{A.4}$$

$$Ep = 82000000000 \tag{A.5}$$

$$\beta = 89/82 \tag{A.6}$$

Some basic transformation strains for use later:

$$et3 = 0.00137 \tag{A.7}$$

$$et5 = 0.000137 \tag{A.8}$$

$$eS3 = \frac{a1}{c1} * \cos \beta 1 - \pi/2 \tag{A.9}$$

A.2 Main Calculation

The transformation radius is defined:

$$r3 = K2 * (\cos{(x/2)} * (1 - \sin{(x/2)}\sin{(3*x/2)}) * eS3 - (4.8/3) * eT3 * \sin{(x/2)}) /$$

$$(\Delta G + \beta * Ep * (\frac{eT3^2}{3.6 * (1 + \beta)} + \frac{6 * eS3^2}{7.2 * 1 + \beta}))^2 \quad \text{(A.10)}$$

$$r3' = D[r3, x] \quad \text{(A.11)}$$

In practice this term with the transformation strains for the CuZr system is entirely dominated by the shape strain term, so the below can also be used:

$$r3a = K2 * (\cos{(x/2)} * (1 - \sin{(x/2)}\sin{(3*x/2)}) * eS3) /$$

$$(\Delta G + \beta * Ep * (\frac{eT3^2}{3.6 * (1 + \beta)} + \frac{6 * eS3^2}{7.2 * 1 + \beta}))^2 \quad \text{(A.12)}$$

$$r3a' = D[r3a, x] \quad \text{(A.13)}$$

A zone height is calculated. Note that this uses a value for the angle at which the zone height is maximum that is calculated later (Equation A.47).

$$w5 = r3a * \sin{(x)} \backslash .x \rightarrow 0.517421 \quad \text{(A.14)}$$

The corresponding radius is given by:

$$r4 = r3a \backslash .x \rightarrow 0.517421 \quad \text{(A.15)}$$

A.2.1   Region 1: Shear band sides

Zone normal components:

$$\begin{aligned} nx1 &= 0 \\ ny1 &= -1 \end{aligned} \quad \text{(A.16)}$$

Weight function components:

$$hx1 = (1/(2*sqrt[2*\pi]*(1-\nu)*sqrtr6))*(\sin{(x/2)}*(2-2\nu+\cos{(x/2)}\cos{(3*x/2)})) \quad \text{(A.17)}$$

$$hy1 = (1/(2*sqrt[2*\pi]*(1-\nu)*sqrtr6))*(\cos{(x/2)}*(1-2\nu+\sin{(x/2)}\sin{(3*x/2)})) \quad \text{(A.18)}$$

Elements of the transformation strain matrix:

$$vx1 = \frac{a1}{a0}*\cos{\beta1} - \frac{\pi}{2} - 1 \tag{A.19}$$

$$vy1 = \frac{c1}{\sqrt{2}*a0} - 1 \tag{A.20}$$

$$sx1 = \frac{a1}{c1}*\sin{\beta1} - \frac{\pi}{2}*nx1 \tag{A.21}$$

$$sy1 = -1*\frac{a1}{c1}*\sin{\beta1} - \frac{\pi}{2}*ny1 \tag{A.22}$$

Taking **n**.**h** as a precursor to the integral:

$$nh1 = nx1*(vx1*hx1 + sx1*hy1) + ny1*(sy1*hx1 + vy1*hy1) \tag{A.23}$$

And then the integral to get the contribution to toughening:

$$\Delta K21 = Integrate[(Ep/(1-\nu))*(nh1 + et5*(nx1*hx1 + ny1*hy1)*\left(\frac{\nu}{1-2\nu}\right)),$$

$$\{r6, 0, adv*w\}]\backslash.x \to \pi \quad \text{(A.24)}$$

$$ans1 = \Delta K21\backslash.\nu \to 0.373\backslash.w \to w5 \tag{A.25}$$

Or to get the term considering only the volume component of the transformation:

$$\Delta K21vol = Integrate[et5 * (Ep/(3 * (1 - 2\nu))) * (nh1 * hx1 + ny1 * hy1),$$

$$\{r6, 0, adv * w\}]\backslash .x \to \pi \quad \text{(A.26)}$$

A.2.2 Region 2: Transformation zone edges

Essentially the same method is followed, so the terms should be identifiable from the notation used above.

$$\begin{aligned} nx2 &= 0 \\ ny2 &= 1 \end{aligned} \qquad \text{(A.27)}$$

$$r2 = w \, \sin(x) \qquad \text{(A.28)}$$

$$r2' = D[r2, x] \qquad \text{(A.29)}$$

Surface element for the integral:

$$ds2 = \sqrt{r2^2 + r2'^{\,2}} \qquad \text{(A.30)}$$

$$hx2 = (1/(2*sqrt[2*\pi]*(1-\nu)*sqrtr2))*(\sin(x/2)*(2-2\nu+\cos(x/2)\cos(3*x/2))) \quad \text{(A.31)}$$

$$hy2 = (1/(2*sqrt[2*\pi]*(1-\nu)*sqrtr2))*(\cos(x/2)*(1-2\nu+\sin(x/2)\sin(3*x/2))) \quad \text{(A.32)}$$

$$vx2 = \frac{a1}{a0} * \cos\beta1 - \frac{\pi}{2} - 1 \qquad \text{(A.33)}$$

$$vy2 = \frac{c1}{\sqrt{2} * a0} - 1 \qquad \text{(A.34)}$$

153

$$sx2 = \frac{a1}{c1} * \sin\beta1 - \frac{\pi}{2} * nx2 \tag{A.35}$$

$$sy2 = -1 * \frac{a1}{c1} * \sin\beta1 - \frac{\pi}{2} * ny2 \tag{A.36}$$

$$nh2 = nx2 * (vx2 * hx2 + sx2 * hy2) + ny2 * (sy2 * hx2 + vy2 * hy2) \tag{A.37}$$

And hence the solution:

$$\Delta K22 = Integrate[(Ep/(1-\nu)) * (nh2 + et5 * (nx2 * hx2 + ny2 * hy2) * \left(\frac{\nu}{1-2\nu}\right)),$$
$$\{x, 0.517421, \frac{\pi}{2} + ArcTan[adv]\}] \tag{A.38}$$

$$ans2 = \Delta K22\backslash.v \to 0.373\backslash.w \to w5 \tag{A.39}$$

Or for volume strain only:

$$\Delta K22vol = Integrate[et5 * (Ep * ds2/(3 * (1-2\nu))) * (nh2 * hx2 + ny2 * hy2),$$
$$\{x, 0.517421, \frac{\pi}{2} + ArcTan[adv]\}]\backslash.x \to \pi \tag{A.40}$$

A.2.3   Region 3: Ahead of tip

The process for finding the zone normal is slightly more complicated for this case.

$$anx3 = -r3a' * \sin(x) - r3a * \cos(x) \tag{A.41}$$

$$any3 = r3a' * \cos(x) - r3a * \sin(x) \tag{A.42}$$

$$n3 = -anx3, -any3 \tag{A.43}$$

$$n31 = Normalize[n3] \tag{A.44}$$

$$n31x = n31[[1]] \tag{A.45}$$

$$n31y = n31[[2]] \tag{A.46}$$

Finding a point where the x-component of the zone normal is 0 can nicely give the angle at which the zone height forms a maximum (plotting the zone radius helps identify which maximum is the relevant one).

$$Solve[n31x == 0, x] \tag{A.47}$$

$$hx3 = (1/(2 * sqrt[2 * \pi] * (1 - \nu) * sqrtr3a)) * (\sin{(x/2)} * (2 - 2\nu + \cos{(x/2)}\cos{(3 * x/2)})) \tag{A.48}$$

$$hy3 = (1/(2*sqrt[2*\pi]*(1-\nu)*sqrtr3a))*(\cos{(x/2)}*(1-2\nu+\sin{(x/2)}\sin{(3 * x/2)})) \tag{A.49}$$

It should be noted that the below relate to a rotating transformation orientation. Replacing this with a fixed orientation should be fairly simple - consider for example the orientations used for the zone edge and crack side terms.

$$vx3 = (\frac{a1}{c1} * \cos{\beta1} - \frac{\pi}{2} - 1) * n31y + (\frac{c1}{\sqrt{2} * a0} - 1) * n31x \tag{A.50}$$

$$vy3 = \frac{c1}{\sqrt{2} * a0} - 1() * n31y - ((\frac{a1}{c1} * \cos{\beta1} - \frac{\pi}{2} - 1) * n31x \tag{A.51}$$

$$sx3 = -(\frac{a1}{c1} * \sin{\beta1} - \frac{\pi}{2}) * n31x \tag{A.52}$$

155

$$sy3 = -(\frac{a1}{c1} * \sin \beta1 - \frac{\pi}{2}) * n31y \tag{A.53}$$

$$nh3 = nx3 * (vx3 * hx3 + sx3 * hy3) + ny3 * (sy3 * hx3 + vy3 * hy3) \tag{A.54}$$

$$ds3 = sqrtr3a^2 + r3a'^{\,2} \tag{A.55}$$

$$Int4 = \frac{Ep}{1 - \nu} * nh3 * ds3 \backslash .\nu \to 0.373 \tag{A.56}$$

This is then ready to be calculated. Note that the integral has been calculated numerically, since attempting it analytically caused Mathematica to come up with no results.

$$\Delta K23a = NIntegrate[Int4, x, -0.517421, 0.517421] \tag{A.57}$$

If one should be interested in the volume-only terms, the following should be used instead:

$$Int5 = \frac{et5 * Ep}{3 * (1 - 2\nu)} * (n31x * hx3 + n31y * hy3) * ds3 \backslash .\nu \to 0.373 \tag{A.58}$$

Appendix B

Mathematica code for Force Chain Buckling

B.1 Lowest Force Calculations

The aim of this stage of the calculation is to determine the force required to buckle a particular mode. Modes are defined by their wavenumber m. In practical usage this calculation is run multiple times for a given set of inputs, once for each available m. The allowed m with the lowest corresponding force is the buckling mode that operates.

Note that the commentary here is fairly simplistic; the details of the mathematics can be found in Sections 4.2, 4.3, 4.4 or the papers of Tordesillas and Hunt [3] [4]. The code itself and a little explanation is presented here; the output of some of the code is extremely lengthy and would serve little utility so is excluded.

B.1.1 Defining parameters

First, a variable is placed at the top of the document defining m (here $m1$ is used). This is so that it can easily be changed between runs of the code.

$$m1 = 10 \tag{B.1}$$

Next, spring constants are defined, again located right at the top so they can be found and changed easily. Note that kn takes a value calculated in Section 4.4 and the other spring constants

are expressed as fractions of it.

$$
\begin{aligned}
kn &= 64.078 \\
kr &= 0.1 * kn \\
ks &= 0.01 * kn \\
kt &= 0.1 * kn
\end{aligned}
\tag{B.2}
$$

Particle size and number of particles in a chain are then defined:

$$
R1 = 5 * 10^{-10} \tag{B.3}
$$

$$
N2 = 29 \tag{B.4}
$$

B.1.2 Main calculation

The initial potential energy balance equation is now defined. Note that it has already been broken down into Fourier components, and that generic parameters are being used at this stage rather than the versions defined above.

$$
V = \frac{1}{2}k_s R^2 q_i^2 + \frac{1}{2}k_t R^2 (q_{i+1} - q_i - \omega_i - \omega_{i+1})^2 + \frac{1}{2}k_r R^2 (\omega_{i+1} - \omega_i)^2 - \frac{1}{4}FR(q_{i+1} - q_i)^2 \tag{B.5}
$$

$$
q1_i = u_m \sin\left[\frac{im\pi}{N+1}\right] \tag{B.6}
$$

$$
q1_{i+1} = u_m \sin\left[\frac{(i+1)m\pi}{N+1}\right] \tag{B.7}
$$

$$
\omega1_i = \phi_m \cos\left[\frac{im\pi}{N+1}\right] \tag{B.8}
$$

$$
\omega1_{i+1} = \phi_m \cos\left[\frac{(i+1)m\pi}{N+1}\right] \tag{B.9}
$$

The next step is to begin applying equilibrium equations to try to reduce the system to N degrees of freedom:

$$W1 = (D[V, \omega_i]D[\omega 1_i, \phi_m] + D[V, \omega_i]D[\omega_{i+1}, \phi_m]) \tag{B.10}$$

$$W2 = (D[W1, \omega_i]D[\omega 1_i, \phi_m] + D[W1, \omega_i]D[\omega_{i+1}, \phi_m]) \tag{B.11}$$

$$W3 = (D[W1, q_i]D[q1_i, u_m] + D[W1, q_i]D[q_{i+1}, u_m]) \tag{B.12}$$

$$W4 = \sum_{i=0}^{N} W2 \tag{B.13}$$

$$W5 = \sum_{i=0}^{N} W3 \tag{B.14}$$

$$K3 = Simplify[W4/W5] \tag{B.15}$$

$$K4 = K3\backslash.N \to N2\backslash.m \to m1\backslash.kt \to kt1\backslash.kr \to kr1 \tag{B.16}$$

This constant $K4$ can be used to link q_i and ω_i. Note that below a generic K is used; $K4$ will be introduced when the equations are evaluated at the end.

$$q2_i = u_m \sin\left[\frac{im\pi}{N+1}\right] \tag{B.17}$$

$$q2_{i+1} = u_m \sin\left[\frac{(i+1)m\pi}{N+1}\right] \tag{B.18}$$

$$\omega 2_i = \phi_m \cos\left[\frac{im\pi}{N+1}\right]\backslash.\phi_m \to Ku_m \tag{B.19}$$

$$\omega 2_{i+1} = \phi_m \cos\left[\frac{(i+1)m\pi}{N+1}\right]\backslash.\phi_m \to Ku_m \tag{B.20}$$

Substituting into the potential energy equation V gives:

$$W = \frac{1}{2}k_s R^2 q2_i^2 + \frac{1}{2}k_t R^2(q2_{i+1} - q2_i - \omega 2_i - \omega 2_{i+1})^2 + \frac{1}{2}k_r R^2(\omega 2_{i+1} - \omega 2_i)^2 - \frac{1}{4}FR(q2_{i+1} - q2_i)^2$$

(B.21)

Via the equilibrium methods outlined in Tordesillas et al [4] [3], the double-differential of W with respect to u_m should equal 0.

$$A0 = D[W, u_m] \tag{B.22}$$

$$A1 = D[A0, u_m] \tag{B.23}$$

Setting this double-differential of W to 0 and solving for F gives:

$$F1 = Solve[A1 == 0, F] \tag{B.24}$$

This is hence the force required to buckle mode $m1$. It can be evaluated by introducing numeric values for the input parameters.

$$F2 = F1\backslash .kr \to kr1\backslash .kt \to kt1\backslash .ks \to ks1\backslash .R \to R1 \tag{B.25}$$

$$F3 = F2\backslash .K \to -K4 \tag{B.26}$$

$$F4 = F3\backslash .m \to m1\backslash .N \to N2 \tag{B.27}$$

Hence giving the final output of the calculation.

B.2   Volume Strain Calculations

This section aims to calculate the volume strain associated with a given axial strain shortly after buckling.

B.2.1 Defining parameters

Note that the corresponding values of F_{min} and K should be taken from the output of the lowest force calculation above.

$$R = 5 * 10^{-10} \tag{B.28}$$

$$F_{min} = 1.60 * 10^{-9} \tag{B.29}$$

$$N1 = 29 \tag{B.30}$$

$$M = 30 \tag{B.31}$$

$$K = 2 \tag{B.32}$$

$$kn = 64.078 \tag{B.33}$$

B.2.2 Main calculation

Firstly, an expression for the buckling axial displacement Δ_b is determined:

$$\Delta_{crit} = \frac{N1 F_{min}}{kn} \tag{B.34}$$

$$\Delta = \epsilon_1 2RN1 \tag{B.35}$$

$$\Delta_b = \Delta - \Delta_{crit} \tag{B.36}$$

Next, the parameter D (see Section 4.3) is calculated:

$$D1 = \sum_{i=0}^{K-2} \left(\cos \frac{(i+1)\pi}{K-1} - \cos \frac{i\pi}{K-1} \right)^2 \qquad \text{(B.37)}$$

Together these can be used to link axial strain to the lateral displacement x:

$$x = \sqrt{\frac{4R\Delta_b}{D1}} \qquad \text{(B.38)}$$

Finally, strain calculations are carried out.

$$\epsilon_2 = \frac{x}{MR} \qquad \text{(B.39)}$$

$$\epsilon_v = \epsilon_2 - \epsilon_1 \qquad \text{(B.40)}$$

$$\epsilon 1_v = \epsilon_v \backslash. \rightarrow \epsilon_1 - > 0.02 \qquad \text{(B.41)}$$

Note also the strain at which buckling begins, before which lateral strain will be zero:

$$\epsilon_{crit} = \frac{F_{min}}{2Rkn} \qquad \text{(B.42)}$$